

Spectroscopy of small boron-containing  
molecules and line intensity calculations  
for HCl and CaH

Gang Li

PhD

University of York

Chemistry

January 2012

# Abstract

The Fourier-transform infrared emission spectra of BO were recorded. The observed spectrum of BO in the 1200 - 2100  $\text{cm}^{-1}$  region contains three bands: the fundamental bands of  $^{11}\text{BO}$  and  $^{10}\text{BO}$  and a hot band of  $^{11}\text{BO}$  with band origins measured to be 1861.9242(97), 1915.3071(09) and 1838.3773(68)  $\text{cm}^{-1}$ , respectively.

The infrared spectra of the unstable HBS molecule in the  $\nu_1$  and  $\nu_3$  fundamental regions have been recorded at high resolution using a Fourier transform spectrometer. Total 35 bands involving 45 vibrationally excited states located up to 6000  $\text{cm}^{-1}$  above the ground state were assigned for  $\text{H}^{11/10}\text{B}^{32}\text{S}$ .

A dipole moment function (DMF) for hydrogen chloride (HCl) has been obtained using a direct fit approach. Combining wavefunctions derived from the Rydberg-Klein-Rees (RKR) numerical method and a semi-empirical DMF, line intensities were calculated numerically for bands with  $\Delta v=0,1,2,3,4,5,6,7$  up to  $v'=7$ .

Einstein A coefficients and absolute line intensities have been calculated for the  $\text{E}^2\Pi\text{-X}^2\Sigma^+$  transition of CaH. Using wavefunctions derived from the RKR method and electronic transition dipole moment functions obtained from high-level ab initio calculations, rotationless transition dipole moment matrix elements have been calculated for all 10 bands involving  $v'=0,1$  of the  $\text{E}^2\Pi$  state to  $v''=0,1,2,3,4$  of the  $\text{X}^2\Sigma$  state. The rotational line strength factors (Hönl-London factors) are derived for the intermediate coupling case between Hund's case (a) and (b) for the  $\text{E}^2\Pi\text{-X}^2\Sigma^+$  transition.

High-resolution spectra of BaS were recorded using laser excitation spectroscopy. The observed rotationally-resolved spectrum of BaS in the 12100-12765  $\text{cm}^{-1}$  spectral range contains the 2-1, 3-1, 3-2, 4-2, 5-2, 5-3 vibrational bands of the  $\text{A}^1\Pi\text{-X}^1\Sigma^+$  transition and the 4-1, 5-1, 5-2 vibrational bands of the  $\text{a}^3\Pi_1\text{-X}^1\Sigma^+$  transition. Approximately 1000 lines of the  $\text{A}^1\Pi\text{-X}^1\Sigma^+$  transition and 600 lines of the  $\text{a}^3\Pi_1\text{-X}^1\Sigma^+$  transition for the main isotopologue  $^{138}\text{Ba}^{32}\text{S}$  (67.5% natural abundance) were measured. Rotational and vibrational parameters were derived for the  $\text{A}^1\Pi$  and  $\text{a}^3\Pi_1$  states.

# Contents

Contents .....	3
Chapter 1.....	18
Introduction.....	18
1.1 Motivation.....	18
1.1.1 Boron-containing molecules.....	19
1.1.2 Line intensity calculations for HCl and CaH.....	21
1.2 Born-Oppenheimer approximation.....	23
1.3 Energy levels of diatomic molecules .....	24
1.3.1 Rotational energy levels.....	24
1.3.2 Combination differences .....	25
1.3.3 Vibrational energy levels .....	26
1.3.3 Rydberg-Klein-Rees (RKR) potential curve and LEVEL program .....	28
1.4 Energy levels of linear triatomic molecules .....	29
1.4.1 Rotational energy levels.....	29
1.4.2 Vibrational energy levels .....	30
1.5 Electronic spectroscopy of diatomic molecules.....	38
1.5.1 Angular momentum in diatomic molecules.....	38
1.5.2 Selections rules for electronic transitions .....	40
1.5.3 Vibrational coarse structure.....	40
Chapter 2.....	44
Experimental .....	44
2.1 Emission source .....	44
2.1.2 Broida-type oven .....	47

2.2 Fourier-transform spectroscopy .....	50
2.2.2 Apodization .....	53
2.2.3 Zerofilling.....	54
2.2.4 Phase correction .....	55
2.2.5 Advantages of FTS.....	55
2.2.6 Bruker IFS-125HR spectrometer .....	59
2.3 Laser excitation spectroscopy.....	64
Chapter 3.....	66
Fourier-transform Infrared Emission Spectroscopy of BO .....	66
3.1 Introduction.....	66
3.2 Experimental.....	67
3.3 Results and discussion.....	68
3.3 Conclusion .....	72
Chapter 4.....	73
High resolution vibration-rotation emission spectroscopy of HBS .....	73
4.1 Introduction.....	73
4.2 Ab initio prediction of the vibration-rotation energy levels .....	77
4.3 Experimental details .....	78
4.4 Analysis of the spectra.....	86
4.4.1. Observed states with $v_2 = 0$ .....	87
4.4.2 Observed states with $v_2 = 1$ .....	88
4.4.3 Observed states with $v_2 = 2$ .....	89
4.4.4 Observed states with $v_2 = 3$ .....	92
4.5 Conclusion .....	101
Chapter 5.....	102

Direct fit of experimental ro-vibrational intensities to the dipole moment function: application to HCl.....	102
5.1 Introduction.....	102
5.2 Methodology and previous results.....	104
5.3 Details of the calculations and the results.....	107
5.3.1 Line intensity of the fundamental band.....	113
5.3.2 Line intensity of the first overtone band.....	113
5.3.3 Line intensity of the second overtone band.....	115
5.3.4 Line intensity of the 4 - 0, 5 - 0, 6 - 0 and 7 - 0 bands.....	116
5.4 Conclusion.....	121
5.5 Future work.....	122
Chapter 6.....	125
Einstein A coefficients and absolute line intensities for the $E^2\Pi-X^2\Sigma^+$ transition of CaH.....	125
6.1 Introduction.....	125
6.2 Methodology.....	127
6.2.1 Hönl-London Factors.....	128
6.2.2 Calculation of Hönl-London Factors for a $^2\Pi-^2\Sigma^+$ Transition...	134
6.3 Details of the calculations and the results.....	138
6.4 Conclusion and future work.....	144
Chapter 7.....	145
High Resolution Laser Excitation Spectroscopy of Barium Monosulfide....	145
7.1 Introduction.....	145
7.2 Experimental detail.....	147
7.3 Results and discussion.....	150
7.3.1 Rotational assignment.....	150
7.3.2 Vibrational assignment.....	151

7.4 Conclusions:.....	158
Chapter 8.....	160
Future work .....	160
8.1 Boron-containing species.....	160
8.1.1 HBO and FBO .....	160
8.1.2 Pure boron clusters .....	165
8.2 List lists of hydrogen halides .....	166
Appendix A.....	167
Line lists for HBS .....	167
Appendix B.....	181
Analytical expressions for the eigenstates of a $^2\Pi$ state.....	181
List of references.....	184

# List of Tables

Table 1.1: Angular momenta in diatomic molecules and their projections on molecular axis.	39
Table 2.1: Boron-containing molecules synthesized using the tube furnace and DC discharge setup.	46
Table 2.2: Available beam splitters for different spectral ranges.	62
Table 2.3: Available detectors for different spectral ranges and their operating temperatures.	63
Table 3.1: Fitted molecular parameters (in $\text{cm}^{-1}$ ) for BO ( $X^2\Sigma^+$ )	70
Table 3.2: Derived molecular parameters (in $\text{cm}^{-1}$ ) for BO( $X^2\Sigma^+$ )	71
Table 4.1: Experimental conditions	80
Table 4.2: Spectroscopic constants (in $\text{cm}^{-1}$ ) for $\text{H}^{11}\text{B}^{32}\text{S}$ and the difference between the observed and ab initio calculated values (see text for details).	93
Table 4.3: Spectroscopic constants (in $\text{cm}^{-1}$ ) for $\text{H}^{11}\text{B}^{32}\text{S}$ and the difference between the observed and ab initio calculated values (see text for details).	94
Table 4.4: Spectroscopic constants (in $\text{cm}^{-1}$ ) for $\text{H}^{11}\text{B}^{32}\text{S}$ and the difference between the observed and ab initio calculated	95

values (see text for details).

Table 4.5: Spectroscopic constants (in $\text{cm}^{-1}$ ) for $\text{H}^{11}\text{B}^{32}\text{S}$ and the difference between the observed and ab initio calculated values (see text for details).	96
Table 4.6: Spectroscopic constants (in $\text{cm}^{-1}$ ) for $\text{H}^{11}\text{B}^{32}\text{S}$ and the difference between the observed and ab initio calculated values (see text for details).	97
Table 4.7: Spectroscopic constants (in $\text{cm}^{-1}$ ) for $\text{H}^{10}\text{B}^{32}\text{S}$ and the difference between the observed and ab initio calculated values (see text for details).	98
Table 4.8: Spectroscopic constants (in $\text{cm}^{-1}$ ) for $\text{H}^{10}\text{B}^{32}\text{S}$ and the difference between the observed and ab initio calculated values (see text for details).	99
Table 4.9: Spectroscopic constants (in $\text{cm}^{-1}$ ) for $\text{H}^{10}\text{B}^{32}\text{S}$ and the difference between the observed and ab initio calculated values (see text for details).	100
Table 5.1: Dipole moment function coefficients of HCl in units of Debye. The number listed in parentheses is the standard error in the last digits of a given value.	114
Table 5.2: Matrix elements $M_{v_0}(m)$ of electric dipole moment of HCl in units of Debye.	109
Table 6.1: $\theta_{J'\Omega'par',J''\Omega''par''}$	133

Table 6.2: General HLF expressions for a ${}^2\Pi\text{-}{}^2\Sigma^+$ transition in which the ${}^2\Pi$ state is intermediate between Hund's cases (a) and (b). Refer to text for further details.	136
Table 6.3: Hönl-London Factors for ${}^2\Pi\text{-}{}^2\Sigma^+$ transitions.	137
Table 6.4: LEVEL outputs for a ${}^2\Pi\text{-}{}^2\Sigma^+$ transition of CaH using RKR potentials and ab initio transition dipole moment function.	141
Table 7.1: Deslandres table of band origins of the $A^1\Pi - X^1\Sigma^+$ transition of ${}^{138}\text{Ba}{}^{32}\text{S}$ .	153
Table 7.2: Franck-Condon factors for the $A^1\Pi - X^1\Sigma^+$ transition of ${}^{138}\text{Ba}{}^{32}\text{S}$ .	154
Table 7.3: Molecular parameters of BaS from a global least-squares fit.	155
Table 7.4: Derived equilibrium spectroscopic constants for BaS.	156

# List of Figures

- Figure 1.1: The distribution of boron among various gases at 20 temperatures above the point where all boron is condensed. Abundances are shown as mole fractions relative to  $\text{H}_2 + \text{He}$  and as fraction of total boron. At high temperatures HBO and BO are found to be the dominant species. At mid-range temperatures  $\text{HBO}_2$ , becomes dominant. Species such as BS, HBS, FBO and  $\text{BO}_2$  may also exist.
- Figure 1.2: Lower and upper stated combination differences. 25
- Figure 1.3: An example of a Morse potential. 27
- Figure 1.4: Normal vibration modes of HBS. The + and - signs are used to define in-plane and out-plane movements.  $\nu_1, \nu_2, \nu_3$  modes are essentially localized H-B stretch, degenerate H-B-S bend in orthogonal planes, and localized B-S stretch, respectively. 31
- Figure 1.5: The excitation of a degenerate vibrational mode of a 32 linear triatomic molecule with all possible transitions.
- Figure 1.6: Observed energy levels and transitions of  $\text{H}^{11}\text{B}^{32}\text{S}$ . 33
- Figure 1.7: Energy level diagram for the first lines of a parallel 36  $^1\Sigma^+ - ^1\Sigma^+$  transition.
- Figure 1.8: Energy level diagram for the first lines of perpendicular 37  $^1\Pi - ^1\Sigma^+$  and  $^1\Pi - ^1\Sigma^-$  transitions.
- Figure 1.9: Angular momentum in diatomic molecules. 38

Figure1.10:	Vibrational progressions and sequences in a electronic spectrum of a diatomic molecule.	41
Figure1.11:	Illustration of the semi-classical Franck-Condon principle.	42
Figure 2.1:	An illustration of the emission source that combines a DC discharge and a high temperature furnace.	44
Figure 2.2:	Schematic diagram of the Broida-type oven at the University of York.	49
Figure 2.3:	Optical arrangement of a Michelson interferometer. M1 and M2 are a fixed and a moving mirror, respectively. $J$ is the half-half beamsplitter and B is the coating on the back. K is a compensator plate.	50
Figure 2.4:	A wide-band continuous spectrum $E(\nu)$ .	52
Figure 2.5:	An interference record $F(x)$ .	52
Figure 2.6:	Instrumental line shapes corresponding to the 10 different apodizing functions compared with the sinc function (dashed line).	56
Figure 2.7:	FTIR spectra of HBS with different zero filling factors.	57
Figure 2.8:	FTIR spectra of HBO using single sided scan and double sided scan.	58
Figure 2.9:	A schematic diagram of the Bruker IFS-125HR	62

spectrometer taken from the user manual. The labelled components are listed on the table above. It should be noted that the source compartment was removed for emission spectroscopy in our experiment.

- Figure 2.10: Schematic diagram showing the principle components of the laser excitation experiment in the Bernath laboratory; titanium:sapphire laser, beam splitter (BS), Iodine cell for calibration, Broida-type oven, Monochromator, power multiplier tube (PMT) and a computer. 65
- Figure 3.1: Emission lines from the two fundamental bands of  $^{11}\text{B}^{16}\text{O}$  and  $^{10}\text{B}^{16}\text{O}$ , and the  $\nu = 2-1$  hot band of the main isotopologue  $^{11}\text{B}^{16}\text{O}$  recorded by Fourier transform spectroscopy. The unmarked features are due to HBO. 68
- Figure 4.1: Overview of the FTIR spectrum of  $\nu_1$  fundamental of HBS with baseline flattened. HBO spectrum was also present as an impurity. 81
- Figure 4.2: Overview of the FTIR spectrum of  $\nu_3$  fundamental of HBS with baseline flattened. HBO spectrum was also present as an impurity. 82
- Figure 4.3: An expanded portion of the HBS spectrum marking some rotational lines of  $\text{H}^{11}\text{B}\text{S}$ . The nature abundance ratio of the  $^{11}\text{B}$  and the  $^{10}\text{B}$  isotopes is 4:1. 83
- Figure 4.4: Observed energy levels and transitions of  $\text{H}^{11}\text{B}^{32}\text{S}$ . 84
- Figure 4.5: Energy level diagram of observed transitions of  $\text{H}^{10}\text{B}^{32}\text{S}$ . 85

Figure 5.1:	Dipole moment functions of HCl using the $M_i$ coefficients from Table 5.1.	112
Figure 5.2:	Comparison of the empirical line intensities with Pine et al. experimental values of the H <sup>35</sup> Cl fundamental band.	113
Figure 5.3:	Comparison of the line-intensities of the H <sup>35</sup> Cl 2-0 band comparison with present study as a reference.	114
Figure 5.4:	Comparison of the line-intensities of the H <sup>35</sup> Cl 3-0 band with experimental values as a reference.	115
Figure 5.5:	Comparison of the line-intensities of the H <sup>35</sup> Cl 4-0 band with experimental values as a reference.	117
Figure 5.6:	Comparison of the line-intensities of the H <sup>35</sup> Cl 5-0 band with experimental values as a reference.	118
Figure 5.7:	Comparison of the line-intensities of the H <sup>35</sup> Cl 6-0 band with experimental values as a reference.	119
Figure 5.8:	Comparison of the line-intensities of the H <sup>35</sup> Cl 7-0 band with experimental values as a reference.	120
Figure 5.9:	Transition dipole moment comparison with experimental values of 1-0, 2-0, 3-0, 4-0, 5-0, 6-0 and 7-0 bands of H <sup>35</sup> Cl. (a)Private communication with J. Coxon and P. Hajigeorgiou.	123
Figure 6.1:	Overview of experimental (upper curve) and simulated (lower curve) spectra for the 0-0 and 1-1 bands of the E <sup>2</sup> Π-X <sup>2</sup> Σ <sup>+</sup> transition of CaH. In the top panel, the	142

residuals (observed minus calculated spectra) are displayed as a percentage with the largest peak in the experimental spectrum set to 100%.

- Figure 6.2: Experimental (upper) and simulated (lower) spectra of the  $Q_1$  and  $Q_2$  branches of the 0-0 band of the  $E^2\Pi-X^2\Sigma^+$  transition of CaH. In the top panel, the residuals are displayed as a percentage with the largest peak in the experimental spectrum set to 100%. 143
- Figure 7.1: The laser excitation spectrum of the  $v' = 4 - v'' = 2$  band of the  $A^1\Pi - X^1\Sigma^+$  transition of BaS. The  $J$  assignments are labelled on the top of the spectrum. 149
- Figure 7.2: 3-D bar plot of the Franck-Condon factors of the  $A^1\Pi - X^1\Sigma^+$  transition of BaS. The x and y axis,  $v'$  and  $v''$ , represent upper and lower vibrational levels of the  $A^1\Pi$  and the  $X^1\Sigma^+$  state, respectively. All possible transitions within the scanned spectral range are marked with asterisks. The 0 - 0, 1 - 0 and 2 - 0 bands were not found in our spectra due to their small Franck-Condon factors. 157
- Figure 8.1: High resolution Fourier transform emission spectrum of HBO  $\nu_3$  fundamental and  $2\nu_2$  overtone bands. 162
- Figure 8.2: High resolution Fourier transform emission spectrum of HBO  $\nu_1$  fundamental band. 163
- Figure 8.3: An extended portion of the high resolution Fourier transform emission spectrum of FBO  $\nu_1$  fundamental band. 164

# Acknowledgements

The research described in this dissertation was supported financially by an EPSRC studentship and the department Wild Fund from Dr Tony Wild. It is a great pleasure to be able to thank some of the people who have helped me in various ways, and whose support has been invaluable over the past three years.

I would like to first thank my supervisor, Peter Bernath, who has been a faithful source of wisdom, encouragement throughout. I am also grateful to Dr Iouli Gordon and Dr Larry Rothman for their advices on the HCl project and great hospitality during my visit at Harvard-Smithsonian. Thanks Dr Martin Cockett for the useful suggestions on my project during the TAP meetings.

Special thanks go to Dr Jin-Guo Wang who had taught me operations of lasers and optics, and so many other useful lab skills. I would acknowledge Prof. Hui Li for the ab initio calculations on HBO and HBS. Thanks go to Dr Ram Ram for collaboration on the HBS and YH projects.

I am indebted to Dr Jeremy Harrison for stimulating discussions on the CaH project. Thanks Rob Hargreaves for recording spectra of BO and HBO with me.

Thanks are due to those who have had the dubious pleasure of sharing offices with me: Jon Tandy, Nick Allen, Gonzalo Gonzalez Abad, Rob Hargreaves, Alex Brown, James Brook, Keith Tereszchuk and my housemate Vidas Regelskis who all have made life at the York much more interesting.

Finally, I would like to thank my parents, sister, and fiancée for their love and support, without which I would never have got here in the first place.

# Dedication

My parents, sister, and fiancée

## Author's declaration

I hereby declare that this thesis is my own work and effort and that it has not been submitted anywhere for any award. Where other sources of information have been used, they have been acknowledged. The leading author of the following papers has authorized the reproduction of the papers in this thesis.

Li, G., Hargreaves, R. J., Wang, J. G., and Bernath, P. F., Fourier-transform infrared emission spectroscopy of BO, *Journal of Molecular Spectroscopy* **263**, 123 (2010).

Li, G., Gordon, I. E., Bernath, P. F., and Rothman, L. S., Direct fit of experimental ro-vibrational intensities to the dipole moment function: Application to HCl, *JQSRT* **112**, 1543 (2011).

Li, G., Harrison, J.J., Ram, R.S., Western, C.M., and Bernath, P. F., Einstein A coefficients and absolute line intensities for the  $E^2\Pi - X^2\Sigma^+$  transition of CaH, *JQSRT* **113**, 67 (2012).

Li, G., Wang, J. G., and Bernath, P. F., High resolution laser excitation spectroscopy of barium Monosulfide, *Journal of Molecular Spectroscopy* **271**, 10 (2012).

# Chapter 1

## Introduction

### 1.1 Motivation

Transient molecules are generally referred to as ‘the molecules that are difficult to isolate from other chemically inert molecules’<sup>1</sup>. These molecules play an important role in chemical reactions and are often found in energetic environments such as in flames, industrial plasma, combustions, propellant systems, the upper atmosphere, the interstellar medium, and stellar atmospheres<sup>2-7</sup>. The methods of synthesis of these molecules in the lab include: flames, electric discharge, high temperature furnace, supersonic jet expansion, and laser vaporization<sup>8-10</sup>. The detection methods for transient molecules, such as laser spectroscopy and Fourier transform spectroscopy, have also been greatly improved during the past few decades<sup>11, 12</sup>.

High resolution spectroscopy is recognized as the best tool to study transient molecules. The high resolution ro-vibrational spectra allow us to identify species unambiguously as well as to obtain their molecular parameters including their geometries. The high resolution spectral lines themselves are also useful in many other aspects, such as monitoring chemical reaction intermediates, their variation with time and their distribution among quantum states<sup>13</sup>.

### 1.1.1 Boron-containing molecules

In recent years, there has been an increasing interest in boron and its compounds. Boron, which has extremely high combustion energy per unit mass, has attracted interest as a fuel for air-breathing rockets<sup>4</sup>. Therefore, a complete knowledge of the species such as HBO involved in boron combustion is needed for boron-based propellants. Boron has also been recognised as a promising element for hydrogen storage in the form of hydrides and special nano-structures<sup>14</sup>. The proton–boron-11 fusion reaction has been suggested as a strong candidate for clean fusion as it is non-radioactive and readily available<sup>15</sup>. Boron is one of the lightest elements and is destroyed in nuclear reactions in the cores of stars. Therefore, its abundance in primitive meteorites and cosmochemical behavior in condensation processes is of great interest. In 1997, Lauretta and Lodders modeled boron chemistry in the solar nebula. They suggested that at high temperature, boron-containing gases may exist in many forms such as BO, HBO, HBS, FBO and HBO<sub>2</sub><sup>3</sup>. (Figure 1.1) Small boron-containing molecules are also widely used in the semiconductor industry. For instance, boron halides are used as feed gases in chemical etching and vapour deposition<sup>16</sup>. Boron doping during the diamond chemical vapour deposition (CVD) process involves small gas phase boron-containing molecules, which were recently studied theoretically by the Ashfold group<sup>17</sup>.

We have recently started a series of spectroscopic studies of these small boron-containing species in our lab, with the aim of providing or updating the necessary spectroscopic database. Potential applications include boron combustion, use in the semiconductor industry, and cosmochemical studies. During my PhD, the high resolution Fourier transform infrared (FTIR) spectra of small boron-containing species such as BO, HBO ( $\nu_1$  and  $\nu_3$  bands), HBS ( $\nu_1$  and  $\nu_3$  bands), FBO ( $\nu_1$  band), HBF<sub>2</sub> ( $\nu_1$  band), were recorded using a Bruker IFS-125HR spectrometer.

These transient or semi-stable boron-containing molecules were synthesized at high temperature ( $\sim 1400^\circ\text{C}$ ) using a high temperature tube furnace in conjunction with DC discharge. This thesis focuses on the analysis of the BO and HBS infrared spectra.

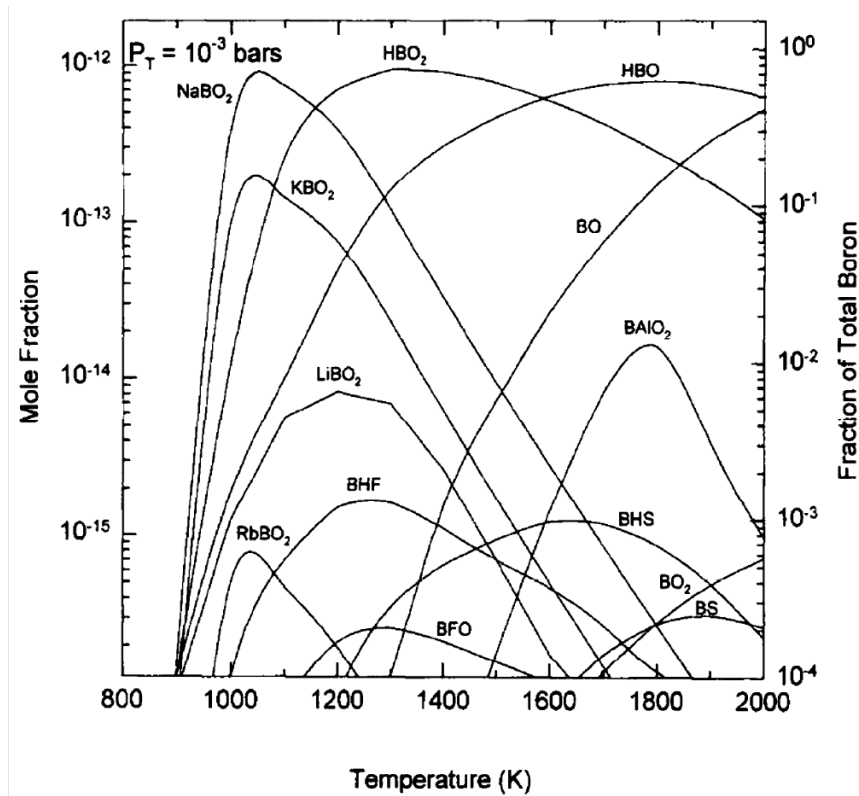


Figure 1.1: The distribution of gas phase boron-containing molecules in a solar nebula. Abundances are shown as mole fractions relative to  $\text{H}_2 + \text{He}$  and as a fraction of total boron. At high temperatures, HBO and BO are found to be the dominant species. At mid-range temperatures,  $\text{HBO}_2$  becomes dominant. Species such as BS, HBS, FBO and  $\text{BO}_2$  may also exist.<sup>3</sup>

### 1.1.2 Line intensity calculations for HCl and CaH

The knowledge of absolute line intensities of molecular species is of fundamental importance with applications in areas such as astrophysics and atmospheric science<sup>7</sup>. This thesis includes the line intensity calculations for HCl and CaH molecules.

A knowledge of accurate spectroscopic line parameters of hydrogen chloride (HCl) is important in modeling and interpreting spectra of stellar<sup>18</sup> and planetary<sup>19</sup> atmospheres. It is also required for the remote sensing of the Earth's atmosphere<sup>20, 21</sup>, laser physics<sup>22, 23</sup>, and precision measurements. Due to their importance, spectral parameters of HCl have been included in the HITRAN spectroscopic database<sup>24</sup> for three decades<sup>25</sup>. We have recently embarked on the task of updating and extending the existing HITRAN data for all hydrogen halides, by improving existing line parameters and including more lines, bands, and isotopologues<sup>26</sup>. During the evaluation of the existing intensity data for HCl, we have found significant discrepancies between the most commonly used semi-empirical dipole moment functions (DMF)<sup>27-32</sup>. Ultimately, a new DMF for HCl was derived, and fitted to the best available (and appropriately weighted) experimental data using a new direct fit approach. The ro-vibrational line intensities derived from our function were compared with the ones based on previously reported DMF's, HITRAN, and experimental data.

CaH is an important molecule in astrophysics, having been identified in the spectra of sunspots<sup>33, 34</sup> and cool brown dwarfs<sup>35, 36</sup> through the observation of bands belonging to the  $A^2\Pi-X^2\Sigma^+$  and  $B^2\Sigma^+-X^2\Sigma^+$  transitions. The CaH bands are particularly strong in M dwarfs and are used to identify M<sup>37</sup> and L<sup>38, 39</sup> type subdwarfs in which metal hydrides are enhanced relative to metal oxides such as TiO. Subdwarfs are metal-poor objects and have very low abundances of heavy elements compared to normal stars like the Sun. The observation of metal hydrides and oxides is, therefore, used as a tool to monitor temperature and composition of the

atmospheres of these objects. Even though the number of new classes of stellar objects has grown<sup>40-42</sup>, an understanding of their atmospheres, evolution, and spectral characteristics remains far from complete. Considerable attempts have been made to develop models to determine their atmospheric parameters, such as chemical composition, pressure, surface gravity, and temperature. Opacities for the molecular species found in the atmospheres of these objects are needed to achieve this goal. However, complete molecular opacity data for many species found in these atmospheres are still lacking, limiting the development of adequate atmospheric models for cool stars and brown dwarfs. For CaH, Weck et al.<sup>43</sup> have performed theoretical calculations on the rovibrationally-resolved transitions involving the  $A^2\Pi$ ,  $B^2\Sigma^+$ ,  $B'^2\Sigma^+$ , and  $E^2\Pi$  excited states and the  $X^2\Sigma^+$  ground states. Their results were in good agreement with the available theoretical and experimental data for the vibrational energy levels and band oscillator strengths.

Recently, we have completed a high-resolution analysis of the  $E^2\Pi$ - $X^2\Sigma^+$  transition of CaH<sup>44</sup> observed in the 20100-20700  $\text{cm}^{-1}$  spectral region. The spectra were recorded using a Bruker IFS-120HR Fourier transform spectrometer, and a rotational analysis of the 0-0 and 1-1 bands was carried out in order to obtain an improved set of spectroscopic parameters for the  $E^2\Pi$  and  $X^2\Sigma^+$  states<sup>44</sup>. These results, combined with the transition dipole moment function of the  $E^2\Pi$ - $X^2\Sigma^+$  transition determined by Weck et al.<sup>43</sup>, have enabled the calculation of Einstein A coefficients and absolute line intensities using the computer programs LEVEL<sup>45</sup> and PGOPHER (version 7.1.108.13)<sup>46</sup>. Line lists and Einstein A coefficients for different bands of the  $E^2\Pi$ - $X^2\Sigma^+$  transition have been generated. A summary of the theoretical approach was applied, and the results of our calculations are presented.

## 1.2 Born-Oppenheimer approximation

In principle, the solution of the Schrödinger equation  $\hat{H}\psi = E\psi$  can explain all of chemistry and spectroscopy. However, so far the exact solution can only be computed for the lightest molecule,  $\text{H}_2^+$ . Thus, one central approximation, the Born-Oppenheimer approximation, named after Max Born and J. Robert Oppenheimer, is introduced by separating the electronic and nuclear motion:

$$E_{total} = E_{electronic} + E_{nuclear}$$

The success of the Born-Oppenheimer approximation is based on one important fact: electrons and nuclei experience similar coulombic forces in magnitude, but electrons are much lighter. As a consequence, electrons move much faster than the nuclei, as if the nuclei are clamped in a fixed geometry. Therefore, the electronic motion can be separated from the nuclear motion. In *ab initio* quantum chemistry calculations, the energies of electronic states are computed on a grid of internuclear distances using software (for example, MOLPRO<sup>47</sup>). This is known as the Born-Oppenheimer potential energy surface.

In fact, there is another version of the Born-Oppenheimer approximation used in scattering theory (Multichannel Quantum Defect Theory). In scattering theory, space is divided into two regions: the Born-Oppenheimer region (near the nuclei) and the Non-Born-Oppenheimer region (far from the nuclei), where electron motion becomes comparable or slower than nuclear motion. The scattering theory is more complete in describing Rydberg states, while the ‘clamped nuclear’ theory is especially useful for studying low-lying electronic states, computationally and experimentally.

## 1.3 Energy levels of diatomic molecules

### 1.3.1 Rotational energy levels

To start with, one may assume that a diatomic molecule is a rigid rotor, thus the Schrödinger equation for the rotational Hamiltonian operator is:<sup>48</sup>

$$\hat{H}\psi = \frac{\hat{J}^2\psi}{2I} = E\psi,$$

where  $\hat{J}$  is the total angular momentum, and  $I$  is the momentum of inertia about an axis perpendicular to the internuclear axis. This Schrödinger equation can be easily solved, giving the energy eigenvalue  $E$ :

$$E = \frac{\hbar^2}{2I}J(J + 1) = BJ(J + 1).$$

In spectroscopy,  $F(J) = E$  is used as the customary expression for the rotational energy levels, and  $B = \frac{\hbar^2}{2I}$  is used as the rotational constant.

In reality, a diatomic molecule is not strictly rigid. A more adequate image of a diatomic molecule is that of two atoms connected by an ‘invisible spring’. During the rotational motion, the internuclear distance  $r$  changes because both atoms are experiencing centrifugal force. The centrifugal force is balanced by the coulombic force. Taking into account the influence of the centrifugal force, the customary expression for rotational energy levels of diatomic molecules can be derived as:

$$F_v(J) = B_vJ(J + 1) - D_v[J(J + 1)]^2$$

in which  $v$  is the vibrational level and the constant  $D_v$  is the centrifugal distortion constant. In fact, there are some other higher-order distortion corrections,  $H_v, L_v, \dots$ . Incorporating these gives:

$$F_v(J) = B_vJ(J + 1) - D_v[J(J + 1)]^2 + H_v[J(J + 1)]^3 + L_v[J(J + 1)]^4 + \dots$$

The rotational constants  $B$  and  $D$  depend on the vibrational levels, specified by the vibrational quantum number,  $v$ , and the electronic state. The customary expression of the vibrational dependence of the rotational constant is a power series:

$$B_v = B_e - \alpha_e \left( v + \frac{1}{2} \right) + \gamma_e \left( v + \frac{1}{2} \right)^2 + \dots,$$

$$D_v = D_e + \beta_e \left( v + \frac{1}{2} \right) + \dots,$$

where  $\alpha_e$ ,  $\gamma_e$  and  $\beta_e$  are called the vibration-rotation interaction constants.

### 1.3.2 Combination differences

The combination differences (Figure 1.2) are defined as the differences of transitions between two vibrational states that share a common upper or lower level. These differences are very useful in the absolute rotational assignment because they depend only on upper or lower state spectroscopic constants. The lower state and upper state rotational combination differences are:

$$\Delta F''(J) = B''(J+1)(J+2) - B''(J-1) = 4B''\left(J + \frac{1}{2}\right)$$

$$\Delta F'(J) = B'(J+1)(J+2) - B'(J-1) = 4B'\left(J + \frac{1}{2}\right)$$

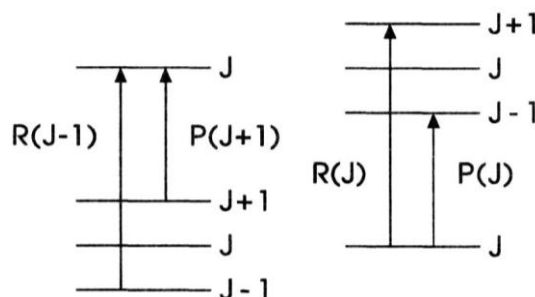


Figure 1.2: Lower (left) and upper (right) state combination differences.

### 1.3.3 Vibrational energy levels

Considering a diatomic molecule as a vibrating rotor, and ignoring the center-of-mass contribution to the kinetic energy, the Schrödinger equation is:

$$\frac{-\hbar^2}{2\mu}\nabla^2\psi + V(r)\psi = E\psi$$

The potential energy  $V(r)$  depends only upon the internuclear distance,  $r$ . In history, there has been considerable effort towards defining the analytical or empirical form of  $V(r)$ . One of the most general forms is the Dunham potential, which is a Power series about  $\xi$ . Here,  $\xi$  is the relative distance to the equilibrium internuclear distance,  $r_e$ .

$$\begin{aligned} V(r) &= a_0 \left(\frac{r-r_e}{r_e}\right)^2 \left[ 1 + a_1 \left(\frac{r-r_e}{r_e}\right) + a_2 \left(\frac{r-r_e}{r_e}\right)^2 + \dots \right] \\ &= a_0 \xi^2 [1 + a_1 \xi + a_2 \xi^2 + \dots] \end{aligned}$$

Although solving the Schrödinger equation with the Dunham potential is impossible, the approximate analytical forms of the solution were given by Dunham. The energy levels from his solution are:

$$E_{v,J} = \sum_{lm} Y_{lm} \left(v + \frac{1}{2}\right)^l \left(v + \frac{1}{2}\right)^m .$$

Another simple form of potential energy function is the Morse potential (Figure 1.3), which is often used in text-books to demonstrate the shape of the potential energy curve ,

$$V(r) = D_e(1 - e^{-\beta(r-r_e)})^2,$$

where  $r_e$  is the equilibrium bond length and  $D_e$  is the well depth (defined relative to the dissociated atoms)

The analytical solution of Schrödinger equation for the Morse potential can be obtained and the vibrational part of the eigenvalue is:

$$G(v) = \omega_e \left( v + \frac{1}{2} \right) - \omega_e x_e \left( v + \frac{1}{2} \right)^2,$$

In fact, the most commonly used vibrational energy level expression is an extension of the above equation:

$$G(v) = \omega_e \left( v + \frac{1}{2} \right) - \omega_e x_e \left( v + \frac{1}{2} \right)^2 + \omega_e y_e \left( v + \frac{1}{2} \right)^3 + \omega_e z_e \left( v + \frac{1}{2} \right)^4 + \dots,$$

where  $v$  is a vibrational quantum number,  $\omega_e$  represents the vibrational wavenumber, while the remaining terms,  $\omega_e x_e$ ,  $\omega_e y_e$ ,  $\omega_e z_e$  are called anharmonicity parameters.

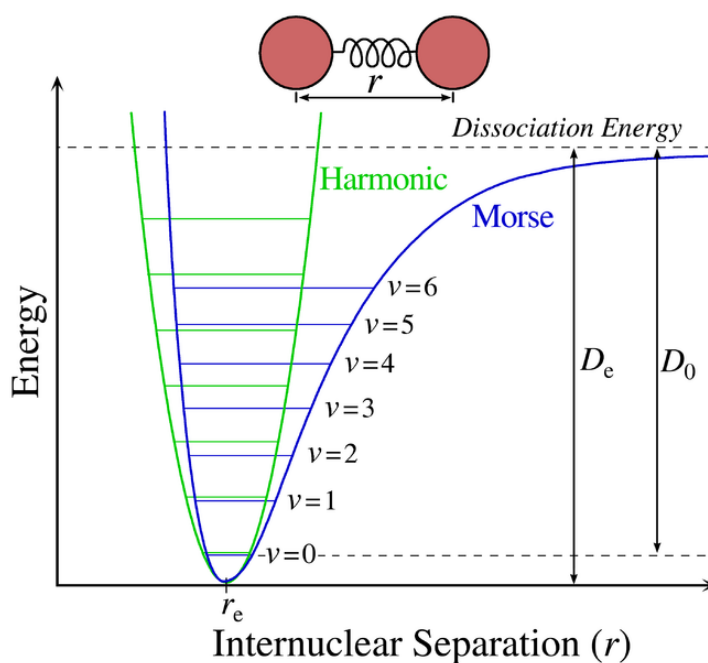


Figure 1.3: An example of a Morse potential. (Mark Somoza, 2006)

Furthermore, the Dunham  $Y_{lm}$  spectroscopic constants can be related back to the conventional expressions by the following relationship:

$$\begin{array}{lll} Y_{10} \approx \omega_e & Y_{20} \approx -\omega_e x_e & Y_{30} \approx \omega_e y_e \\ Y_{01} \approx B_e & Y_{11} \approx -\alpha_e & Y_{21} \approx \gamma_e \\ Y_{02} \approx -D_e & Y_{12} \approx -\beta_e & \dots \end{array}$$

Isotopic species have different reduced masses and, thus, different spectroscopic constants. There are certain relationships between the

isotopic mass and the spectroscopic constants. The isotopic dependence of the Dunham coefficients can be summarized using the following equation:

$$Y_{lm} \propto \left(\mu^{-\frac{l}{2}}\right) (\mu^{-m}) = \mu^{-(l+2m)/2},$$

Moreover, using the above equation, a set of mass-independent constants is defined as:

$$U_{lm} = \mu^{(l+2m)/2} Y_{lm}.$$

This is a great advantage of Dunham parameters, which allows the spectroscopic data of different isotopic species to be combined in a single equation:

$$E_{vJ} = \sum_{lm} \mu^{-\frac{(l+2m)}{2}} U_{lm} \left(v + \frac{1}{2}\right)^l [J(J+1)]^m.$$

### 1.3.3 Rydberg-Klein-Rees (RKR) potential curve and LEVEL program

Even though the Dunham  $Y_{lm}$  parameters can be used to inversely derive the  $a_0, a_1, a_2, \dots$ , coefficients of the Dunham potential function, this method is complicated and not often used. For diatomic molecules, nowadays, some readily available computer programs, such as Le Roy's RKR1 program<sup>49</sup> are able to derived the potential curve from  $G_v$  and  $B_v$  constants using the Rydberg-Klein-Rees method<sup>50</sup>.

Subsequently, this RKR potential curve can be used by Le Roy's LEVEL program<sup>45</sup> to solve the Schrödinger equation numerically. Therefore, the vibration-rotation energy levels,  $E_{v,J}$  and the wavefunctions,  $\psi_{v,J}$  can be obtained. Further applications of the LEVEL program include computing  $B_v, D_v$  constants, and the Franck-Condon factor, which essentially quantifies the overlap of the wavefunctions of two connecting vibrational levels of different electronic states. In

addition, if combined with a dipole moment function of a certain transition, Einstein A coefficients can also be computed. The use of RKR1 and LEVEL programs to calculate the spectroscopic constants and other quantities is discussed in detail in Chapters 5 and 6.

## 1.4 Energy levels of linear triatomic molecules

### 1.4.1 Rotational energy levels

For almost all known triatomic molecules at their ground electronic states, the angular momentum of the electrons about the internuclear axis is zero. As a consequence, as with diatomic molecules, the simple rigid or non-rigid rotor model applies. The expression of energy levels is the same as that for diatomic molecules:

$$F_v(J) = B_v J(J+1) - D_v [J(J+1)]^2 + H_v [J(J+1)]^3 + L_v [J(J+1)]^4 + \dots,$$

The vibrational dependence of rotational constant  $B$  of linear triatomic molecules is different from that of diatomic molecules:

$$B_{(v_1 v_2 v_3)} = B_e - \alpha_1 \left( v_1 + \frac{1}{2} \right) - \alpha_2 (v_2 + 1) - \alpha_3 \left( v_3 + \frac{1}{2} \right),$$

in which  $B_e$  is the rotational constant at equilibrium geometry, and the  $\alpha_i$  ( $i = 1, 2, 3$ ) correspond to three fundamental modes.  $\alpha_1$  and  $\alpha_3$  values are usually positive, which implies that the moments of inertia are slightly larger in the excited levels for the stretching modes, while the bending mode behaves oppositely and the  $\alpha_2$  value is negative for the bending mode. The above equation is very useful in predicting the  $B$  values for the higher vibrational states, thus helping the vibrational assignments.

## 1.4.2 Vibrational energy levels

The triatomic molecules discussed in this thesis, such as HBS and HBO, are all closed-shell molecules. They have no unpaired spins or electronic orbital angular momenta. Thus, the interpretation of the ro-vibrational spectra is entirely based on the nuclear degree of freedom. There are  $3N-5=4$  normal modes for linear triatomic molecules. Each of these four normal modes corresponds to an irreducible representation in the  $C_{\infty v}$  point group list below, with  $\nu_2$  being a doubly degenerate bending mode. These four normal modes are all infrared active (Figure 1.4).

$\nu_1(\sigma^+)$	<i>stretching mode</i>
$\nu_2(\pi)$	<i>bending mode (doubly degenerate)</i>
$\nu_3(\sigma^+)$	<i>stretching mode</i>

The vibrational levels of linear triatomic molecules are usually denoted by  $(\nu_1, \nu_2, \nu_3)$  and the three fundamental vibrational bands are:

upper level	-	ground level
$\nu_1\nu_2\nu_3$		$\nu_1\nu_2\nu_3$
100	-	000
010	-	000
001	-	000

The transition dipole moments associated with the two  $\sigma^+$  fundamental bands, (100)-(000) and (001-000), are known as parallel  $\Sigma - \Sigma$  transitions. The  $\pi$  fundamental band, (010)-(000), is known as a perpendicular  $\Pi - \Sigma$  transition.

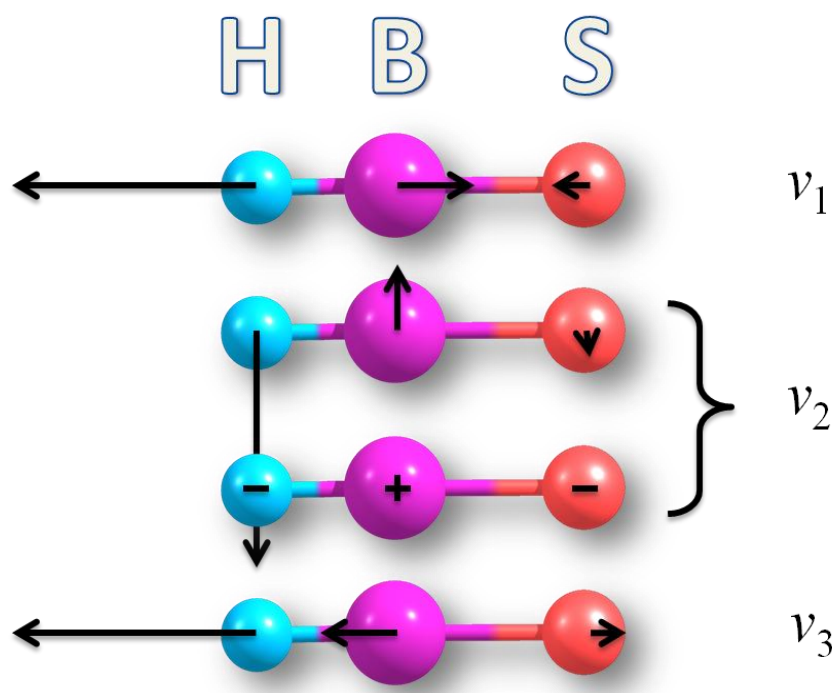


Figure 1.4: Normal vibration modes of HBS. The + and - signs are used to define in-plane and out-plane movements.  $\nu_1$ ,  $\nu_2$ ,  $\nu_3$  modes are essentially localized H-B stretch, degenerate H-B-S bend in orthogonal planes, and localized B-S stretch, respectively.

The excitation of a degenerate vibrational mode leads to an angular momentum  $l$  along the internuclear axis (the imaginary axis that passes through all three nuclei) because the superposition of the two vibrations resembles a rotation. With  $l = 0, 1, 2, \dots$ , the levels are designated  $\Sigma, \Pi, \Delta, \dots$ , respectively, therefore they contain several vibrational sub-levels. The symmetry of these excited vibrational levels is obtained by taking direct products of the symmetry species. In the harmonic oscillator approximation, energy levels with the same  $\nu$  are degenerate. However, when taking anharmonicity into account, these degenerated levels split (see Figure 1.5). The vibrational energy-levels are customarily expressed as:<sup>48</sup>

$$G_{\nu_1\nu_2\nu_3} = \omega_1\left(\nu_1 + \frac{1}{2}\right) + \omega_2(\nu_2 + 1) + \omega_3\left(\nu_3 + \frac{1}{2}\right) \\ + x_{12}\left(\nu_1 + \frac{1}{2}\right)(\nu_2 + 1) + x_{13}\left(\nu_1 + \frac{1}{2}\right)\left(\nu_3 + \frac{1}{2}\right)$$

$$+x_{23} \left( v_3 + \frac{1}{2} \right) (v_2 + 1) + gl^2$$

with  $x_{ab}$  ( $a,b=1,2,3$ ), being the anharmonicity parameters and  $g$  being the separation between two sub-levels with the same  $v$  but different  $l$ .

In addition to fundamental bands, overtone, combination, and hot bands are also allowed in vibrational spectra. All allowed transitions among the first bending energy levels of linear triatomic molecules are depicted in Figure 1.5. Thus, the energy level diagram can be quite complicated. Figure 1.6 gives an example of the energy levels of observed states and transitions of the HBS molecule.

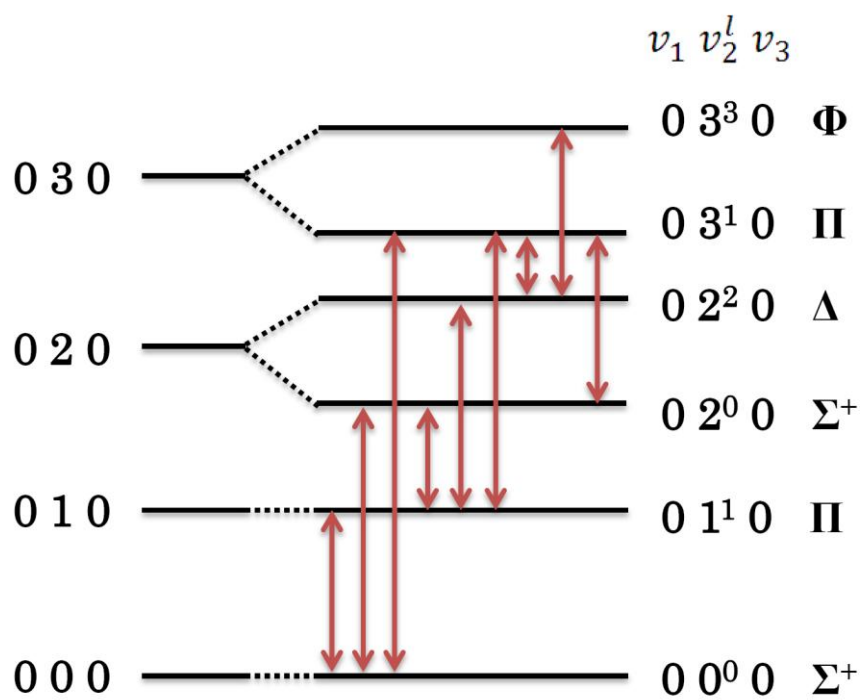


Figure 1.5: The excitation of a degenerate vibrational mode of a linear triatomic molecule with all possible transitions.

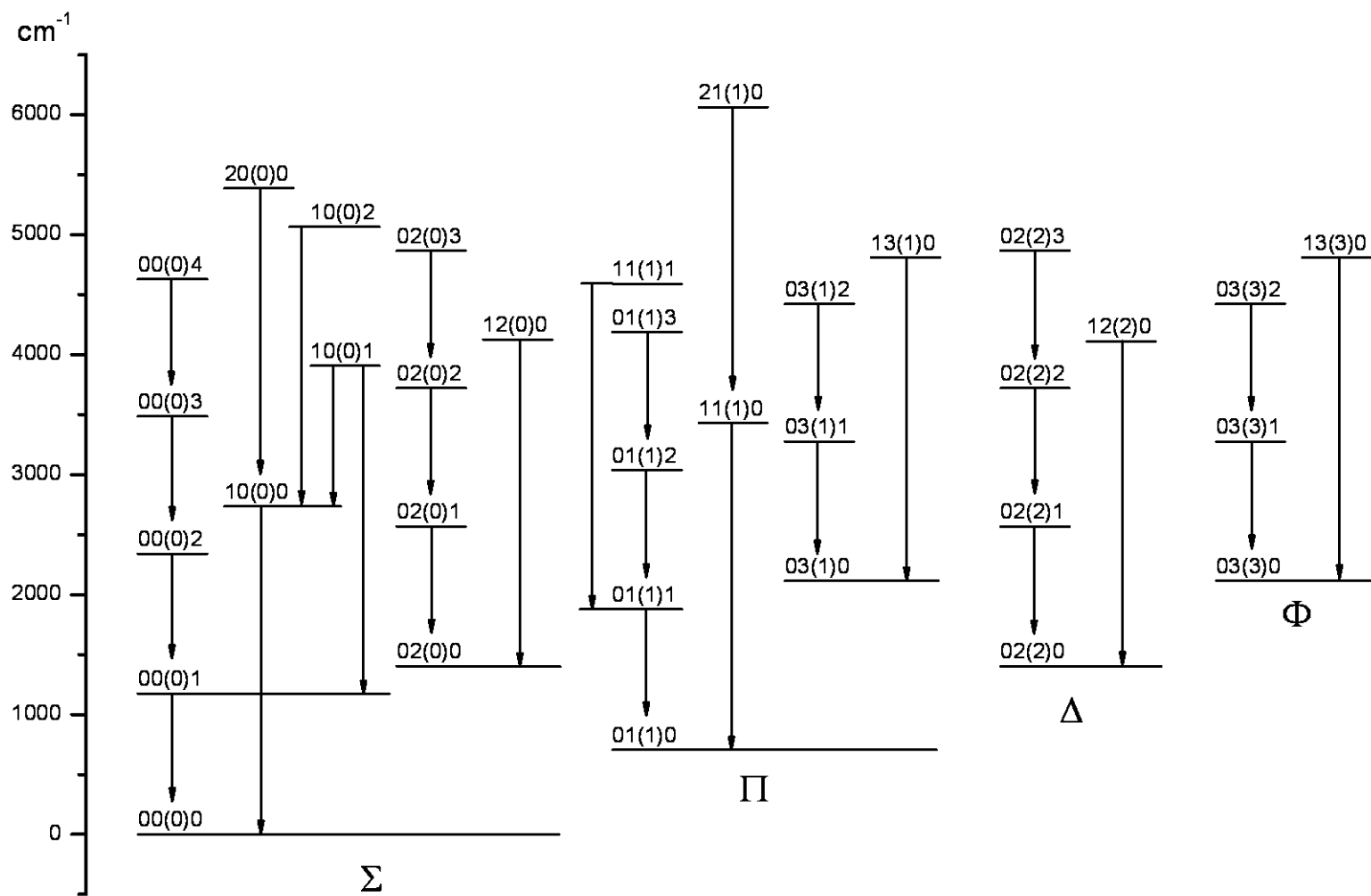


Figure 1.6: Observed energy levels and transitions of  $\text{H}^{11}\text{B}^{32}\text{S}$ .

### 1.4.3 Selection rules

The selection rules for transitions among the excited energy levels come from the transition dipole moment integral. In general, it can be summarized as  $\Delta l = 0, \pm 1, g \leftrightarrow u$ , and  $\Sigma^+ \leftrightarrow \Sigma^-$ . They are cataloged as three types:

1.  $\Delta l = 0, l = 0$ . Parallel  $\Sigma - \Sigma$  type transition with one P branch ( $\Delta J = -1$ ) and one R branch ( $\Delta J = +1$ ). (see Figure 1.7)
2.  $\Delta l = 0, l \neq 0$ .  $\Pi - \Pi, \Delta - \Delta, \Phi - \Phi$ , transitions, and so forth. These transitions have P and R branches ( $\Delta J = \pm 1$ ) and weak Q branches ( $\Delta J = 0$ ), which may not be always observed.
3.  $\Delta l = \pm 1$ . Perpendicular transitions such as  $\Pi - \Sigma, \Delta - \Pi$ . These transitions have P and R branches ( $\Delta J = \pm 1$ ) and a strong Q branch ( $\Delta J = 0$ ). (see Figure 1.8)

Further restrictions on the selection rules for the ro-vibrational transitions arise from the parity of the molecular wavefunctions. The total Hamiltonian operator includes electronic, vibrational, and rotational parts (excluding nuclear spin). In the laboratory coordinates, applying the  $\hat{E}^*$  inversion operator to the particles (nuclei and electrons) inverts all the coordinates – that is,

$$\begin{aligned}\hat{E}^*|X_i, Y_i, Z_i\rangle &= |-X_i, -Y_i, -Z_i\rangle \\ &= \pm |X_i, Y_i, Z_i\rangle\end{aligned}$$

All the relative positions of the particles remain the same after the inversion operation. Thus, the energy levels are unchanged. However, the sign of the wavefunctions may change under the inversion operation. The sign of the eigenvalue of the above equation,  $\pm 1$ , is designated the parity + or -. In general, the selection rule for one-photon electronic dipole transitions is  $+\leftrightarrow -$ . In order to determine its sign under the inversion operation, the total wavefunction is divided into electronic, vibrational, and rotational parts. The effects on these parts need to be determined individually as follows:

$$\psi = \psi_{el}\psi_{vib}\psi_{rot}$$

For the electronic ground state of triatomic molecules, a convenient labeling scheme based on the parity of the rotational wavefunction is used:

$$\hat{E}^*|r\rangle = (-1)^J|r\rangle$$

If the rotational dependence on  $J$  is removed from the total parity, then the remaining parity is labeled by  $e$  or  $f$ . States with  $+(-1)^J$  is designated with  $e$  parity, and those with  $-(-1)^J$  is  $f$  parity. Then the selection rule becomes:  $e \leftrightarrow f$  for Q branch and  $e \leftrightarrow e, f \leftrightarrow f$  for P and R branches, respectively.

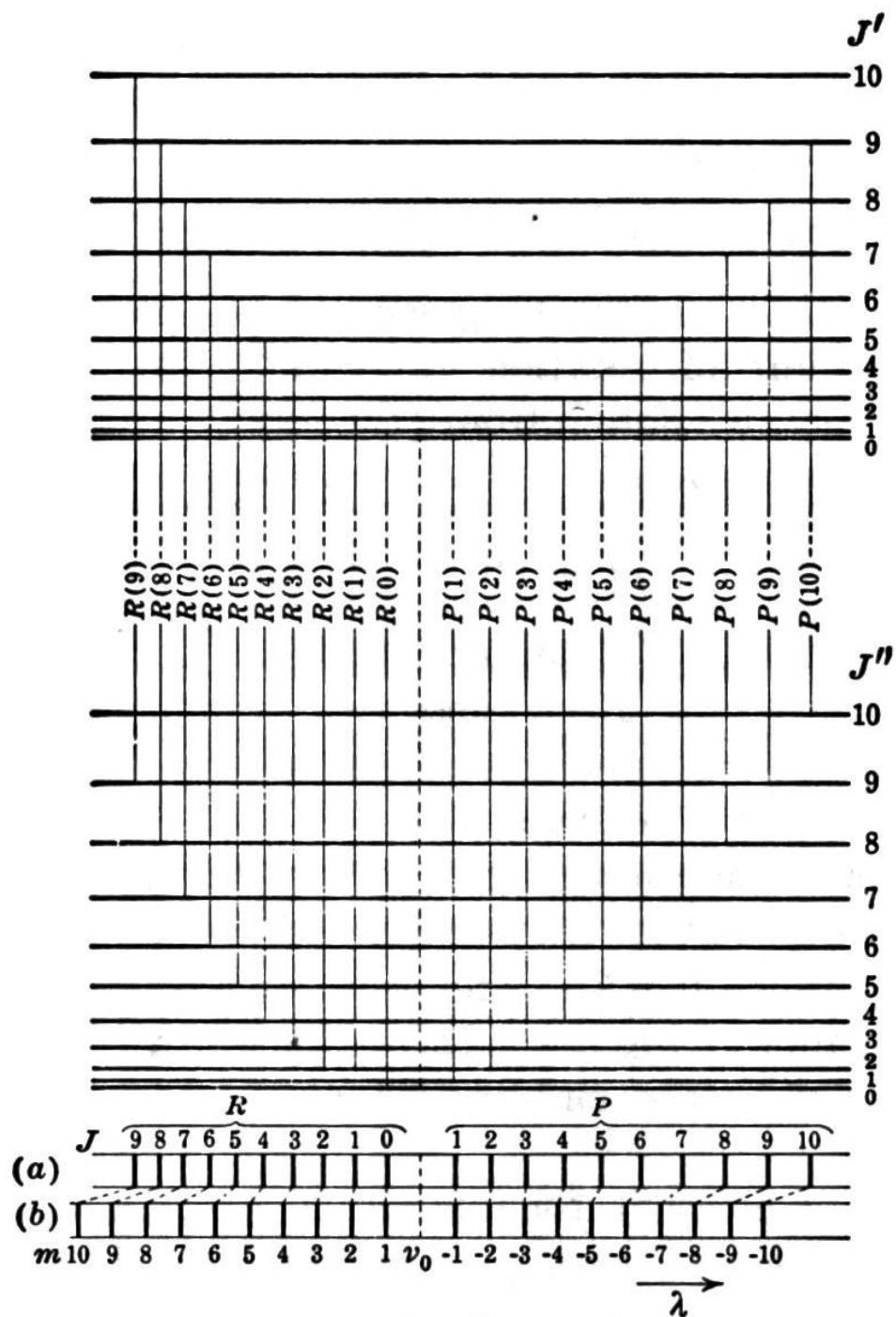


Figure 1.7: Energy level diagram for the first lines of a parallel  $1\Sigma^+ - 1\Sigma^+$  transition<sup>51</sup>.

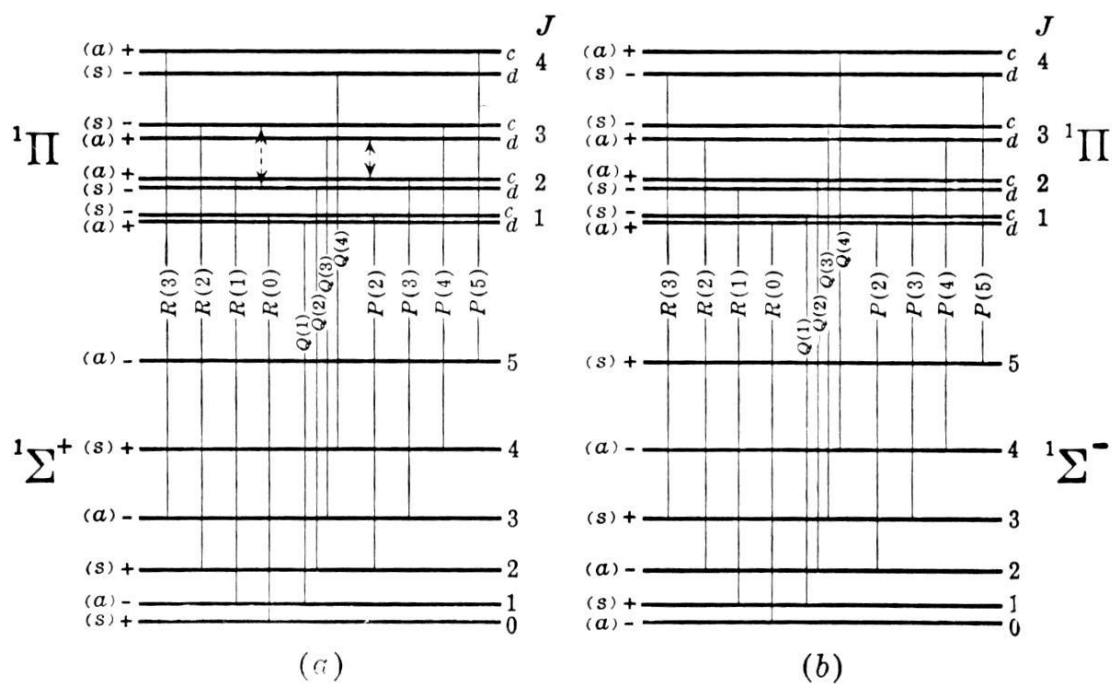


Figure 1.8: Energy level diagram for the first lines of perpendicular  $1\Pi - 1\Sigma^+$  and  $1\Pi - 1\Sigma^-$  transitions<sup>51</sup>.

## 1.5 Electronic spectroscopy of diatomic molecules

In electronic spectroscopy, the various angular momenta and the interactions between them are of great importance. The electronic states of diatomic molecules are characterized by these angular momenta.

### 1.5.1 Angular momentum in diatomic molecules

As shown in Figure 1.9, in diatomic molecules, the total angular momentum,  $\mathbf{J}$ , is the vector sum of three other momenta (excluding vibration and nuclear spin):

$$\mathbf{J} = \mathbf{L} + \mathbf{S} + \mathbf{R}$$

where  $\mathbf{L}$ ,  $\mathbf{S}$ ,  $\mathbf{R}$  are the orbital, spin, and nuclear rotation angular momenta, respectively. Various angular momenta and their projection on the internuclear axis are summarized in Table 1.1.

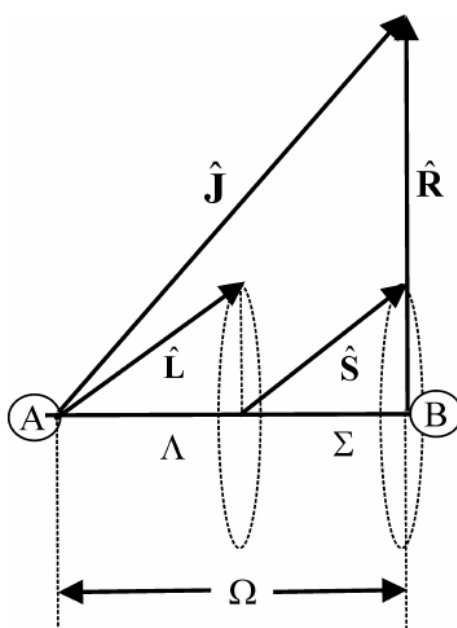


Figure 1.9: Angular momentum in diatomic molecules.<sup>48</sup>

Table 1.1: Angular momenta in diatomic molecules and their projections on the molecular axis.

Angular momentum	Projection on molecular axis (unit of $\hbar$ )
$\mathcal{J}$	$\Omega = (\Lambda + \Sigma)$
$\mathcal{L}$	$\Lambda$
$\mathcal{S}$	$\Sigma$
$\mathcal{R}$	—
$\mathcal{N} = \mathcal{R} + \mathcal{L}$	$\Lambda$

Analogous to the notation of one-electron orbitals in atoms,  $^{2S+1}L_J$ , the electronic states of diatomic molecules are labeled with the symbol  $^{2S+1}\Lambda_\Omega$ . Electronic states with  $\Lambda = 0, 1, 2, 3, \dots$  are designated  $\Sigma, \Pi, \Delta, \Phi, \dots$ . Here the quantum number  $\Lambda$  is the analogue to  $|M_L|$  in an atom. Since in atoms, there are two degenerate states for each  $M_L$  with the same magnitude but different sign, each state in a diatomic molecule with  $\Lambda > 0$  is also doubly degenerate. The quantum number  $\Sigma$  is the component of  $\mathcal{S}$  along the internuclear axis in the unit of  $\hbar$ .  $\Sigma$  is analogue to  $M_S$  in an atom and can have the values:

$$\Sigma = S, S - 1, \dots, -S$$

The multiplicity of the state  $2S + 1$  is indicated by a pre-superscript as in an atom. The quantum number  $\Omega$  is the projection of the total angular momentum, and its value is given by:  $\Omega = |\Lambda + \Sigma|$ . However, the value of  $|\Lambda| + \Sigma$ , instead of  $|\Lambda + \Sigma|$ , is attached to the term symbol as a post-subscript to indicate different components of the same electronic state.

## 1.5.2 Selections rules for electronic transitions

The selection rules for electronic transitions are:

1.  $\Delta\Lambda = 0, \pm 1$ . For example,  $\Sigma - \Sigma, \Pi - \Pi, \Pi - \Sigma, \Delta - \Pi$ , and so forth, are allowed.
2.  $\Delta S = 0$ . Transitions changing multiplicity are highly forbidden for light molecules. But in heavy molecules, as the spin-orbit coupling increases, the  $\Delta S \neq 0$  transitions are possible.
3.  $\Delta\Sigma = 0$  for Hund's case (a).
4.  $\Delta\Omega = 0, \pm 1$ .
5.  $\Sigma^+ - \Sigma^+, \Sigma^- - \Sigma^-$  is allowed, but not  $\Sigma^+ - \Sigma^-$ .
6.  $g \leftrightarrow u$  for homonuclear diatomic molecules.

## 1.5.3 Vibrational coarse structure

Electronic transitions made up of vibrational transitions are called vibronic transitions. Each of the vibronic transitions is made up of rotational lines, thus, they are strictly called rovibronic transitions. Vibronic transitions are organized into sequences and progressions. As shown in Figure 1.10, a progression involves a series of vibronic transitions sharing a common upper or lower level, while a sequence involves a group of bands with the same  $\Delta v$ .

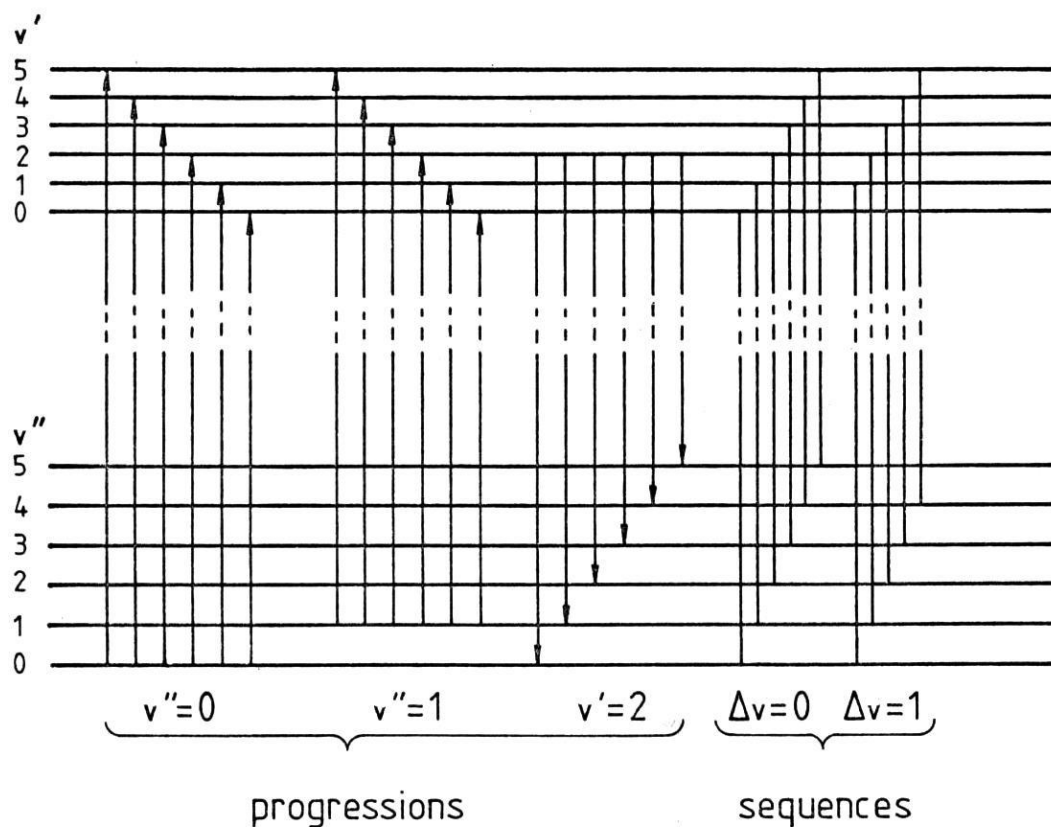


Figure 1.10: Vibrational progressions and sequences in a electronic spectrum of a diatomic molecule.<sup>52</sup>

The band position of a vibronic transition is obtained from the difference of the term values of two vibronic levels, that is:

$$\Delta T_e - \Delta G_v = T' - T'' + \omega'_e \left( v' + \frac{1}{2} \right) - \omega'_e x'_e \left( v' + \frac{1}{2} \right)^2 + \dots$$

$$- \left[ \omega''_e \left( v'' + \frac{1}{2} \right) - \omega''_e x''_e \left( v'' + \frac{1}{2} \right)^2 \right],$$

where  $T$  is the electronic term value, corresponding to the equilibrium configuration, and  $G_v$  is the vibrational term value.

The intensities of a vibronic transition are determined by three factors: the intrinsic strength of the electronic transition, the populations of the initial vibrational level, and the Franck-Condon factor, which is the squared overlap of the two vibrational wavefunctions. The Franck-Condon factor derives from the application of the Franck-Condon principle.

In history, this principle was first invented semi-classically by Franck to explain the various types of intensity distributions found in vibronic transitions. His conclusion was based on the fact that an electronic transition occurs so much more rapidly than a vibronic transition, so that one can assume that the nuclei do not move during the short time of an electronic transition. This is better explained with Figure 1.11. When the equilibrium positions are different for upper and lower states as shown in Figure 1.11a, accounting the Franck-Condon principle, the absorption from point A should go vertically upward to point B instead of to the minimum point C. That is, a transition from A to C is unlikely because there is a large change in  $r$  between A and C. The quantum mechanical version of the Franck-Condon principle is discussed in detail in Chapter 6, but in brief, it is due to the fact that the intensity of a vibronic transition is proportional to the square of the transition moment integral:

$$I_{e'v'e''v''} \propto |\mathcal{R}_e|^2 q_{v'-v''}$$

where  $q_{v'-v''} = |\langle v'|v'' \rangle|^2$  is called the Franck-Condon factor.

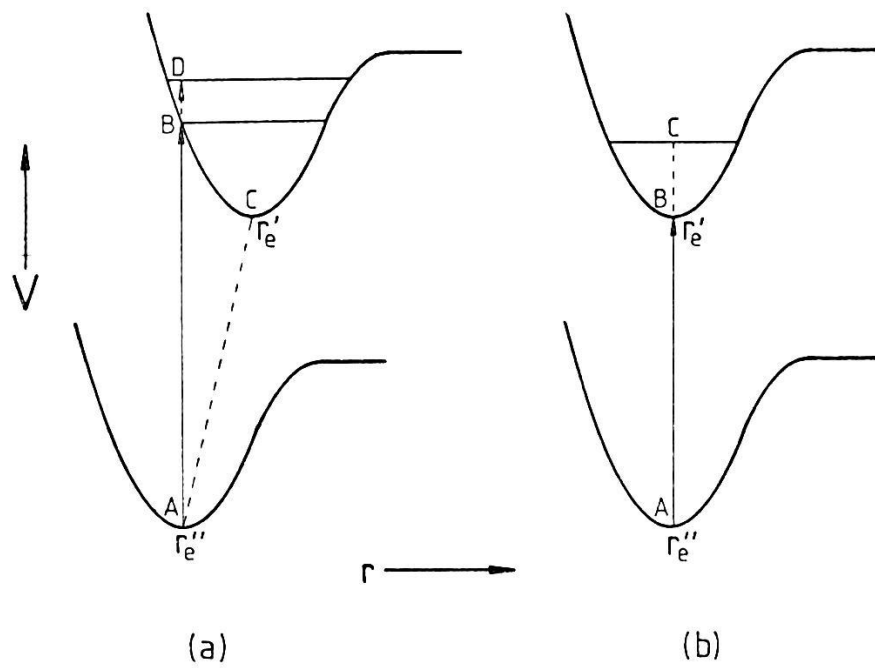


Figure 1.11: Illustration of the semi-classical Franck-Condon principle.<sup>52</sup>

# Chapter 2

## Experimental

Two types of gas phase emission sources were used to synthesize the molecules studied in this thesis: 1) The combination of a high temperature tube furnace and DC electrical discharge; 2) A metal flow reactor known as a Broida-type oven. The preference of one source over another mainly depends on three conditions: the synthesized molecule type, the required experimental temperature and the sensitivity of the detection techniques. In most cases, the tube furnace system is combined with a commercial Fourier transform spectrometer (Bruker IFS-125HR), whereas Broida-type ovens are widely used in laser spectroscopy. Both systems are described in detail in this chapter.

### 2.1 Emission source

#### 2.1.1 Tube furnace with DC discharge

During the investigation of the boron-containing molecules, the high temperature tube furnace combined with a DC electrical discharge is efficient at producing small gas phase boron-containing molecules at high temperature. An illustration of such an experimental setup is shown in Figure 2.1. Table 2.1 provides a list of all the boron-containing molecules generated during my PhD.

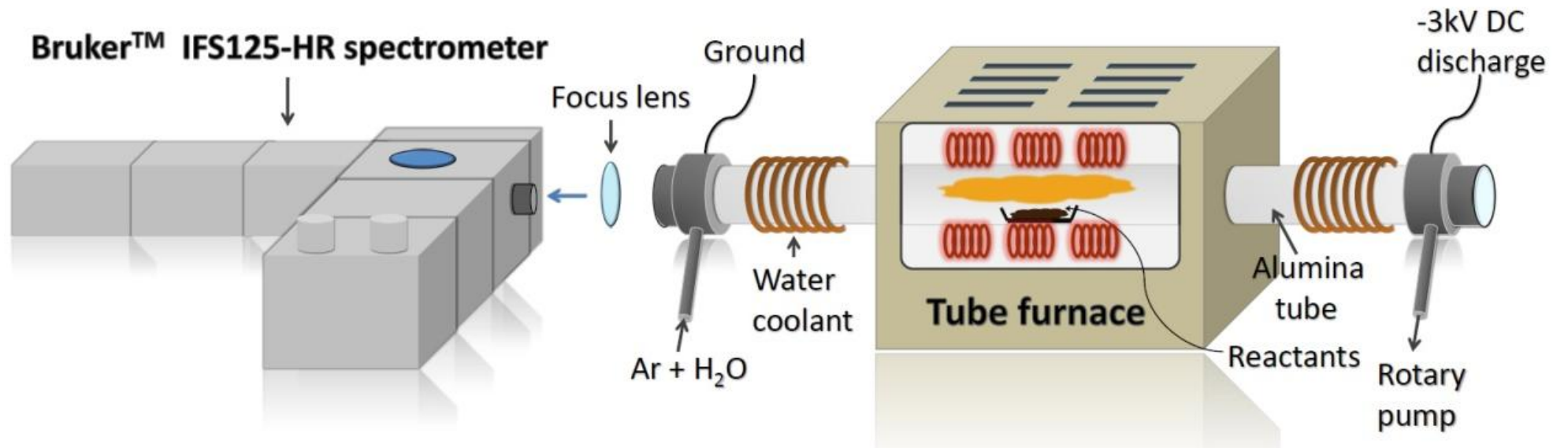


Figure 2.1: An illustration of the emission source that combines a DC discharge and a high temperature furnace.

Table 2.1: Boron-containing molecules synthesized using the tube furnace and DC discharge setup.

Product	Reactants	Condition	Type
BO	Boron, B <sub>2</sub> O <sub>3</sub> , H <sub>2</sub> O	1350 °C + DC Discharge	Emission
HBO	Boron, B <sub>2</sub> O <sub>3</sub> , H <sub>2</sub> O	1350 °C	Emission
HBS	Boron, CS <sub>2</sub> , H <sub>2</sub> O	1300 °C	Emission
FBO	Boron, B <sub>2</sub> O <sub>3</sub> , HCF <sub>3</sub>	1300°C	Emission
HBf <sub>2</sub>	Boron, HCF <sub>3</sub>	800°C	Absorption
BF <sub>3</sub>	Boron, HCF <sub>3</sub>	400°C	Absorption
BF <sub>2</sub> OH	Boron, HCF <sub>3</sub> , H <sub>2</sub> O	800°C	Absorption

The system consists of a Bruker IFS-125HR high resolution Fourier transform spectrometer combined with a commercial CM Rapid Temp furnace (capable of reaching and maintain temperatures up to 1400 °C), and a 1.2-m long alumina (Al<sub>2</sub>O<sub>3</sub>) tube cell. The tube was sealed with two stainless steel end caps which have IR transparent windows. The end of the alumina tube and the end caps were water cooled to prevent damage of the o-ring at each end. The system was maintained at low pressure using an Edwards rotary pump, and monitored using a pressure gauge.

The experiments would typically follow the procedure described below. First, crystalline boron pieces are placed inside an alumina boat. The alumina boat is then inserted into the middle of the 1.2-m long alumina tube. A piece of zirconia felt was placed between the alumina boat and the tube to prevent reaction with the tube wall. The tube is heated gradually by the furnace to a temperature of 1,400°C for around 2.5 hours (the rate of heating up was usually 100 degrees every 10 minutes) to prevent thermal shock of the tube. As the sample is heated, inert argon or helium gas was slowly pumped through the tube to prevent oxidation of the crystalline boron. A flow control valve is used to limit the pumping speed in order to increase the molecular density during the experiment.

Once the sample inside the boat achieves the required temperature, a gas phase reactant is pumped into the tube either directly from a cylinder or by using a bubbler (in the case of liquid). The infrared emission from the products was then focused onto the aperture (component E, Figure 2.2) of the spectrometer using a lens (12 cm focal length).

Occasionally a DC electrical discharge (3 kV, 333 mA) was needed for the production of certain molecules, such as boron monoxide (BO). This is done by attaching a pair of stainless steel cylindrical electrodes to the inside of the end caps. The discharge not only facilitates the production of molecules in the gas phase, but it also populates excited vibrational levels and excited electronic states.

### 2.1.2 Broida-type oven

The Broida oven was first invented by West et al.<sup>54</sup> as a gas-phase molecular source for diatomic metal oxides and halides. It has been widely used since then for many other metal containing molecules<sup>8</sup>. The design of Broida ovens vary in different research groups but the principal components and basic ideas are similar. Figure 2.2 shows a schematic of the Broida-type oven at the University of York.

Essentially, a Broida oven consists of a carbon or alumina crucible (a), which is resistively heated by a tungsten wire basket (b) to vaporize the metal. Inert gas (usually  $\sim 2$  to 5 Torr Argon or Helium) is used as the carrier gas to entrain the metal vapor through a stainless-steel conical chimney (c) into the reaction zone of the oven. An alumina heat shield (d) filled with insulation is placed around the crucible. Zirconia felt is placed between the basket and the insulation to prevent the insulation being burned by the crucible. Water coolant is wired around the whole vacuum chamber and additional water coolant is installed at the bottom of the

baseplate. Prior to the experiment, the current of the resistive tungsten wires is increased gradually every half an hour until the metal begins to glow. This process usually takes about 2-3 hours and the metal vapor can reach a few mTorr. Subsequently, the oxidant is introduced at the top of the chimney through an oxidant ring, and the valve of the vacuum pump is opened up to increase the metal vapor flow. A low-pressure chemiluminescent flame (usually 2- to 3- cm high) containing the product molecule of the metal-oxidant reaction (for example, Ba+CS<sub>2</sub>) is observed on top of the reactant ring.

The Broida oven has its advantages and disadvantages compared with other molecule sources:

- 1) Relatively low temperature ( $\sim 1000$  Kelvin) and pressure (usually less than 5 Torr), thus less congested spectrum for heavy metal containing molecules.
- 2) Large concentration of free radicals ( $\sim 10^{13}$  molecules cm<sup>-3</sup>).
- 3) The spectrum of large molecules can be very congested, thus, difficult to analyze.
- 4) The high resolution spectrum taken with the Broida oven is limited by Doppler broadening and collisional relaxation.

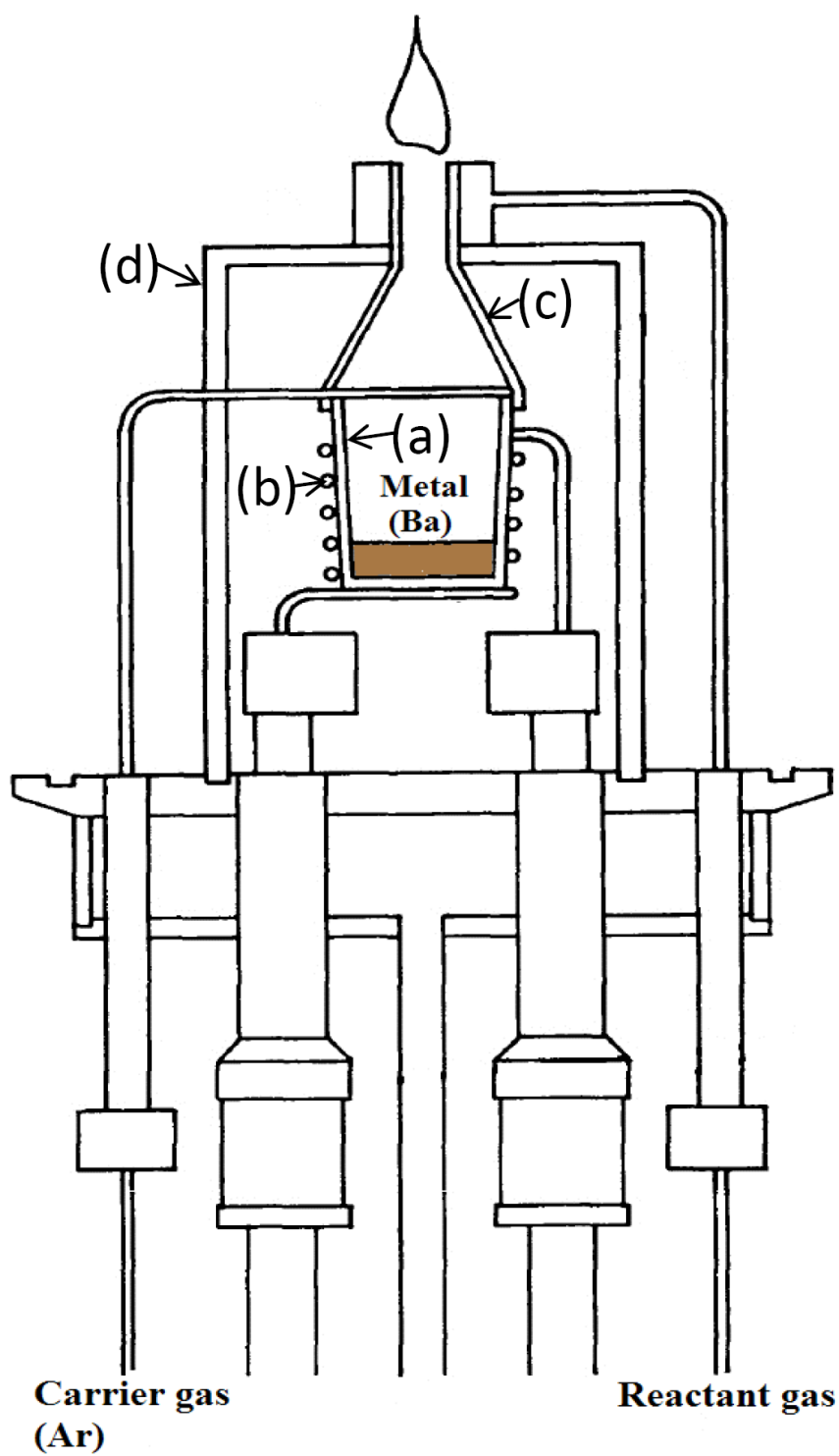


Figure 2.2: Schematic diagram of the Broida-type oven at the University of York.

## 2.2 Fourier-transform spectroscopy

### 2.2.1 Michelson interferometer

In the 1660s, Robert Hooke proposed a wave theory of light and the wave properties of light were supported by the famous Young's double-slit experiment. In the 1880s, A. A. Michelson invented a simple interferometer to study the speed of light. More than half a century later, astrophysicist Peter Fellgett first used an interferometer as a spectrometer to measure the light from celestial bodies. Although the earliest Michelson interferometer only consists of a beamsplitter and two plane mirrors, the principles used in modern Fourier transform spectrometers are essentially the same. Figure 2.3 illustrates the basic optical layout of an Michelson interferometer.

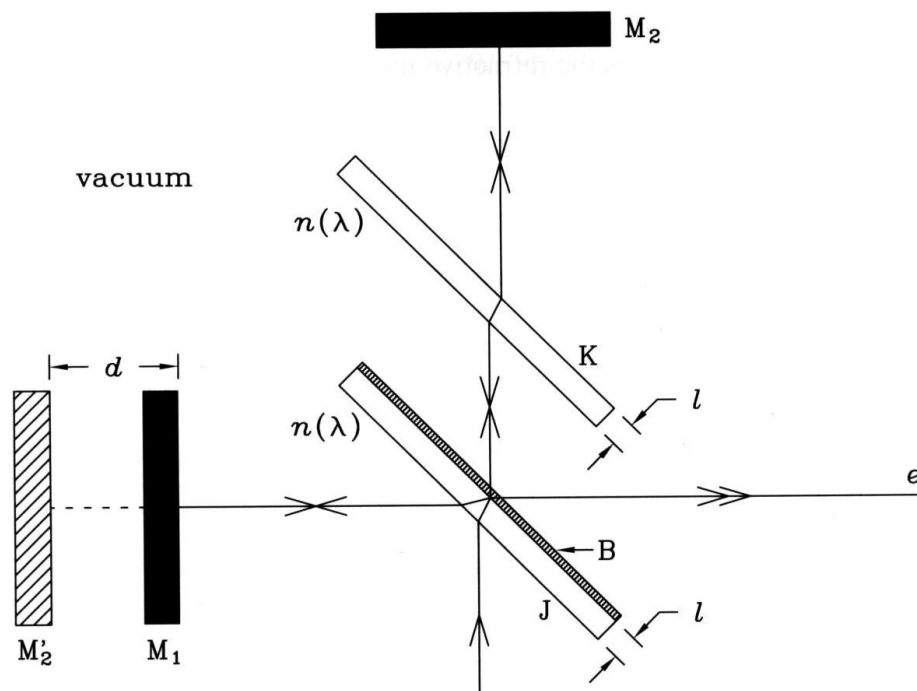


Figure 2.3: Optical arrangement of a Michelson interferometer.  $M_1$  and  $M_2$  are a fixed and a moving mirror, respectively.  $J$  is the half-half beamsplitter and  $B$  is the coating on the back.  $K$  is a compensator plate. This figure is taken from Ref. <sup>11</sup>

The heart of an FT-IR spectrometer is the interferometer. As shown in Figure 2.3, the incident light from the infrared source is separated by a beamsplitter (B) into two parts: which ideally transmits 50% of the light and reflects the remaining part. The reflected part hits a fixed mirror  $M_2$  and is reflected back to the beamsplitter, and the transmitted part of the beam is directed to a movable mirror  $M_1$  and is also reflected back to the beamsplitter. When both beams return to the beamsplitter they are spatially coherent and interfere with each other. Assuming the incident light source is monochromatic and the optical path difference of two beams,  $x = 2d$ , the intensity of the recombined beam is given by:

$$F = 2I_0[1 + \cos(2\pi\nu \cdot 2d)] \quad (2.1)$$

where  $2I_0$  is the intensity of the incident beam,  $\nu$  is the frequency of the incident beam.

Assuming a broadband light source,  $E(\nu)$ , which is continuous and consists of a wide band of wavenumbers (Figure 2.4), the total signal from the whole spectral band is:

$$F(x) = 2 \int_0^{\infty} E(\nu)[1 + \cos(2\pi\nu x)]d\nu \quad (2.2)$$

$F(x)$  is called an interference record or more commonly an interferogram and is shown in Figure 2.5.

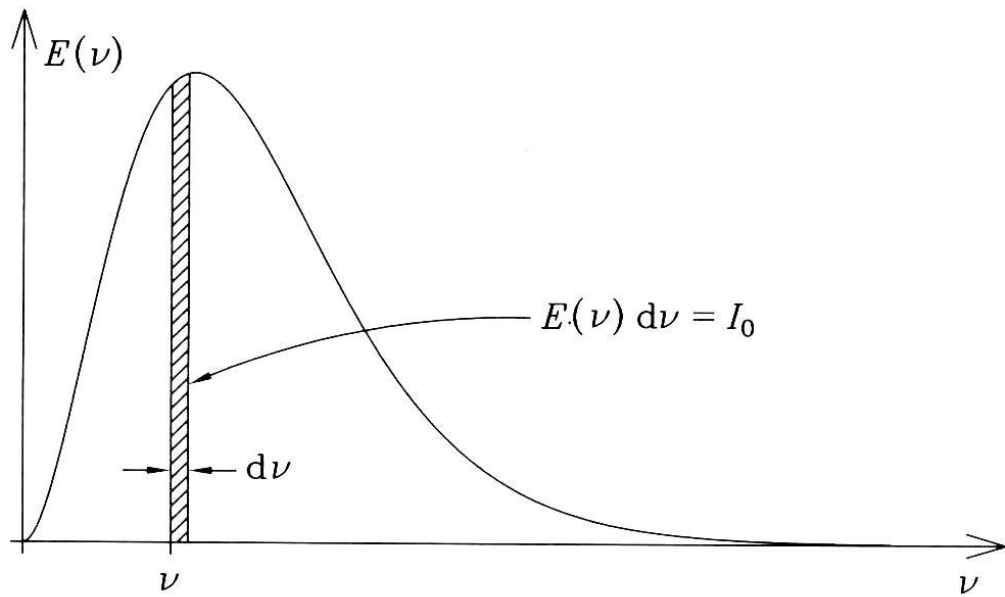


Figure 2.4: A wide-band continuous spectrum  $E(\nu)$ .<sup>11</sup>

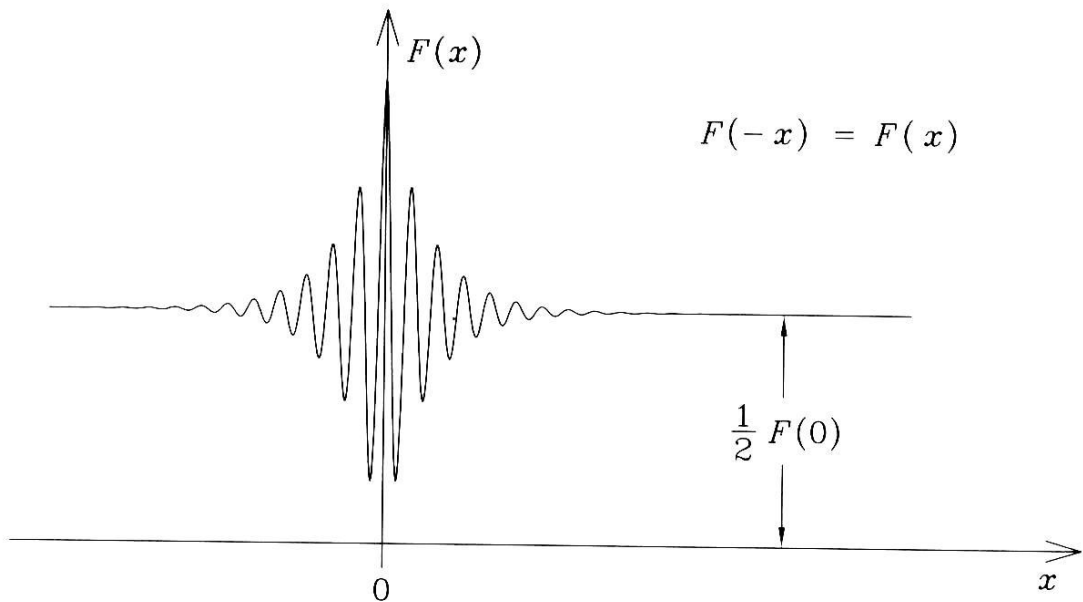


Figure 2.5: An interference record  $F(x)$ .<sup>11</sup>

After subtracting the constant term at zero optical path difference, the interferogram,  $I(x)$ , is obtained:

$$I(x) = F(x) - \frac{1}{2}F(0) = 2 \int_0^{\infty} E(\nu) \cos(2\pi\nu x) d\nu \quad (2.3)$$

To simplify computation, we define  $E(-\nu) = E(\nu)$ , thus

$$I(x) = \int_{-\infty}^{\infty} E(\nu) \cos(2\pi\nu x) d\nu = \int_{-\infty}^{\infty} E(\nu) e^{i2\pi\nu x} d\nu = \mathcal{F}[E(\nu)] \quad (2.4)$$

where  $\mathcal{F}$  is the Fourier transform. Thus, the Fourier transform pair can be written as

$$I(x) = \int_{-\infty}^{\infty} E(\nu) e^{i2\pi\nu x} d\nu = \mathcal{F}[E(\nu)]$$

$$F(\nu) = \int_{-\infty}^{\infty} I(x) e^{-i2\pi\nu x} dx = \mathcal{F}^{-1}[I(x)]$$

In Fourier transform spectroscopy (FTS), the output of a signal is in  $x$ -domain. The desired information is the spectrum in  $\nu$ -domain, which can be calculated from the signal by inverse Fourier transform,  $\mathcal{F}^{-1}$ .

## 2.2.2 Apodization

In a real measurement, the above equation cannot be used because the  $I(x)$  is sampled only for a set of discrete points with a sampling interval  $\Delta x$ . In addition, the data was collected in a finite distance of the mirror travel. The truncated, continuous interferogram  $I_L(x)$  can be thought of as an infinite length interferogram  $I(x)$  multiplied by a boxcar function  $\Pi_{2L}(x)$ .

$$I_L(x) = \Pi_{2L}(x)I(x),$$

$$\Pi_{2L}(x) = \begin{cases} 1, & |x| \leq L, \\ 0, & |x| > L, \end{cases}$$

The sudden truncation of the interferogram leads a  $\text{sinc}\left(\frac{1}{\lambda}\right)$  instrumental line shape (ILS), which oscillates strongly around the base of a narrow line in the spectral domain. This oscillation is also known as ‘ringing’ or ‘leakage’. This effect can be reduced by replacing the boxcar truncation function with a weight function, which equals unity at  $x=0$ , and approaches zero smoothly at large  $|x|$ . This procedure is called ‘apodization’ and the weighted function is called ‘apodization function’. Although apodization can reduce the ringing, it affects the resolution: for example, the HAPP-GENZEL function significantly reduces the ringing, but at the cost of a resolution loss of 50%. Therefore, the choice of a particular apodization function depends on the object of measurement. If the maximum theoretical resolution ( $0.61/L$ ) is needed, then no apodization (boxcar function) is used. In our measurement, a Norton-Beer weak function is usually used, which increases the FWHM of the instrumental line shape (ILS) by 20%. Figure 2.6 gives an example of different apodization functions and their effect on ILS and FWHM.

### 2.2.3 Zerofilling

The ‘fence effect’ of the FTIR spectrum can be solved by adding zeros to the end (zero filling) of the interferogram before the discrete Fourier transform (DFT) is performed. This interpolates the spectrum, thereby reducing the error of line position and intensity measurement. Our original interferograms were always zero-filled with a factor of 2 during experiments, and later on zero-filled by another factor of 8, which gives a total zero filling factor (ZFF) of 16 (see Figure 2.7). Zero filling interpolates using the instrumental line-shape and give better representation compared with other interpolation methods in the spectral domain (such as polynomial or spline).

## 2.2.4 Phase correction

Ideally, the point of zero path difference is the same for all wavelengths. However, due to both optical and electronic effects, the sinusoidal interference pattern for different wavelengths is shifted relatively by a small amount. These phase shifts lead to the asymmetry in the interferogram. This effect can be corrected during DFT using the algorithm developed by Larry Mertz, therefore, it is called 'Mertz phase correction'. Phase shift problems can also be eliminated by using double sided scans when recording the spectra. (see Figure 2.8)

## 2.2.5 Advantages of FTS

Today, most of the spectrometers used in mid-infrared spectroscopy are Fourier transform type. The IR spectrometers that utilize the Fourier transform (FT-IR) provide some significant advantages compared to dispersive spectrometers:

- 1) In dispersive spectrometers, the spectrum is recorded at successive, narrow, wavelength ranges, while FTIR spectrometers record all wavelengths simultaneously.
- 2) The circular aperture used in FTIR spectrometer has a larger area than the slits used in grating spectrometers, enabling more radiation travelling through.
- 3) FTIR gives a precise wavenumber scale, usually a few hundredths of a wavenumber.
- 4) The signal-to-noise ratio of an FT spectrometer can be more than 10 times that of a dispersive spectrometer.

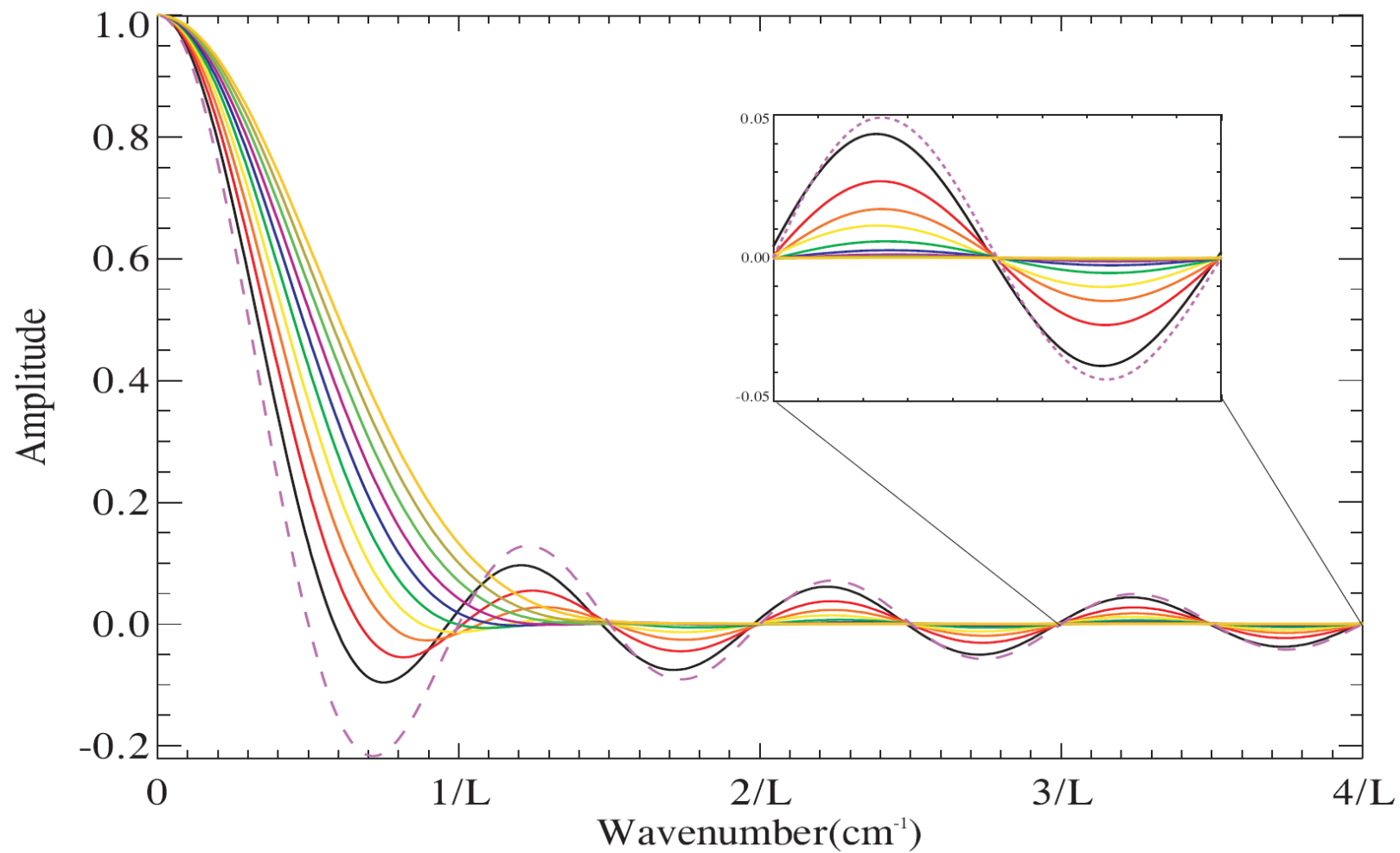


Figure 2.6: Instrumental line shapes corresponding to the 10 different apodizing functions compared with the sinc function (dashed line).<sup>53</sup>

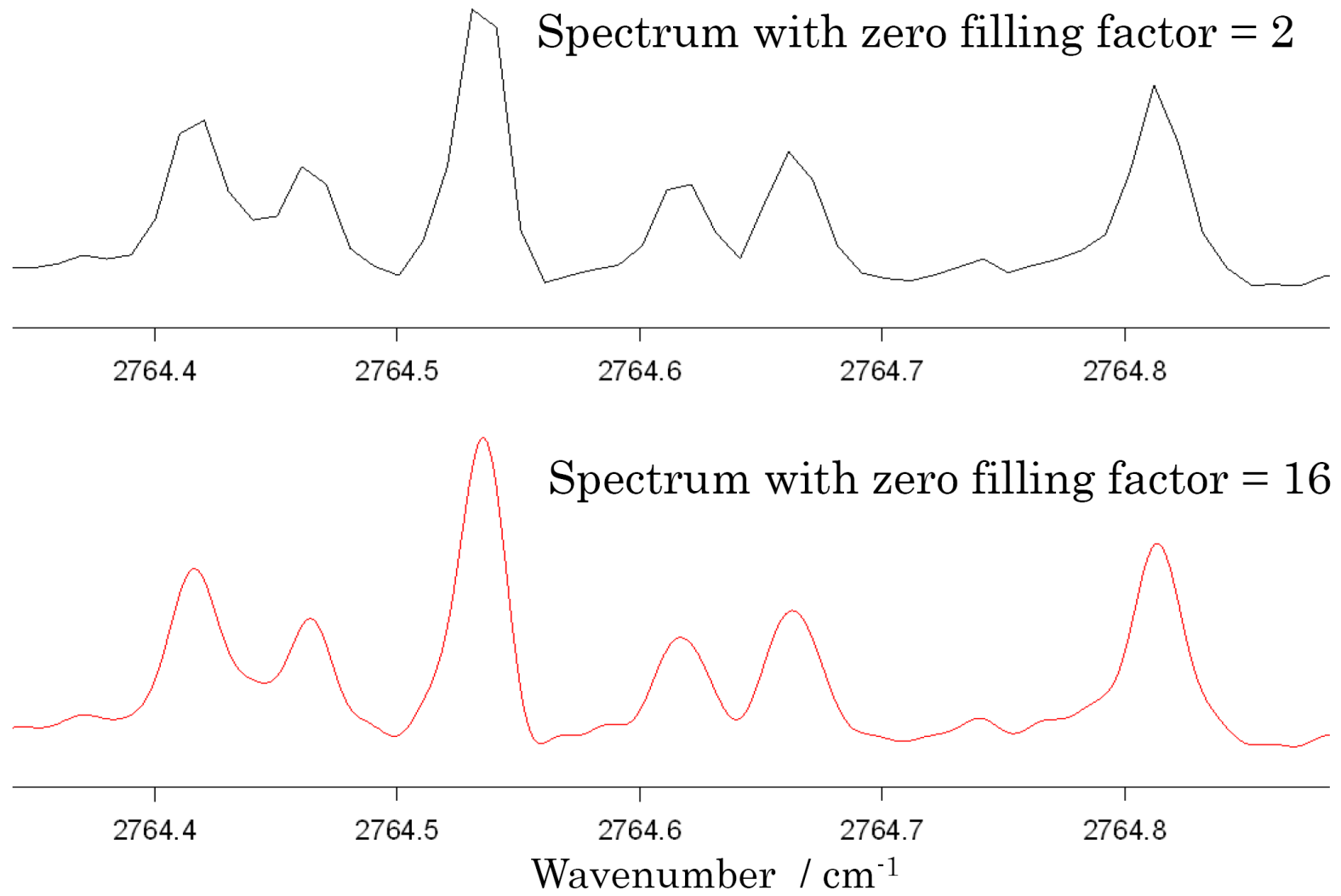
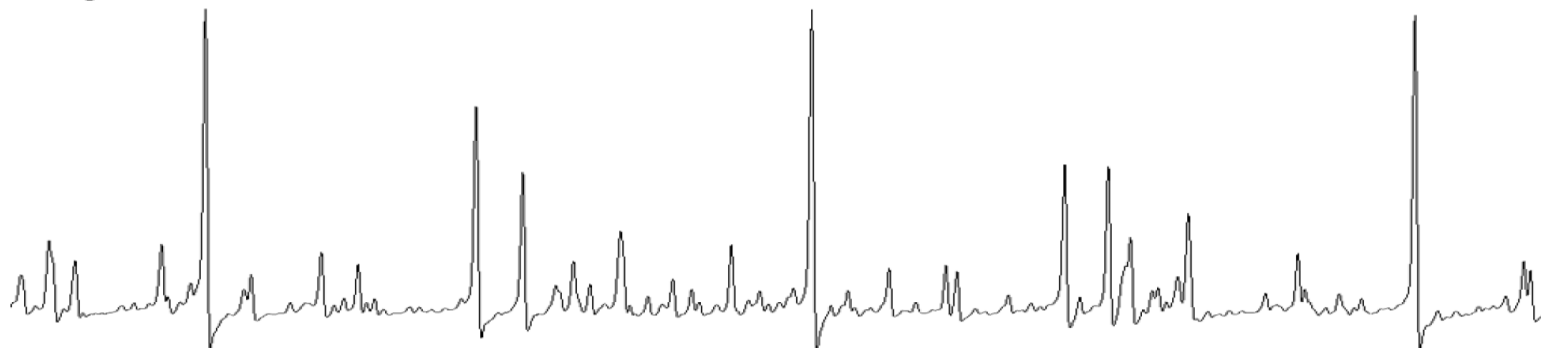


Figure 2.7: FTIR spectra of HBS with different zero filling factors.

Single sided scan



Double sided scan

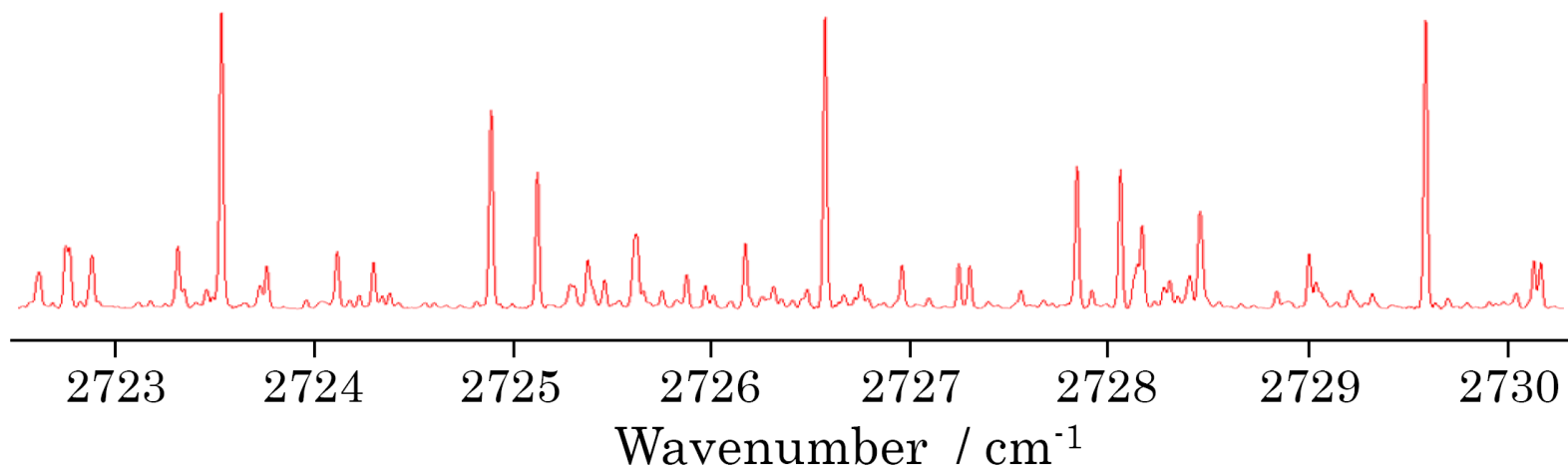


Figure 2.8: FTIR spectra of HBO using single sided scan and double sided scan.

## 2.2.6 Bruker IFS-125HR spectrometer

Figure 2.9 shows the optical arrangements of the Bruker IFS-125HR spectrometer. The emission beam from the furnace (orange colored arrow) was focused by a lens into the spectrometer through a round aperture. The emission beam was then collimated with two folding mirrors (D), and separated by a beamsplitter (B). Ideally, half of it was reflected onto a fixed mirror (C) and travelled back; the other half went through onto a moving mirror and travelled back. Two beams recombined at the beamsplitter. The recombined beam was guided by a series of mirrors (D,J, K and L) to the detector. An Ethernet connection was built up between the spectrometer and a computer to control the vacuum and monitor the status of the spectrometer. Software provided by Bruker called OPUS (version 6.5) was used to control the scanning parameters and the optics settings of the spectrometer (e.g. optical filter, electric filter, and aperture and detector selections).

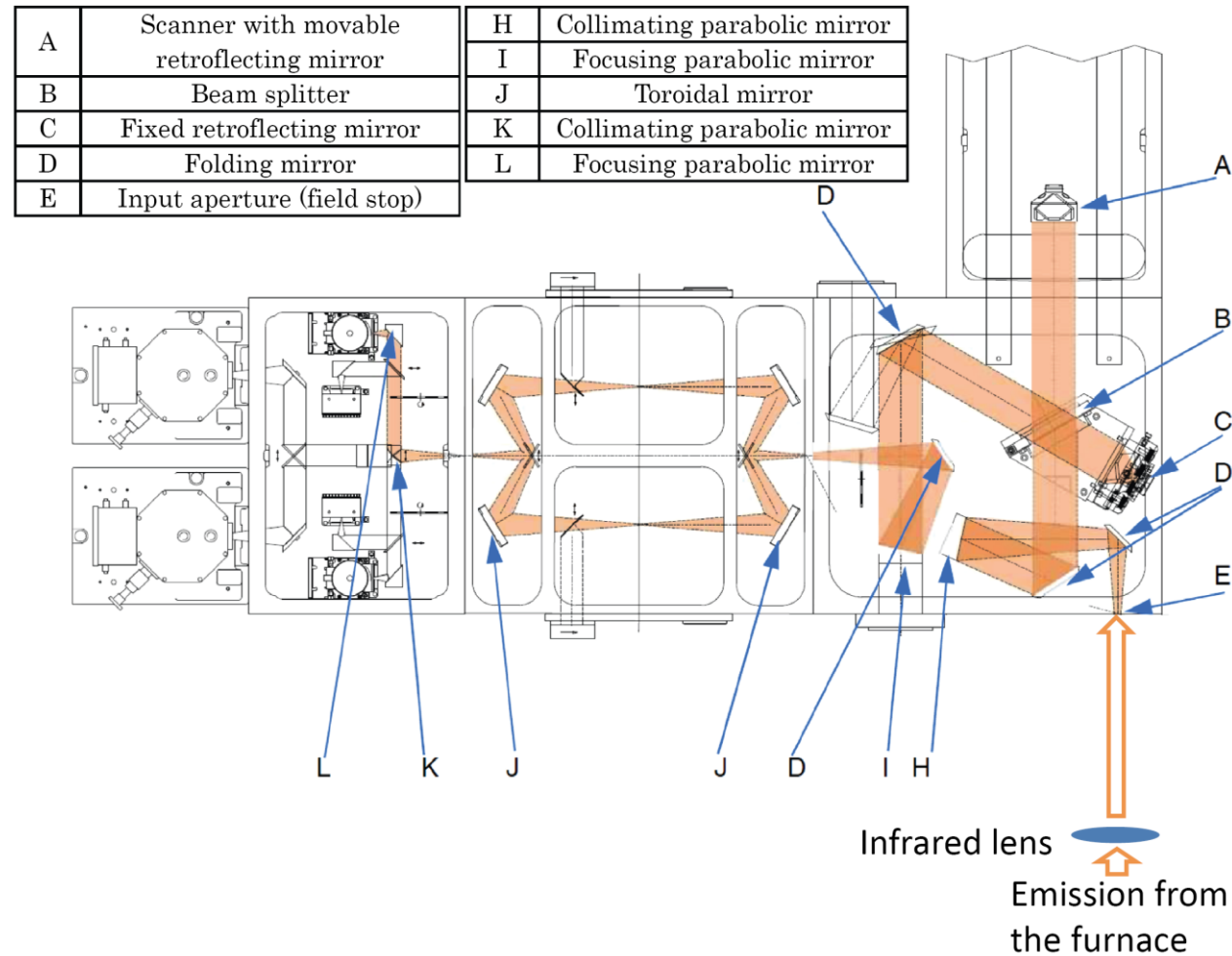


Figure 2.9: A schematic diagram of the Bruker IFS-125HR spectrometer taken from the user manual. The labelled components are listed on the table above. It should be noted that the source compartment was removed for emission spectroscopy in our experiment.

In emission spectroscopy, the combination of an optical filter, beam splitter and detector defines the measurement range. The optical filter is used to cut off any emission outside the desired spectral range. In the mid-infrared (MIR) region (400-5000  $\text{cm}^{-1}$ ), the standard beam splitter is a KBr substrate with multilayered coating. Other types of beam splitters and the spectral coverage are listed in Table 2.2. These beam splitters allow data acquisition in wavelength ranges other than MIR when used in connection with the appropriate detectors (see Table 2.3). The mercury-cadmium-telluride (MCT) detector covers the 450-4800  $\text{cm}^{-1}$  spectral range and a non-linearity correction is necessary. The InSb detector covers the 1850-14000  $\text{cm}^{-1}$  spectral range and it provides a better signal-to-noise ratio (SNR).

The circular aperture controls the amount of incident emissions; the aperture size and the spectral range recorded are limited by the choice of spectral resolution. The spectral resolution is usually determined by the Doppler temperature and pressure broadening at full widths at half maximum (FWHM). The theoretical resolution of a spectrum resolution is  $0.61/L$ . The details of other settings, such as apodization, and zero-filling are discussed in the next section.

Table 2.2: Available beam splitters for different spectral ranges.

<b><i>Beam splitter</i></b>	<b><i>Spectral Range (cm<sup>-1</sup>)</i></b>
<b><i>MIR</i></b>	
KBr	4,800 - 450
<b><i>NIR</i></b>	
CaF <sub>2</sub>	14,000 - 1,850
<b><i>VIS</i></b>	
Quartz(II)	25,000 - 9,500
Quartz(II)	50,000 - 20,000

Table 2.3: Available detectors for different spectral ranges and their operating temperatures.

<b><i>Detector</i></b>	<b><i>Spectral Range (cm<sup>-1</sup>)</i></b>	<b><i>Operating Temperature</i></b>
<b><i>MIR</i></b>		
MCT narrow band	5,000- 780	Liquid-nitrogen cooled
<b><i>NIR</i></b>		
InSb	9,600 - 1,850	Liquid-nitrogen cooled
<b><i>FIR</i></b>		
Si bolometer	370 - 10	Liquid-helium cooled
DLATGS	700 - 10	Room temperature cooled
<b><i>VIS</i></b>		
Si diode	25,000 - 9,000	Room temperature cooled

## 2.3 Laser excitation spectroscopy

Figure 2.10 shows the experimental block diagram for a laser excitation experiment. The output of a continuous-wave, single-mode, ring-type titanium:sapphire laser is split into two beams: one is introduced into a heated iodine vapor cell for the purpose of calibration, and the other beam is introduced from above the oven into the flame through a Brewster window on top of the oven. Excitation fluorescence could be observed through an infrared viewer during scanning. The fluorescence is collected and collimated using two lenses and is focused into a monochromator. The monochromator functions as a band-pass filter and its position is fixed while the laser is scanned through the spectral range of interest. As the laser was scanned, the optical signal from the monochromator was detected using a photomultiplier tube (PMT). Phase-sensitive detection is achieved by chopping the laser beam and feeding the signal from the PMT into a lock-in amplifier, which was phase-locked by a reference signal from the mechanical chopper. The output of the lock-in amplifier was then sent to the PC, which controlled the laser scanning.

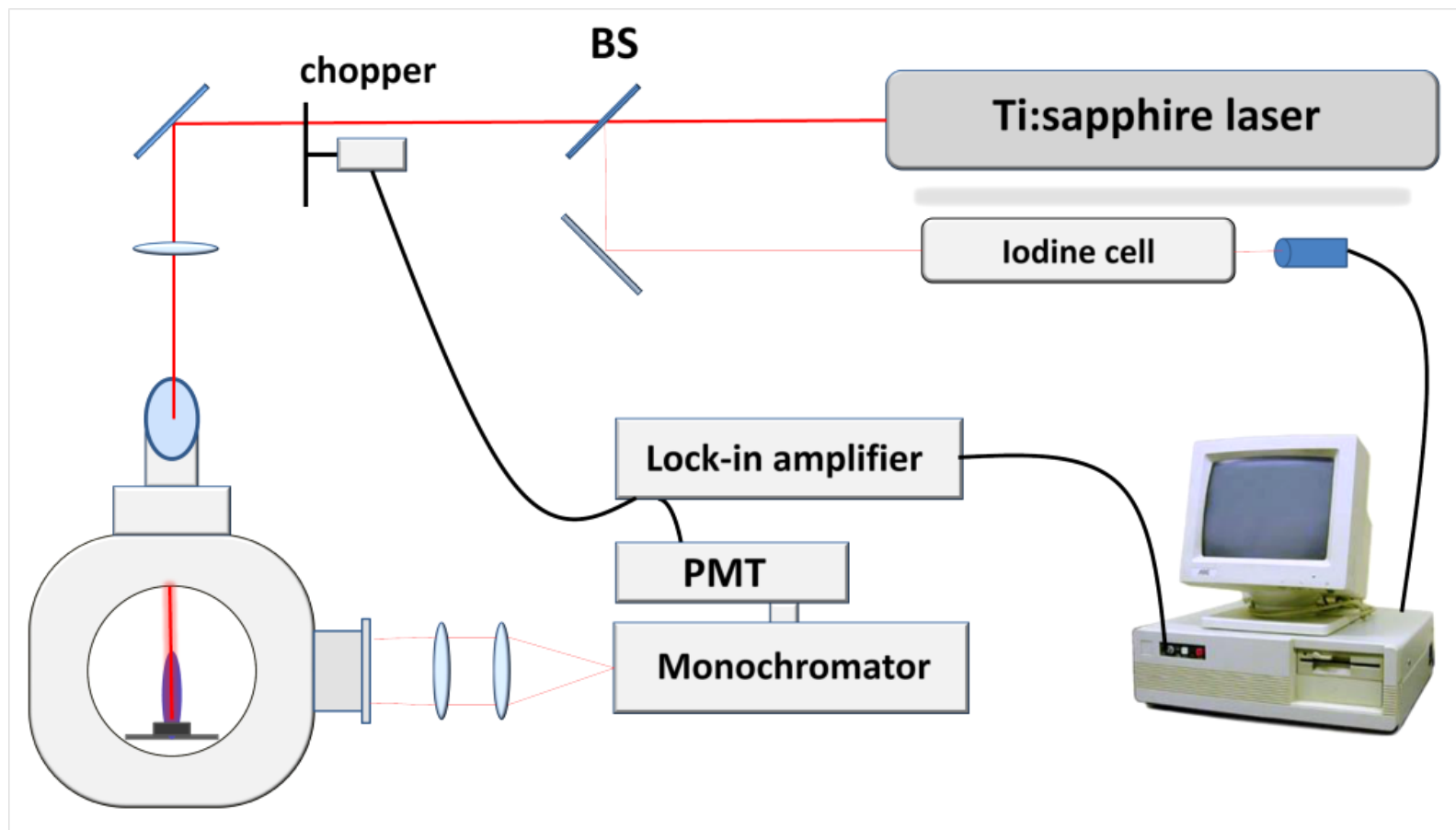


Figure 2.10 Schematic diagram showing the principle components of the laser excitation experiment in the Bernath laboratory; titanium:sapphire laser, beam splitter (BS), Iodine cell for calibration, Broida-type oven, Monochromator, power multiplier tube (PMT) and a computer.

# Chapter 3

## Fourier-transform Infrared Emission Spectroscopy of BO

### 3.1 Introduction

The semi-metal boron has a very rich chemistry and its compounds have many potential applications such as solid state fuel for air-breathing rockets<sup>4</sup>, hydrogen storage materials<sup>55</sup>, and the proton boron-11 fusion reaction<sup>56</sup>. As an intermediate product formed during the boron combustion process, boron monoxide (BO) has been extensively studied since 1925 when two emission band systems,  $A^2\Pi - X^2\Sigma^+$  and  $B^2\Sigma^+ - X^2\Sigma^+$  were first identified by Mulliken<sup>57</sup>. The two most important high resolution measurements on these electronic band systems were carried out by Coxon et al.<sup>58</sup> and Mélen et al.<sup>59</sup>.

In 1985 the microwave spectrum of BO was recorded by Tanimoto et al.<sup>60</sup>. More recently, an infrared measurement of the BO fundamental band was performed by Stancu et al.<sup>61</sup> using diode laser spectroscopy. However, the microwave and diode laser measurements only probed the  $v=0$  and  $v=1$  vibrational levels of the ground state of BO, respectively. Moreover, in the infrared laser study, only 19 lines and 12 lines for the fundamental bands of  $^{11}\text{B}^{16}\text{O}$  and  $^{10}\text{B}^{16}\text{O}$  were observed, respectively, and no hot bands were detected.

The Fourier transform measurements presented here contained the fundamental bands of both isotopic species,  $^{11}\text{BO}$  and  $^{10}\text{BO}$ , along with one hot band of the main isotopologue  $^{11}\text{BO}$  with 95, 72 and 64 lines, respectively. In the previous infrared work<sup>61</sup> the  $\text{O} + \text{BCl}_3$  reaction was used to synthesize BO, which required very specific experimental conditions.

## 3.2 Experimental

A full description of the high temperature tube furnace experiment setup can be found in chapter 2. In the present study, an alumina boat which contained a mixture of equal amounts of boron pieces and boron oxide ( $\text{B}_2\text{O}_3$ ) powder was placed in the centre of an alumina tube. The system was evacuated and steadily heated to  $1400^\circ\text{C}$  over a period of four hours. A piece of zirconia felt was placed between the alumina boat and the tube furnace to prevent the reaction of the reactant with the tube wall. The pumping speed was controlled using a valve and 2 Torr of argon buffer gas was introduced into the tube.

Initially the strong HBO  $\nu_3$  band<sup>63</sup> was observed at temperatures above  $1300^\circ\text{C}$ . The hydrogen atoms needed to form HBO presumably came from water impurities. BO molecules were then produced by applying a DC discharge (3 kV, 333 mA) to the tube containing HBO. The HBO molecule was the precursor of BO because the HBO signal decreased when the discharge was applied and BO was synthesised. A few mTorr of water vapour was introduced into the tube by passing the argon carrier gas through a glass bubbler to facilitate the production of HBO and BO. High resolution infrared emission spectra of  $^{11}\text{BO}$  and  $^{10}\text{BO}$  were recorded using the Bruker IFS 125 HR spectrometer using a  $\text{CaF}_2$  beam splitter and the MCT detector with a  $2200\text{ cm}^{-1}$  long pass filter to cover the  $1200 - 2100\text{ cm}^{-1}$  spectral range.

### 3.3 Results and discussion

Fig. 3.1 shows an expanded portion of the BO spectrum. The figure shows lines from the fundamental bands of  $^{11}\text{BO}$  and  $^{10}\text{BO}$  and the 2–1 hot band of  $^{11}\text{BO}$  with the rotational line assignments marked above. Other unassigned features in this spectrum are due to HBO. It should be noted that the  $^{11}\text{BO}$  lines are much more intense than the  $^{10}\text{BO}$  lines due to the 4:1 natural abundance ratio of the  $^{11}\text{B}$  and  $^{10}\text{B}$  isotopes. The observed lines display no spin doubling.

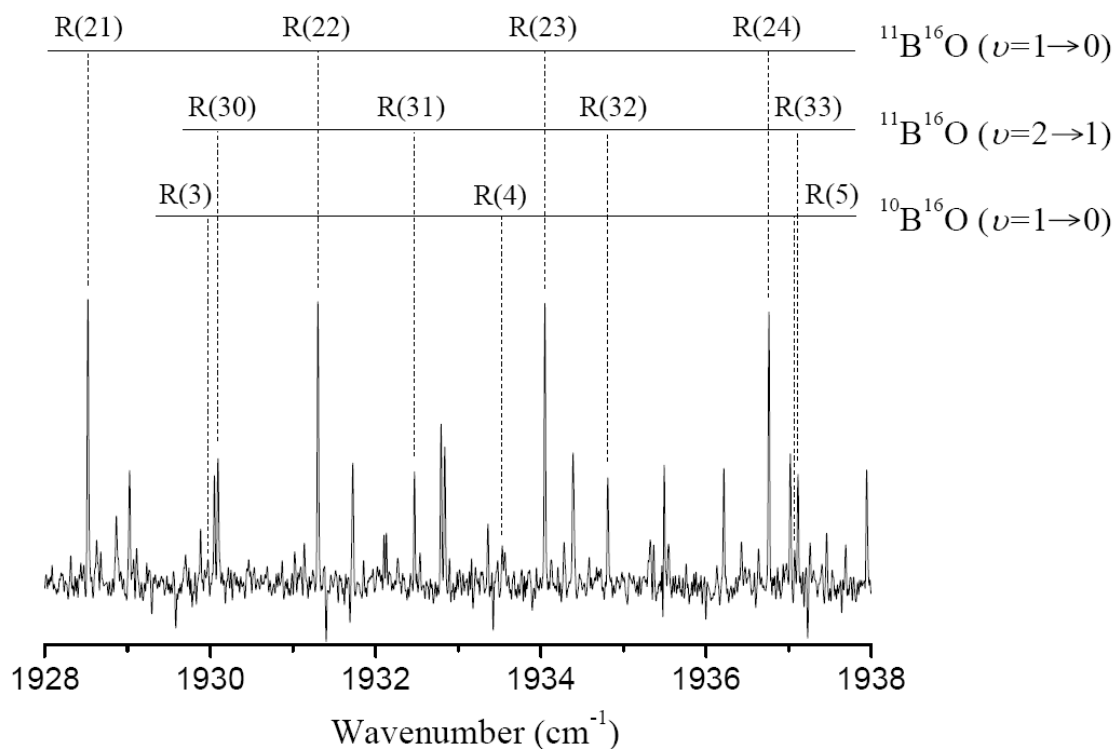


Figure 3.1: Emission lines from the two fundamental bands of  $^{11}\text{B}^{16}\text{O}$  and  $^{10}\text{B}^{16}\text{O}$ , and the  $\nu = 2-1$  hot band of the main isotopologue  $^{11}\text{B}^{16}\text{O}$  recorded by Fourier transform spectroscopy. The unmarked features are due to HBO.

The BO spectrum was calibrated with the NIST CO line list <sup>64</sup> and the absolute accuracy of this calibration is better than  $0.0002 \text{ cm}^{-1}$ . The

lines were fitted with a Voigt lineshape function using the M. Carleer's WSpectra program<sup>65</sup>. The general accuracy of strong blended lines is better than  $0.0004\text{ cm}^{-1}$ , but many lines are overlapped by HBO and were de-weighted. A Loomis-Wood program was then used to identify the bands with the  $J$  values assigned using lower state combination differences. The measured wavenumbers of the lines together with the microwave data and the diode laser data were then fitted as  ${}^1\Sigma - {}^1\Sigma$  transition. The accuracy of unblended infrared lines was taken as  $0.0004\text{ cm}^{-1}$  and the accuracy of the microwave lines was taken as  $0.03\text{ MHz}$ .

Band origins from Stancu et al.<sup>61</sup>,  $1861.92409(13)$  and  $1915.30674(14)\text{ cm}^{-1}$ , for  ${}^{11}\text{BO}$  and  ${}^{10}\text{BO}$  respectively, are in very good agreement with our fitted results,  $1861.9242(97)$  and  $1915.3071(09)\text{ cm}^{-1}$  (Table 3.1). Furthermore, the 2–1 band of  ${}^{11}\text{BO}$  was measured for the first time and the origin was derived from the least-squares fit to be  $1838.3773(68)\text{ cm}^{-1}$ . The vibrational parameters,  $\omega_e$  and  $\omega_e x_e$ , for  ${}^{11}\text{BO}$  were determined to be  $1885.4712(27)$  and  $11.7734(65)\text{ cm}^{-1}$ , respectively, which are listed in Table 3.2. For comparison, molecular parameters derived from previous diode laser and electronic spectral measurements are also provided in Table 3.2. The previously measured values for  $\omega_e$  do not satisfactorily agree with each other (see Table 3.2), presumably partly because different numbers of vibrational levels were included in their determination from the lower resolution electronic spectra.

Table 3.1: Fitted molecular parameters (in  $\text{cm}^{-1}$ ) for BO ( $X^2\Sigma^+$ )

	Present work	Infrared laser <sup>a</sup>	Electronic <sup>b</sup>	Microwave <sup>c</sup>
$^{11}\text{B}^{16}\text{O}$				
$B_0$	1.7734100(72)	1.773421(10)	1.772861(79)	1.77341071(15)
$D_0$	$6.3486(37)\times 10^{-6}$	$6.42(3)\times 10^{-6}$	$6.236(35)\times 10^{-6}$	$6.3871(9)\times 10^{-6}$
$B_1$	1.7568518(36)	1.756845(9)	1.756263(83)	
$D_1$	$6.3465(91)\times 10^{-6}$	$6.33(2)\times 10^{-6}$	$6.189(39)\times 10^{-6}$	
$B_2$	1.7402701(15)	–	1.739767(82)	
$D_2$	$6.3462(75)\times 10^{-6}$	–	$6.253(38)\times 10^{-6}$	
$v_0$	1861.9242(97)	1861.92409(13)	1861.965	
$v_1$	1838.3773(68)	–		
$^{10}\text{B}^{16}\text{O}$				
$B_0$	1.8776711(80)	1.877680(22)	1.87714(10)	1.87767255(22)
$D_0$	$7.1151(16)\times 10^{-6}$	$7.10(13)\times 10^{-6}$	$6.983(60)\times 10^{-6}$	$7.1986(12)\times 10^{-6}$
$B_1$	1.8596270(04)	1.859662(25)	$6.854(72)\times 10^{-6}$	
$D_1$	$7.1133(63)\times 10^{-6}$	$7.28(17)\times 10^{-6}$	$6.854(72)\times 10^{-6}$	
$v_0$	1915.3071(09)	1915.30674(14)	1915.36	

<sup>a</sup>Ref.<sup>61</sup>.<sup>b</sup>Ref.<sup>59</sup>.<sup>c</sup>Ref.<sup>60</sup>.

Table 3.2: Derived molecular parameters (in  $\text{cm}^{-1}$ ) for  $\text{BO}(X^2\Sigma^+)$ 

	Present work	Infrared laser <sup>a</sup>	Mélen et al. <sup>b</sup>	Coxon et al. <sup>c</sup>
$^{11}\text{B}^{16}\text{O}$				
$\omega_e$	1885.4712(27)	1885.552(28) <sup>d</sup>	1885.286(41)	1885.579(32)
$\omega_e x_e$	11.7734(65)	–	11.694(11)	11.825(14)
$B_e$	1.7816989(75)	1.781709(7)	1.781110(31)	1.781366(50)
$D_e$	6.3489(40) $\times 10^{-6}$	6.47(1) $\times 10^{-6}$	6.247(14) $\times 10^{-6}$	
$a_e$	1.65699(78) $\times 10^{-2}$	1.6576(14) $\times 10^{-2}$	1.6516(17) $\times 10^{-2}$	1.6444(19) $\times 10^{-2}$
$r_e(\text{Å})$	1.2045531(45)	1.204550(4)	–	–
$^{10}\text{B}^{16}\text{O}$				
$\omega_e$	–	1940.202(38) <sup>d</sup>	1940.308(23)	1940.218(41)
$\omega_e x_e$	–	–	12.4873(42)	12.433(19)
$B_e$	1.8866932(68)	1.886689(17)	1.886154(46)	1.886250(82)
$D_e$	7.1159(93) $\times 10^{-6}$	7.01(10) $\times 10^{-6}$	6.928(20) $\times 10^{-6}$	–
$a_e$	1.80441(76) $\times 10^{-2}$	1.8018(34) $\times 10^{-2}$	1.8107(13) $\times 10^{-2}$	1.7894(77) $\times 10^{-2}$
$r_e(\text{Å})$	1.2045605(87)	1.204561(9)	–	–

<sup>a</sup>Ref.<sup>61</sup>.<sup>b</sup>Ref.<sup>59</sup>.<sup>c</sup>Ref.<sup>58</sup>.<sup>d</sup>Ref.<sup>61</sup>. (Note: this value was calculated by using the anharmonicity parameter from Coxon et al.)

The rotational constant,  $B_0$  of 1.7734100(72) and 1.8776711(80)  $\text{cm}^{-1}$  for  $^{11}\text{BO}$  and  $^{10}\text{BO}$ , respectively, have been derived from the least-squares fit. Both results are in very good agreement with the values 1.77341071(15) and 1.87767255(22)  $\text{cm}^{-1}$  determined from the microwave measurements <sup>60</sup>. These results are also in good agreement with the infrared laser results, which are also listed in Table 3.1. By assuming the usual linear dependence of  $B_v$  with respect to  $v$  <sup>66</sup>, the  $B_e$  and  $a_e$  parameters were derived and the results are given in Table 3.2. The equilibrium bond length  $r_e$  were derived for both isotopic species, which are 1.2045531(45) and 1.2045605(87) Å for  $^{11}\text{BO}$  and  $^{10}\text{BO}$ , respectively.

### 3.3 Conclusion

The Fourier-transform infrared emission spectra of BO were recorded using a Bruker IFS 125 HR spectrometer. The observed spectrum of BO in the 1200 - 2100  $\text{cm}^{-1}$  region contains three bands: the fundamental bands of  $^{11}\text{BO}$  and  $^{10}\text{BO}$  and a hot band of  $^{11}\text{BO}$  with band origins measured to be 1861.9242(97), 1915.3071(09) and 1838.3773(68)  $\text{cm}^{-1}$ , respectively.

# Chapter 4

## High resolution vibration-rotation emission spectroscopy of HBS

### 4.1 Introduction

Transient molecules are unstable and short lived species which play an important role in atmospheric, combustion and biological processes. Studies of these species can provide information on reaction mechanisms, new synthetic procedures or synthesis of new classes of compounds. Thioborine, HBS, is a boron containing transient molecule isoelectronic to HCP and HCN, which have been investigated in detail through high resolution studies. HBS is a linear triatomic molecule for which some spectroscopic data are available from microwave and infrared studies but more spectroscopic data are needed to extract additional information about the structure of this radical.

The HBS molecule was first synthesized by Kirk and Timms<sup>67</sup> from the reaction of hydrogen sulfide gas with boron at a temperature of 1150-1300 °C under slow flow conditions at low pressure. The product was monitored using a time-of-flight mass spectrometer. The thioborine (HBS) produced from this reaction was not stable in the gas phase and decayed on the walls of the reaction chamber to form H-B-S polymers. The rotational spectrum of this novel molecule was later observed by Pearson and McCormick<sup>68</sup> who produced thioborine at about 1100 °C using a continuous flow system and recorded the millimeter-wave spectra of eight

isotopic species. From the observed rotational line frequencies they derived spectroscopic constants and bond lengths for the ground state for each isotopologue and concluded that HBS is a linear molecule. In a subsequent study, Pearson et al.<sup>69</sup> recorded the zero-field microwave spectra of  $J=0 \rightarrow J=1$  transition of  $\text{H}^{11}\text{B}^{32}\text{S}$ ,  $\text{D}^{11}\text{B}^{32}\text{S}$  and  $\text{D}^{10}\text{B}^{32}\text{S}$  species in order to study the molecular Zeeman effects in these species. From this study they provided accurate values for the nuclear hyperfine coupling constants and electric dipole moments.

Sams and Maki<sup>70</sup> recorded the high resolution spectra of HBS in the 2720-2750  $\text{cm}^{-1}$  region and provided infrared measurements of the  $\nu_1$  vibrational fundamental of  $\text{H}^{11}\text{B}^{32}\text{S}$  and its minor isotopologues. The observed values of  $\nu_1$  were used in conjunction with the ground state distortion and  $l$ -doubling constants to determine the force constants for the molecule in order to estimate the frequencies of the unobserved vibrational fundamentals. Their calculated values were 2769, 635, and 1194  $\text{cm}^{-1}$  for the  $\nu_1$ ,  $\nu_2$ , and  $\nu_3$  fundamentals, respectively. Uncertainty in calculated values was estimated to be in the range of 5-10%. In another infrared study of HBS, Turner and Mills<sup>71</sup> have observed the infrared spectrum of the  $\nu_1$  and  $\nu_3$  fundamentals of HBS and DBS using a Nicolet Fourier transform spectrometer at a resolution of 0.1  $\text{cm}^{-1}$ . They found the intensity of the  $\nu_1$  and  $\nu_3$  fundamental bands to be comparable in their spectra. They also attempted to record the  $\nu_2$  fundamental band which falls in the region in which their detector was quite sensitive but were surprised by the absence of any  $\nu_2$  bands. From the complete absence of even the Q branch lines of this band they concluded that the vibrational transition moment of  $\nu_2$  was at least 20 times weaker than for  $\nu_3$ . From the results of this analysis in conjunction with the earlier results, they determined the equilibrium structure [ $r_e(\text{B-H})=1.16989(12)$  Å,  $r_e(\text{B-S})=1.5978(3)$  Å] and harmonic and anharmonic force fields for HBS.

The ground state rotational spectra of  $\text{H}^{11}\text{B}^{33}\text{S}$  and  $\text{H}^{10}\text{B}^{33}\text{S}$  isotopic species of thioborine have been observed by Bizzocchi et al.<sup>72</sup> in the

millimeter-wave region by a high temperature reaction of hydrogen sulfide with crystalline boron. The analysis of hyperfine structure produced by the  $^{10}\text{B}$ ,  $^{11}\text{B}$  and  $^{33}\text{S}$  in thioborane molecule has provided quadrupole coupling constants. They also obtained measurements of many higher  $J$  rotational transitions of the most abundant HBS isotopologues in order to improve their ground state spectroscopic constants. In another study Bizzocchi and Degli Esposti<sup>73</sup> observed the millimeter and submillimeter-wave spectra of four vibrationally excited states of HBS and DBS lying below  $1500\text{ cm}^{-1}$ . These measurements in conjunction with the earlier infrared results were employed to calculate more precise anharmonic force constants and equilibrium bond lengths. In a most recent study Bizzocchi et al.<sup>74</sup> have observed the millimeter-wave spectra of HBS and DBS in the vibrational ground state using the Lamb-dip technique and obtained the improved values of the  $^{10}\text{B}$  and  $^{11}\text{B}$  hyperfine parameters in HBS and also determined the deuterium electric quadrupole coupling constant.

There are several studies of the photoelectron spectrum of HBS, for example by Fehner and Turner<sup>75</sup>, Kroto et al.<sup>76</sup>, and Suffolk et al.<sup>77</sup>. The first photoelectron spectrum of HBS was obtained by Fehner and Turner<sup>75</sup> who obtained the ionization potentials of HBS and vibrational frequencies in the excited states of  $\text{HBS}^+$ . This study was followed by a new observation of the photoelectron spectrum of HBS by Kroto et al.<sup>76</sup> at a temperature of  $1100\text{ }^\circ\text{C}$  from the reaction between  $\text{H}_2\text{S}$  and crystalline boron. From this study they determined accurate values for the first, second and third adiabatic ionization potentials and confirmed that the ion is linear in all the states observed. In another study, the photoelectron spectra of XBS ( $\text{X}=\text{H}, \text{F}, \text{Cl}, \text{Br}$ ) were measured by Suffolk et al.<sup>77</sup>, in order to analyze the general trend in the ionization energies as a function of halide substituent using self consistent molecular orbital calculations. Chau et al.<sup>78</sup> have applied a Frank-Condon analysis of the corresponding photoelectron bands of HBS and ClBS to derive the structural parameters of the molecules in the corresponding ionic states and have compared the vibrational frequencies and force constants in various electronic states.

Ennis and Hitchcock<sup>79</sup> and Hitchcock et al.<sup>80</sup> have demonstrated the application of the inner shell excitation spectroscopy for the observation of HBS and HBO transient species in gas phase.

There are several theoretical calculations on the geometry, equilibrium structure and molecular properties of transient species. Talaty et al.<sup>81</sup> have studied the potential energy surfaces of several such species and their isomeric forms using ab initio molecular orbital calculations. They have concluded that while HBO and HBS are linear, their isomeric forms HOB and HSB should exist as bent molecules. So far the HOB and HSB molecules have not been detected experimentally. There are several studies on the spectroscopic properties of HBS and other molecules of this family. Gropen and Wisløff-Nilssen<sup>82</sup> has performed an ab initio calculation in order to determine their equilibrium structure and molecular properties of HBS while Puzzarini et al.<sup>83</sup> have recently performed similar calculations on XBS and XCP (X=H, F, Cl). Nguyen and Ruelle<sup>84</sup> have performed a SCF study of carbon-phosphorous and boron-sulphur bond in RCP and RBS molecules with (R=H, CH<sub>3</sub>, NH<sub>2</sub>, OH, F & Cl). Lee et al.<sup>85</sup> have performed an ab initio calculation on the X<sup>1</sup>Σ<sup>+</sup> states of HBS and FBS and the X<sup>2</sup>Σ<sup>+</sup> and A<sup>2</sup>Σ<sup>+</sup> states of HBS<sup>+</sup> and FBS<sup>+</sup> with large basis sets. Their calculated geometries, vibrational frequencies and force constants agreed well the observed values. More recently Francisco<sup>86</sup> has performed an ab initio study on XBS<sup>+</sup> (X=H, F & Cl) to investigate their structure, bonding, vibrational spectra and energetic properties along with those of corresponding XBS neutral species.

In the present work we report on the high resolution study of the  $\nu_1$  and  $\nu_3$  fundamentals and a large number of hot bands of H<sup>11</sup>BS and H<sup>10</sup>BS species using Fourier transform infrared emission spectroscopy. The assignment of many of the hot bands was greatly facilitated by the results of ab initio calculations. This analysis provides the spectroscopic constants for a large number of vibrational levels of H<sup>11</sup>BS and H<sup>10</sup>BS species.

## 4.2 Ab initio prediction of the vibration-rotation energy levels

(All of the computational results presented in chapter 4 were derived by Prof. Hui Li using the MOLPRO-2010 package of ab initio programs, and is briefly explained here.)

The equilibrium structure and three-dimensional potential energy surface of HBS were calculated using the coupled-cluster method including single and double excitations and a perturbation correction due to connected triple excitations with the F12a approximation [CCSD(T)-F12a] in conjunction with the correlation-consistent valence basis sets up to triple-zeta quality (cc-pVTZ-F12). The simple and efficient CCSD(T)-F12x approximations (x=a,b) were initially proposed by Adler et al.<sup>87</sup>. Later in 2009, this method was explained in more detail and extended to open-shell systems by Knizia et al.<sup>88</sup>. They also carried out extensive benchmark calculations on molecular properties including reaction energies, atomization energies electron affinities, ionization potentials equilibrium geometries, and harmonic vibrational frequencies. This calculation demonstrated that the results obtained using AVTZ basis sets were already better than those using conventional CCSD(T) method with AV5Z basis sets.

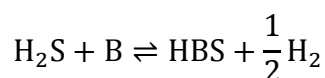
To determine the shape of the potential-energy surface of HBS, the total energies were calculated at CCSD(T)-F12/cc-pVTZ-F12 level at 6000 points in the vicinity of the equilibrium configuration. The vibration-rotation energy levels of HBS ranging up to about 6000 cm<sup>-1</sup> above the ground vibrational state were determined for the rotational quantum number  $J=0-20$ . The spectroscopic constants were obtained by fitting the ro-vibrational transitions with the following equation:

$$F_{v,J} = B_v J(J + 1) - D_v J^2(J + 1)^2 \pm \frac{1}{2} [qJ(J + 1) + q_D J^2(J + 1)^2],$$

Subsequently, the ab initio rotational constants,  $B$ , were determined and used to guide our assignments.

### 4.3 Experimental details

Thioborine (HBS) was first identified by Kirk and Timms<sup>67</sup> using mass spectrometry. They found HBS to be the main product of the gas phase reaction of hydrogen sulphide with crystalline boron under low pressure at the temperature of 1150-1130 °C. The following is the reaction formula as provided by them:



A small amount of  $\text{BS}^+$  and  $\text{B}^+$  fragment ions from HBS (less than 5% of the intensity of HBS), were also detected. This approach was later used to produce gas phase HBS in many subsequent studies<sup>68-71, 73, 76, 79</sup>. In the present study, we tried a different approach. Reagent grade (Sigma-Aldrich) carbon disulfide ( $\text{CS}_2$ ), and water were used as precursors to produce HBS.



The molecules were produced in a high temperature furnace, a full description of which can be found in chapter 2. In the current study, an alumina boat containing about 2 gram crystalline boron pieces was placed in the centre of an alumina tube inside the furnace. The system was evacuated and gradually heated to 1300 °C over a period of 5 hours to prevent thermal shock of the tube. This temperature was maintained stable while recording the spectra. The pumping speed was controlled using a stainless steel valve and about 2 Torr of argon was introduced into the tube as buffer gas.

Reagent grade  $\text{CS}_2$  vapor from a liquid reservoir was then introduced. In order to limit the formation of HBO, the reservoir was

pumped for two minutes prior to the experiment to remove all dissolved oxygen from the CS<sub>2</sub>. As observed previously<sup>89</sup>, HBO was generated from water impurities. Initially, weak HBS and HBO  $\nu_1$  bands were observed. A few mTorr water vapor was introduced into the tube by passing the argon carrier gas through a glass bubbler to facilitate the production of HBS. In order to maximize the signal, we tweaked a few experimental conditions, such as the pumping speed and the amount of water vapor. Finally, the high resolution infrared emission spectra of HBS were recorded using a Bruker IFS-125HR spectrometer.

The spectra of HBS  $\nu_1$  and  $\nu_3$  bands were recorded separately in two regions and the experimental conditions are listed in Table 4.1. The choice of these two regions was a consequence of the available optical filter and constituent materials of the system. The first region covered the spectral range of 1750-4000 cm<sup>-1</sup> and was recorded with calcium fluoride (CaF<sub>2</sub>) windows, a CaF<sub>2</sub> focusing lens (f=10 cm), a CaF<sub>2</sub> beam splitter and a liquid nitrogen cooled InSb detector. The high wavenumber cutoff was due to the long pass filter and the low wavenumber cutoff was limited by the InSb detector. Figure 4.1 shows the HBS  $\nu_1$  band in the first region with the baseline flattened. HBO  $\nu_1$  band was also recorded as an impurity and the band intensity is around half of that of HBS. Although the R branch of the HBS and P branch of HBO are overlapped, these two species can be easily distinguished because the rotational constant B of HBO is nearly twice the B value of HBS. Strong CO emission band is also found at 2117 cm<sup>-1</sup> and is almost 50 times stronger than the HBS  $\nu_1$  band. A few weak spectral lines found near 3600 cm<sup>-1</sup> region were identified belonging to the  $2\nu_3$  band of HBO by comparing to our pure HBO spectrum taken earlier in this region.

The second region covered the spectral range of 750-1150 cm<sup>-1</sup>. This region was recorded with thallium bromoiodide (KRS-5) windows, a zinc selenide (ZnSe) focusing lens (f~7 cm), a potassium bromide (KBr) beam splitter and a liquid nitrogen cooled mercury-cadmium telluride (MCT)

detector. Figure 4.2 shows the spectrum of HBS  $\nu_3$  band with the baseline flattened. The CS impurity spectrum was also present in the same region. The ratio of the intensities of these two bands is around 3:1. The  $2\nu_2$  overtone band of HBS was not observed in this region.

The resolution listed in Table 4.1 was chosen based on the Doppler and pressure broadening of observed rotational lines. The signal-to-noise ratio (SNR) of the strongest lines of  $\nu_1$  and  $\nu_3$  bands of HBS were about 40 and 60, respectively.

Table 4.1 Experimental conditions.

Experimental Parameters	Region 1	Region 2
Spectral region (cm <sup>-1</sup> )	1750-4000	750-1750
Detector	InSb	MCT
Beam splitter	KBr	KBr
Windows	CaF <sub>2</sub>	KRS-5
Lens	CaF <sub>2</sub>	ZnSe
Scans	320	160
Resolution (cm <sup>-1</sup> )	0.02	0.005
Aperture (mm)	2	2
Zerofilling factor	×16	×16
Temperature (°C)	1400	1400

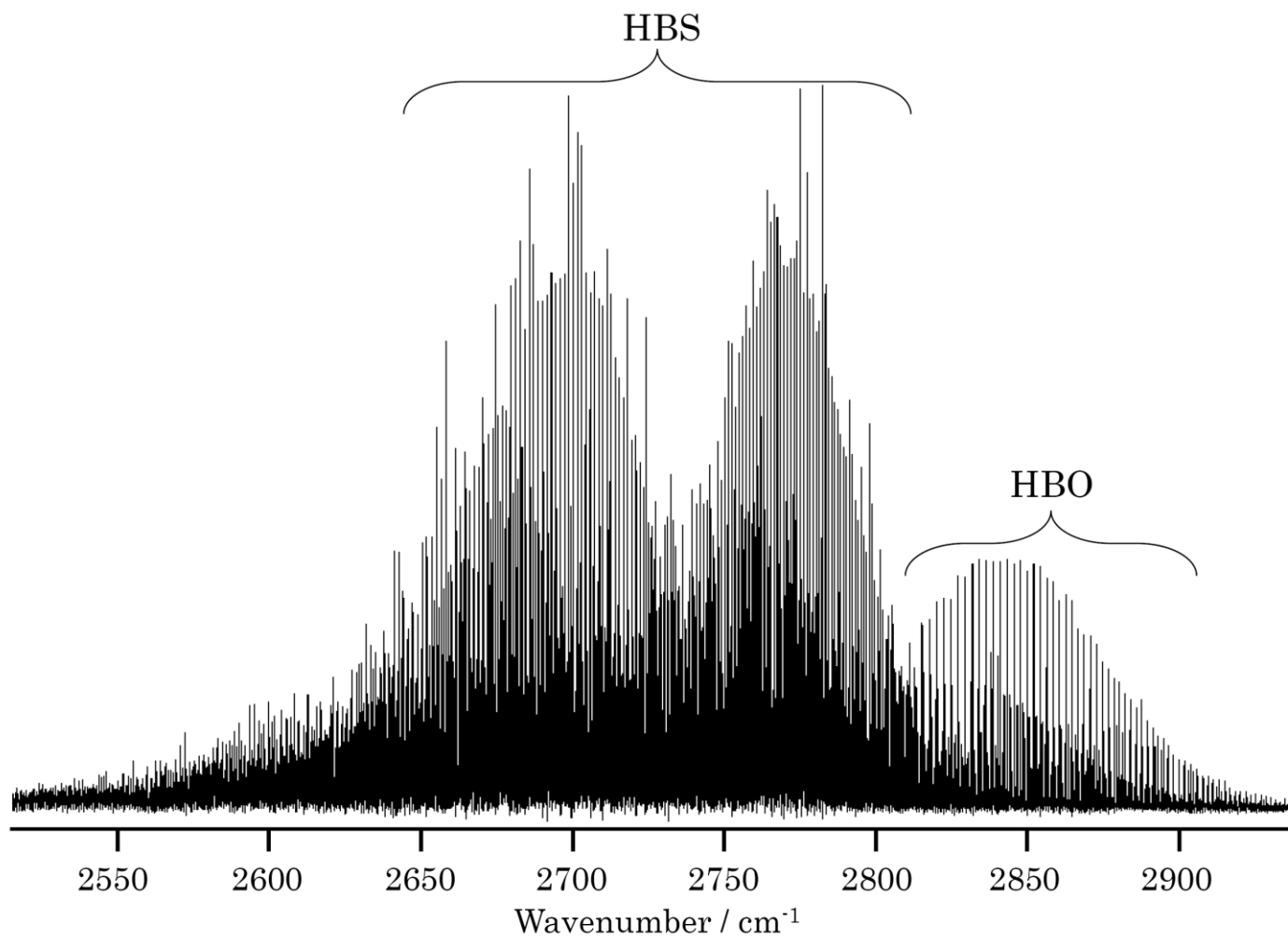


Figure 4.1: Overview of the FTIR spectrum of  $\nu_1$  fundamental of HBS with baseline flattened. HBO spectrum was also present as an impurity.

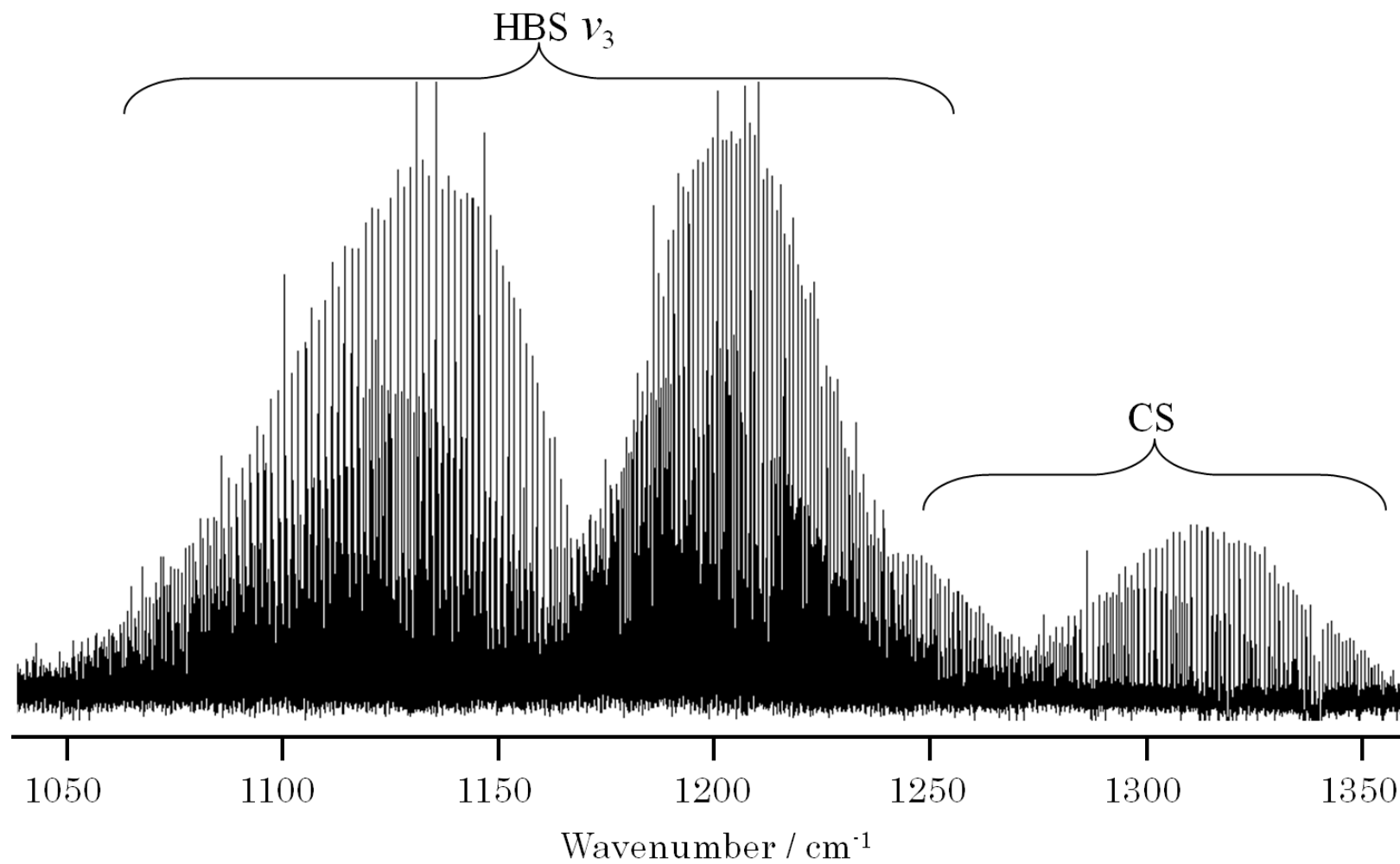


Figure 4.2: Overview of the FTIR spectrum of  $\nu_3$  fundamental of HBS with baseline flattened. HBO spectrum was also present as an impurity.

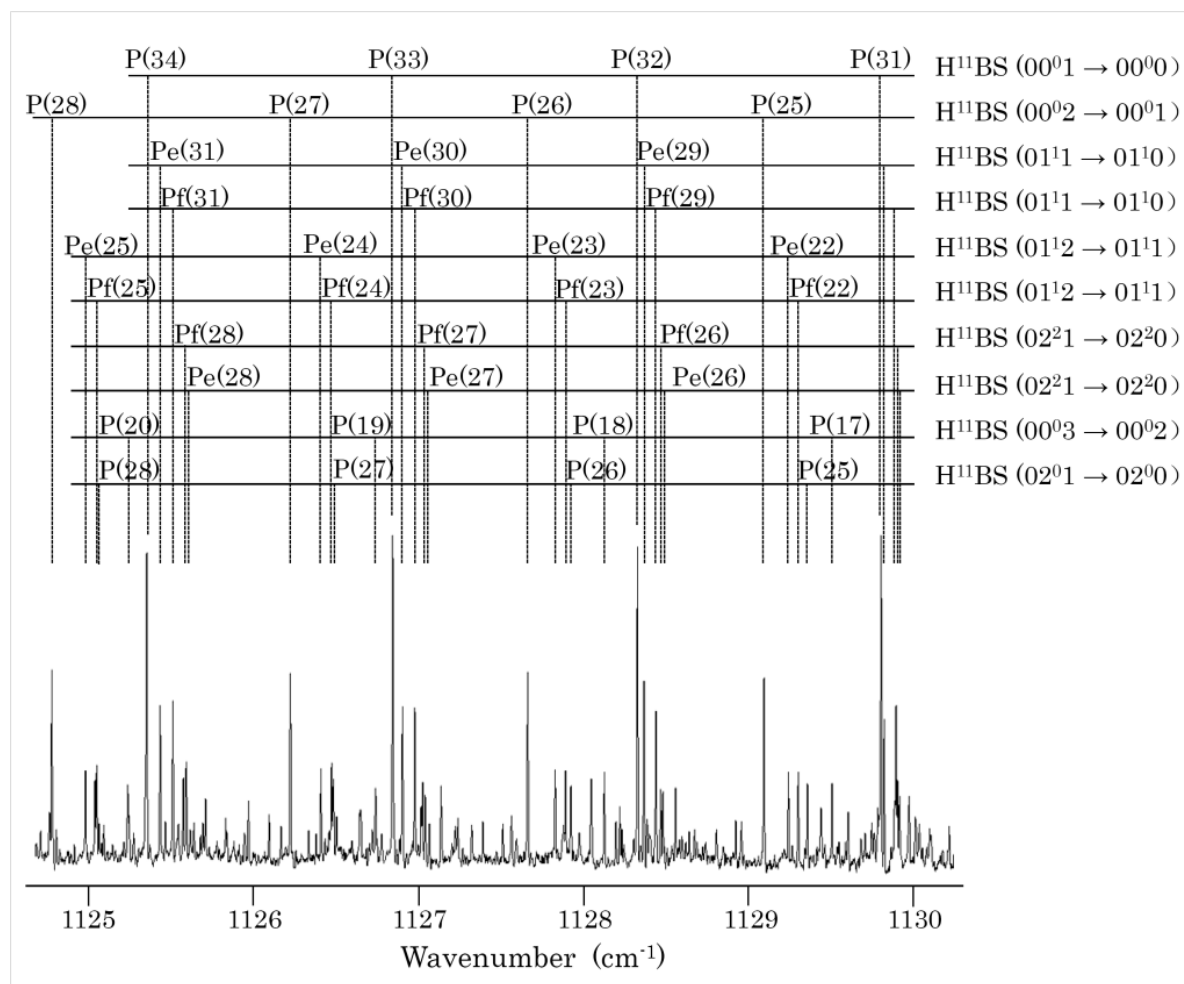


Figure 4.3: An expanded portion of the HBS spectrum marking some rotational lines of H<sup>11</sup>BS. The nature abundance ratio of the <sup>11</sup>B and the <sup>10</sup>B isotopes is 4:1.

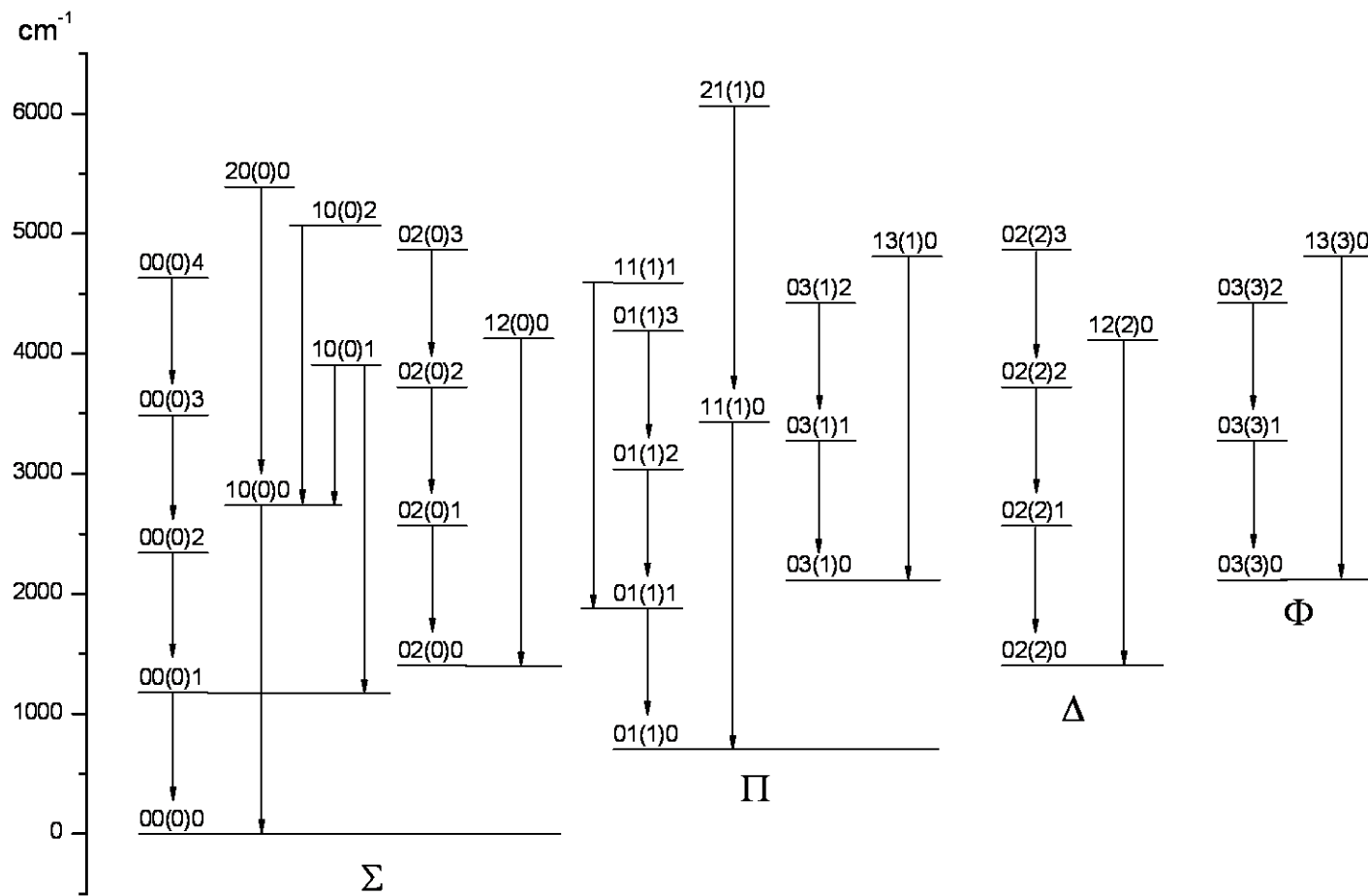


Figure 4.4: Observed energy levels and transitions of  $\text{H}^{11}\text{B}^{32}\text{S}$ .

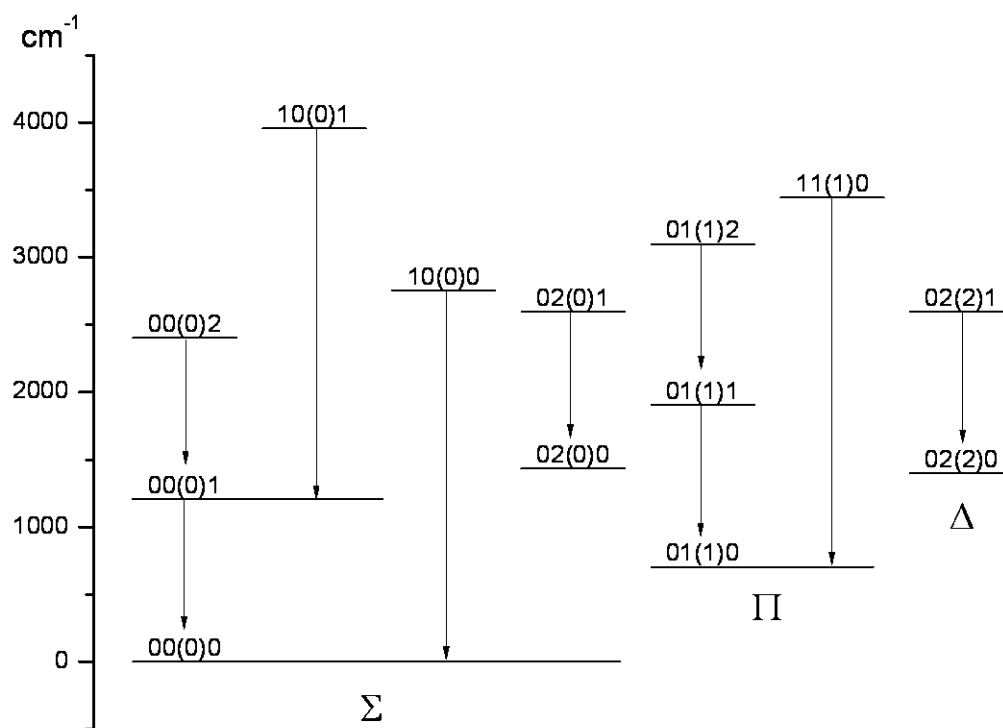


Figure 4.5: Energy level diagram of observed transitions of  $\text{H}^{10}\text{B}^{32}\text{S}$ .

## 4.4 Analysis of the spectra

The WSpectra program written by Carleer<sup>65</sup> was used to determine the line positions. At a temperature of 1300 °C, the spectrum contains strong impurity of CO emission lines, which were used to calibrate the spectrum. Based on the NIST CO line list<sup>90</sup>, the absolute accuracy of our calibration is better than 0.0001 cm<sup>-1</sup>. A color Loomis-Wood program was used to pick out the branches in different bands. The absolute rotational assignments were determined using lower states combination differences.

Figures 4.4 and 4.5 show the energy level diagrams of the observed levels of H<sup>11</sup>BS and H<sup>10</sup>BS species, respectively. A least-squares fit was performed for each assigned band using a lsqWIN program. The following customary energy-level expression for linear triatomic molecules<sup>48</sup> was used in the analysis:

$$E(J) = G(v_1, v_2^l, v_3) + BJ(J + 1) - DJ^2(J + 1)^2 \pm \frac{1}{2}[qJ(J + 1) + q_D J^2(J + 1)^2],$$

Eq. 4.1

where  $G(v_1, v_2^l, v_3)$  is the vibrational energy of the  $(v_1, v_2^l, v_3)$  state relative to the zero-point energy (ZPE),  $G(0,0^0,0)$ ;  $l$  is the vibrational angular momentum quantum number, where  $l = 0,1,2,3,\dots$  represents for  $\Sigma^+, \Pi, \Delta, \Phi$  states, respectively;  $q$  and  $q_D$  are the  $l$ -type doubling constants, where  $q = q_D = 0$  for  $\Sigma$  and  $\Phi$  states,  $q, q_D \neq 0$  for  $\Pi$  state,  $q = 0, q_D \neq 0$  for  $\Delta$  state. High order centrifugal distortion constants,  $H$ , were needed for bands having high  $J$  rotational lines. The higher order constant  $q_H$  is needed for  $\Phi$  state. The upper and lower sign refer to the  $e$  and  $f$  parities, respectively. The vibrational assignments of the hot bands were guided strongly by the results of the variational calculations. Specifically, the assignments were accomplished by shifting the  $J$  assignments until the upper and lower state B values, and the band origins are all matched with

the predicted values from variational calculations. A comparison of the fitted spectroscopic parameters and the values predicted from the variational calculations are provided in Tables 4.2 to 4.9. For the reason that neither  $\nu_2$  bending mode nor any combination bands were observed, many levels are ‘hanging’ and their absolute energies could not be determined experimentally. For the sake of clarity, all of the assigned bands are divided into 4 groups with bands in each group connected by levels in common.

#### 4.4.1. Observed $(\nu_1, \nu_2^l, \nu_3)$ states with $\nu_2 = 0$

The  $\nu_1$  and  $\nu_3$  fundamentals,  $10^00-00^00$  and  $00^01-00^00$ , were easy to identify for the main isotopologue  $\text{H}^{11}\text{B}^{32}\text{S}$ , because of their strongest intensity in the two respective regions. These bands consist of P and R branches appearing with almost similar intensities and around 160 rotational lines were measured in each of these bands. A combined fit including the latest microwave data<sup>73</sup> was performed and the band centers of the  $\nu_1$  and  $\nu_3$  fundamentals were measured as  $2735.80671(13) \text{ cm}^{-1}$  and  $1172.369301(19) \text{ cm}^{-1}$ , respectively. A value of  $2735.7969(22) \text{ cm}^{-1}$  was determined by Sams and Maki<sup>70</sup> for the  $\nu_1$  fundamental in their high resolution infrared study. Our measured band center is about  $0.0098 \text{ cm}^{-1}$  higher than the value determined by from Sams and Maki<sup>70</sup> which is larger than their quoted uncertainty of  $\pm 0.0022 \text{ cm}^{-1}$ . For the  $\nu_3$  fundamental, the band center reported by Turner and Mills<sup>71</sup> is  $1172.389(11) \text{ cm}^{-1}$  which is consistent with our results within the experimental error. The  $10^00-00^00$  and  $00^01-00^00$  bands were also observed for the  $^{10}\text{B}$  species with its natural abundance,  $^{11}\text{B}:^{10}\text{B}=4:1$ . The band centers of the two fundamentals were measured as  $2751.44311(40) \text{ cm}^{-1}$  and  $1207.06757(4) \text{ cm}^{-1}$  for  $\text{H}^{10}\text{B}^{32}\text{S}$ , compared to  $2751.4349(28) \text{ cm}^{-1}$  for  $\nu_1$  by Sams and Maki<sup>70</sup> and  $1207.073(8) \text{ cm}^{-1}$  for  $\nu_3$  by Turner and Mills<sup>71</sup>.

As shown in Figures 4.4 and 4.5, seven  $v_2 = 0$ ,  $\Sigma^+ - \Sigma^+$ , hot bands originating from levels 00<sup>0</sup>2, 00<sup>0</sup>3, 00<sup>0</sup>4, 20<sup>0</sup>0, 10<sup>0</sup>1 and 10<sup>0</sup>2 for H<sup>11</sup>B<sup>32</sup>S, and two  $\Sigma^+ - \Sigma^+$  hot bands originating from levels 00<sup>0</sup>2 and 10<sup>0</sup>1 for H<sup>10</sup>B<sup>32</sup>S were identified. These hot bands were assigned by matching both band origins and rotational constants to calculated values. Together with two fundamentals, 10<sup>0</sup>0-00<sup>0</sup>0 and 00<sup>0</sup>1-00<sup>0</sup>0 bands, the observed infrared  $v_2 = 0$ ,  $\Sigma^+ - \Sigma^+$ , bands were combined with microwave data<sup>73</sup> to determine the final sets of spectroscopic parameters and the results for the H<sup>11</sup>BS and H<sup>10</sup>BS isotopologues are collected in Tables 4.2 and 4.7, respectively. The differences between fitted and calculated values are also listed. A good agreement is found between experimental and calculated values. A difference of a few wavenumbers is found for the band origins, while for the rotational constants, a shift of  $\delta=0.0013$  cm<sup>-1</sup> has been found for each vibrational level of H<sup>11</sup>B<sup>32</sup>S. After subtracting  $\delta$  from the calculated values, the differences were reduced to an order of 10<sup>-5</sup> cm<sup>-1</sup>. This constant shift is presumably caused by the overestimation of the energy using the CCSD(T)-F12a method. During the least-squares fit, it was noted that the inclusion of high order centrifugal distortion constant H for the levels, 00<sup>0</sup>0, 00<sup>0</sup>1, 00<sup>0</sup>2, 00<sup>0</sup>3, 10<sup>0</sup>0 and 10<sup>0</sup>1, reduces the standard deviation of the fit by a factor of 2.

#### 4.4.2 Observed ( $v_1, v_2^l, v_3$ ) states with $v_2 = 1$

As shown in Figure 4.4, total six  $\Pi - \Pi$  ( $v_2 = 1$ ) bands associated with seven vibrational levels (01<sup>1</sup>0, 01<sup>1</sup>1, 01<sup>1</sup>2, 01<sup>1</sup>3, 11<sup>1</sup>0, 21<sup>1</sup>0, 11<sup>1</sup>1) were assigned for H<sup>11</sup>B<sup>32</sup>S. Similarly in Figure 4.5, three  $\Pi - \Pi$  ( $v_2 = 1$ ) bands associated with four vibrational levels (01<sup>1</sup>0, 01<sup>1</sup>1, 01<sup>1</sup>2, 11<sup>1</sup>0) were assigned for H<sup>10</sup>B<sup>32</sup>S. Each of these bands consists of two P branches (P<sub>e</sub> and P<sub>f</sub>) and two R branches (R<sub>e</sub> and R<sub>f</sub>). The P branches split at P<sub>e</sub>/P<sub>f</sub>(2) and R branches split at R<sub>e</sub>/R<sub>f</sub>(1). Transition frequencies in the bending state 01<sup>1</sup>0 had been previously measured in the millimeter- and submillimeter-wave region.<sup>73</sup> Our choice of *e, f* parities was based on the

results of this study. The millimeter-wave data were combined with present infrared measurements to determine the spectroscopic constants listed in Tables 4.3 and 4.8 for H<sup>11</sup>BS and H<sup>10</sup>BS, respectively. The high- $J$  transitions recorded allowed us to determine the  $l$ -type doubling constant  $q$  and  $q_D$  with a sufficient precision. As shown in Figure 4.3, the intensity of the strongest  $\Pi - \Pi$  band in the  $\nu_3$  region is approximately half the intensity of the  $\nu_3$  fundamental.

#### 4.4.3 Observed $(\nu_1, \nu_2^l, \nu_3)$ states with $\nu_2 = 2$

For the vibrational states with  $\nu_2 = 2$ , the vibrational angular momentum quantum number  $l$  assumes the values 0 and  $\pm 2$ , thus giving rise to a non-degenerate level  $\Sigma^+$  and a doubly degenerate level  $\Delta$ . The splitting of the  $\Delta$  levels primarily arise from the effect of  $l$ -resonance. The  $l$ -resonance has been observed in the ro-vibrational spectra of many linear triatomic molecules, such as BeH<sub>2</sub>,<sup>91</sup> MgH<sub>2</sub>,<sup>92</sup> FBS<sup>93</sup>. Initially discovered by Amat and Nielsen<sup>94, 95</sup>, the theory of  $l$ -resonance were systemically studied and applied to HCN and DCN microwave and infrared measurements by Maki and Lide<sup>96</sup>.

A brief description of the theory of  $l$ -resonance is discussed here. Taking the  $02^00 \sim 02^20$  interaction as an example, the interaction matrix elements are:

$$\begin{aligned} \langle \nu_1 \nu_2^0 \nu_3, J | H' | \nu_1 \nu_2^2 \nu_3, J \rangle &= \langle J, \Lambda = 0, \Omega = 0 | -B(R)(J^+)^2(L^-)^2 e | J, \Lambda = 2, \Omega = 2 \rangle \\ \langle \nu_1 \nu_2^0 \nu_3, J | H' | \nu_1 \nu_2^2 \nu_3, J \rangle & \\ &= \langle J, \Lambda = 0, \Omega = 0 | -B(R)(J^+)^2(L^-)^2 e | J, \Lambda = -2, \Omega = -2 \rangle \end{aligned}$$

These two matrix elements are equal and it is only necessary to consider the positive  $\Omega$  values. Therefore, the  $02^00 \sim 02^20$  interaction is characterized by following matrix element:

$$\langle \nu_1 \nu_2^0 \nu_3, J | H' | \nu_1 \nu_2^2 \nu_3, J \rangle = \eta [J(J+1) - 2](J+1)^{\frac{1}{2}}$$

If the centrifugal distortion of the perturbation matrix element were included:

$$\langle v_1 v_2^0 v_3, J | H'_{CD} | v_1 v_2^2 v_3, J \rangle = \eta_D [J(J+1)][J(J+1)(J-1)(J+2)]^{1/2}$$

Finally, the following  $2 \times 2$  matrix elements were used to model the  $l$ -type resonance:

$$H = \begin{pmatrix} E_{\Sigma^+}^0 & W_{20} \\ W_{20} & E_{\Delta}^0 \end{pmatrix}$$

The diagonal matrix elements are the ordinary energy expression for  $\Sigma^+$  and  $\Delta$  states:

$$E_{\Sigma^+}^0 = G(v_1, v_2^0, v_3) + B_{\Sigma^+} J(J+1) - D_{\Sigma^+} J^2(J+1)^2,$$

$$E_{\Delta}^0 = G(v_1, v_2^2, v_3) + B_{\Delta} J(J+1) - D_{\Delta} J^2(J+1)^2,$$

While the off-diagonal term representing the interactions has the following form:

$$W_{20} = [\eta + \eta_D J(J+1)] \times [J^2(J+1)^2 - 2J(J+1)]^{1/2}$$

where the difference between  $\Sigma^+$  and  $\Delta$  state origins is equal to  $4g_{22}$ .

The PGOPHER program was adopted to fit the  $l$ -type resonance using the above  $2 \times 2$  interaction matrix. Firstly, the line positions of the  $\Sigma - \Sigma$  dyad:  $02^01 - 02^00$ ,  $02^02 - 02^01$ ,  $02^03 - 02^02$ ,  $12^00 - 02^00$ ; and the interacting  $\Delta - \Delta$  dyad:  $02^21 - 02^20$ ,  $02^22 - 02^21$ ,  $02^23 - 02^22$ ,  $12^20 - 02^20$ , together with their  $J$  assignments, were inserted into the PGOPHER program. Perturbation matrix elements  $\langle v_1 v_2^0 v_3, J | H' | v_1 v_2^2 v_3, J \rangle$  and  $\langle v_1 v_2^0 v_3, J | H'_{CD} | v_1 v_2^2 v_3, J \rangle$  described above were included in the fit for every two states which are interacting. As shown in the energy level diagram, the vibrational energies of the  $02^00$  ( $\Sigma$ ) and  $02^20$  ( $\Delta$ ) states could not be determined directly from the experiment. Therefore, we fixed the energy of the  $02^00$  ( $\Sigma$ ) state to zero and the relative energy of  $02^20$  ( $\Delta$ ) state was determined from the interaction. During our fit, it is found that  $12^20 -$

$02^20$  and  $12^00 - 02^00$  transitions have larger residuals than other  $\nu_2 = 2$  transitions. Further investigation showed that the  $06^00$  ( $\Sigma$ ) state is predicted to be approximately  $20 \text{ cm}^{-1}$  above  $12^00$  ( $\Sigma$ ) state and they are perturbing each other weakly through Fermi resonance. Since no transitions involving  $06^00$  ( $\Sigma$ ) state was found, the deperturbation process was not carried out and the transition wavenumbers of  $12^20 - 02^20$  and  $12^00 - 02^00$  transitions were deweighted in the fit. Eventually, the  $g_{22}$  value was determined to be  $3.513(55) \text{ cm}^{-1}$  for  $\text{H}^{11}\text{B}^{32}\text{S}$  and this value was also used for  $\text{H}^{10}\text{B}^{32}\text{S}$ . Strong correlations were found between  $g_{22}$  constant and the interaction terms. As a consequence, the  $g_{22}$  constant was fixed in the final fit and spectroscopic constants and rest of the interaction terms are determined. The fitted parameters are reported in Tables 4.4 and 4.9, for  $\text{H}^{11}\text{B}^{32}\text{S}$  and  $\text{H}^{10}\text{B}^{32}\text{S}$ , respectively.

In the millimeter wave study, Bizocchi and Esposti has recorded rotational lines up to  $J=18$  for  $02^00$  and  $02^20$  states. They reported that no obvious anomaly is detectable in the spectral patterns of these states, nevertheless a deperturbation analysis was still performed. Our infrared observation of  $\nu_2 = 2$  states contain rotational lines up to  $J=68$ . If the observed lines were fitted with the customary Eq. 4.1, the  $f$  parity lines fit fine but  $e$  parity lines did not fit. This provides strong evidence of  $l$ -type resonance which is essentially the interaction between  $e$  parity lines of  $02^00$  ( $\Sigma$ ) and  $e$  parity lines of  $02^20$  ( $\Delta$ ). Furthermore, no obvious Fermi resonance was found between  $\nu_3 = 1$  and  $\nu_2 = 2$  states and they were fitted separately in the present study.

#### 4.4.4 Observed $(v_1, v_2^l, v_3)$ states with $v_2 = 3$

For the vibrational states with  $v_2 = 3$ , the vibrational angular momentum quantum number  $l$  may assume the values  $\pm 1$  and  $\pm 3$ , thus giving rise to a doubly degenerated level  $\Pi$  and a doubly degenerate level  $\Phi$ . The lines for the  $v_2 = 3$  excited states are relatively weak and some of them are strongly blended. However, unlike the  $v_2 = 2$  states, no anomaly was observed in the spectral patterns for these states. Therefore, the full set of transition frequencies have been analyzed through customary eq. 4.1. Larger uncertainties were used for these lines due to their lower signal-to-noise ratio and blending. The fitted spectroscopic constants are provided in Tables 4.5 and 4.6.

Table 4.2: Spectroscopic constants (in  $\text{cm}^{-1}$ ) for  $\text{H}^{11}\text{B}^{32}\text{S}$  and the difference between the observed and ab initio calculated values (see text for details).

Level	$G_v - ZPE$		$B$		$D / 10^{-7}$		$H / 10^{-13}$
	Obs.	Obs.- Calc.	Obs.	Obs.- Calc.+ $\delta$	Obs.	Obs.- Calc.	Obs.
00 <sup>0</sup>	0.0	-	0.6365407082(27)	0.000038	7.294507(57)	0.06	2.189(30)
00 <sup>1</sup>	1172.369301(19)	-1.9	0.6331183265(32)	0.000006	7.327358(74)	0.07	2.804(35)
00 <sup>2</sup>	2335.134328(56)	-3.9	0.62968709(11)	-0.000035	7.35683(57)	0.06	3.265(87)
00 <sup>3</sup>	3488.34660(10)	-5.9	0.62624674(22)	-0.000087	7.3829(12)	0.06	3.47(18)
00 <sup>4</sup>	4632.04936(21)	-	0.62279385(30)	-	7.38466(88)	-	-
10 <sup>0</sup>	2735.80671(13)	-1.3	0.63356902(22)	0.000018	7.22540(81)	0.07	2.320(85)
20 <sup>0</sup>	5386.81387(48)	-2.9	0.63050863(53)	-0.000006	7.1377(11)	0.04	-
10 <sup>1</sup>	3906.36888(29)	-3.2	0.63018929(52)	-0.000014	7.2729(22)	0.06	3.27(25)
10 <sup>2</sup>	5067.06948(79)	-	0.6267998(12)	-	7.2951(31)	-	-

Table 4.3 : Spectroscopic constants (in  $\text{cm}^{-1}$ ) for H11B32S and the difference between the observed and ab initio calculated values (see text for details).

Level	$G_v - G_{(01^1_0)}^b$		$B$		$D / 10^{-7}$		$H^c / 10^{-13}$	$q / 10^{-3}$		$q_D / 10^{-9}$	
	<i>Obs.</i>	Obs.- Calc.	Obs.	Obs.- Calc.+ $\delta^a$	Obs.	Obs.- Calc.	Obs.	Obs.	Obs.- Calc.	Obs.	Obs.- Calc.
01 <sup>1</sup> 0	0.0	-	0.6373255043(41)	0.000036	7.376585(90)	0.07	2.213(51)	1.5503101(77)	0.008	-6.967(15)	1.1
01 <sup>1</sup> 1	1168.022631(54)	-1.9	0.63397283(11)	0.000005	7.43339(52)	0.07	3.044(88)	1.571928(65)	0.007	-8.597(22)	1.5
01 <sup>1</sup> 2	2326.718509(82)	-4.0	0.63059878(18)	-0.000038	7.48305(90)	0.06	3.55(13)	1.58878(10)	0.006	-10.064(31)	1.8
01 <sup>1</sup> 3	3476.11025(15)	-6.0	0.62720121(23)	-0.000097	7.50637(70)	0.04		1.60161(24)	0.006	-11.582(86)	1.0
11 <sup>1</sup> 0	2721.81800(19)	-1.5	0.63440885(32)	0.000016	7.3238(13)	0.05	3.24(15)	1.57806(18)	0.007	-7.838(43)	0.0
21 <sup>1</sup> 0	5358.78551(46)	-3.3	0.63140462(67)	-0.000005	7.2468(18)	0.05		1.61845(66)	0.007	-8.70(23)	0.1
11 <sup>1</sup> 1	3887.71672(35)	-3.5	0.63112287(43)	-0.000019	7.3800(11)	0.02		1.61626(49)	0.005	-10.42(15)	2.2

a)  $\delta = 0.0013 \text{ cm}^{-1}$

b) The value for  $G_{(01^1_0)}$  obtained from the variational calculation is  $706.5 \text{ cm}^{-1}$

Table 4.4: Spectroscopic constants (in  $\text{cm}^{-1}$ ) for  $\text{H}^{11}\text{B}^{32}\text{S}$  and the difference between the observed and ab initio calculated values (see text for details).

Level	$G_v - G_{02^0_0}$		$B$		$D / 10^{-7}$		$\eta / 10^{-2}$	$\eta_D / 10^{-9}$
	Obs.	Obs.-Calc.	Obs.	Obs.-Calc.	Obs.	Obs.-Calc.	Obs.	Obs.
02 <sup>0</sup> 0	0.0	-	0.638063598(11)	0.000033	7.43962(29)	-1.8		
02 <sup>2</sup> 0	14.0527(2594)	-1.7	0.6380362643(74)	0.000036	7.45019(16)	1.0	1.129352(66)	-5.43(13)
-----								
02 <sup>0</sup> 1	1163.16796(17)	-2.0	0.63479146(31)	0.000001	7.51873(91)	-1.7		
02 <sup>2</sup> 1	1177.79911(11)	-3.6	0.63475015(17)	0.000005	7.52412(46)	1.0	1.14401(30)	-6.56(16)
-----								
02 <sup>0</sup> 2	2317.35257(35)	-4.1	0.63148673(69)	-0.000040	7.5903(21)	-1.7		
02 <sup>2</sup> 2	2332.47803(23)	-5.8	0.63143146(38)	-0.000040	7.5889(11)	0.9	1.15645(65)	-7.83(23)
-----								
02 <sup>0</sup> 3	3462.52825(74)	-	0.6281543(21)	-	7.676(10)	-		
02 <sup>2</sup> 3	3478.08543(43)	-	0.62808315(95)	-	7.6541(37)	-	1.1678(26)	-1.01(14)
-----								
12 <sup>0</sup> 0	2708.76264(56)	-1.7	0.63518357(90)	0.000012	7.3963(23)	-2.0		
12 <sup>2</sup> 0	2721.53582(37)	-3.4	0.63517691(48)	0.000017	7.4033(10)	1.1	1.15180(70)	-6.25(22)

Table 4.5: Spectroscopic constants (in  $\text{cm}^{-1}$ ) for  $\text{H}^{11}\text{B}^{32}\text{S}$  and the difference between the observed and ab initio calculated values (see text for details).

Level	$G_v - G_{03^1_0}$		$B$		$D / 10^{-7}$		$q / 10^{-3}$		$q_D / 10^{-8}$	
	Obs.	Obs.- Calc.	Obs.	Obs.-Calc.	Obs.	Obs.- Calc.	Obs.	Obs.- Calc.	Obs.	Obs.- Calc.
03 <sup>1</sup> 0	0.0	-	0.6387249(19)	0.000024	8.1413(50)	0.02	3.1934(38)	0.07	-5.12(10)	-4.0
03 <sup>1</sup> 1	1158.41409(15)	-2.0	0.6355293(19)	-0.000008	8.2305(51)	0.02	3.2401(38)	0.06	-5.42(10)	-3.7
03 <sup>1</sup> 2	2308.16060(39)	-4.2	0.6322905(21)	-0.000049	8.3121(58)	0.00	3.2796(39)	0.06	-5.76(11)	-3.4
13 <sup>1</sup> 0	2695.27353(51)	-1.8	0.6358960(19)	0.000003	8.2080(49)	-0.05	3.2738(38)	0.07	-6.44(10)	-4.7

Table 4.6: Spectroscopic constants (in  $\text{cm}^{-1}$ ) for  $\text{H}^{11}\text{B}^{32}\text{S}$  and the difference between the observed and ab initio calculated values (see text for details).

Level	$G_v - G_{03^3_0}$		$B$		$D / 10^{-7}$		$q_H / 10^{-12}$
	Obs.	Obs.-Calc.	Obs.	Obs.-Calc.	Obs.	Obs.-Calc.	Obs.
03 <sup>3</sup> 0	0.0	-	0.6386677(18)	0.000039	6.8489(66)	0.08	-3.96(21)
03 <sup>3</sup> 1	1159.53593(12)	-2.0	0.6354497(19)	0.000011	6.9672(72)	0.09	-3.19(23)
03 <sup>3</sup> 2	2310.24813(20)	-4.1	0.6321877(19)	-0.000031	7.0683(71)	0.08	-2.80(22)
13 <sup>3</sup> 0	2692.80006(40)	-	0.6358747(20)	-	6.7510(78)	-	-4.33(24)

Table 4.7: Spectroscopic constants (in  $\text{cm}^{-1}$ ) for  $\text{H}^{10}\text{B}^{32}\text{S}$  and the difference between the observed and ab initio calculated values (see text for details).

Level	$G_v - ZPE$		$B$		$D / 10^{-7}$		$H / 10^{-13}$
	Obs.	Obs.- Calc.	Obs.	Obs.- Calc.	Obs.	Obs.- Calc.	Obs.
00 <sup>0</sup>	0.0	-	0.6698048616(41)	0.000043	8.01539(12)	0.07	1.87(15)
00 <sup>1</sup>	1207.067569(45)	-2.1	0.6661772927(49)	0.000030	8.07566(15)	0.08	3.47(16)
00 <sup>2</sup>	2403.97083(14)	-4.3	0.66253662(33)	-0.000033	8.1353(22)	0.05	5.64(42)
10 <sup>0</sup>	2751.44311(40)	-1.3	0.66641970(50)	0.000020	7.9225(14)	0.06	
10 <sup>1</sup>	3956.38287(59)	-3.4	0.66285801(88)	-0.000006	8.0003(28)	0.04	

Table 4.8: Spectroscopic constants (in  $\text{cm}^{-1}$ ) for  $\text{H}^{10}\text{B}^{32}\text{S}$  and the difference between the observed and ab initio calculated values (see text for details).

Level	$G_v - G_{01^1_0}$		$B$		$D / 10^{-7}$		$q / 10^{-3}$		$q_D / 10^{-9}$	
	Obs.	Obs.- Calc.	Obs.	Obs.- Calc.	Obs.	Obs.- Calc.	Obs.	Obs.- Calc.	Obs.	Obs.- Calc.
01 <sup>1</sup> 0	0.0	-	0.6707496667(28)	0.000041	8.113520(61)	0.09	1.6963672(57)	0.008	-8.137(12)	-1.8
01 <sup>1</sup> 1	1201.739000(82)	-2.1	0.66724330(15)	0.000026	8.20951(57)	0.08	1.74085(17)	0.007	-11.684(81)	-2.5
01 <sup>1</sup> 2	2393.72695(25)	-4.4	0.66370502(53)	-0.000036	8.2996(24)	0.03	1.77720(50)	0.005	-14.83(31)	-3.2
11 <sup>1</sup> 0	2737.2453(51)	-1.6	0.66743598(68)	0.000020	8.0499(17)	0.06	1.73462(80)	0.008	-9.67(26)	-2.0

Table 4.9: Spectroscopic constants (in  $\text{cm}^{-1}$ ) for  $\text{H}^{10}\text{B}^{32}\text{S}$  and the difference between the observed and ab initio calculated values (see text for details).

	$G_v - G_{02^0_0}$		$B$		$D / 10^{-7}$		$\eta / 10^{-3}$	$\eta_D / 10^{-9}$
	Obs.	Obs.- Calc.	Obs.	Obs.- Calc.	Obs.	Obs.- Calc.	Obs.	Obs.
02 <sup>00</sup>	0.0	-	0.671589766(20)	0.000040	8.17074(49)	-2.3	1.28406(17)	-5.33(45)
02 <sup>20</sup>	14.076(267)	-0.7	0.671614574(12)	0.000042	8.20520(31)	1.3		
02 <sup>01</sup>	1195.64523(74)	-2.1	0.6682130(22)	0.000020	8.304(11)	-2.3	1.3171(29)	-10.8(16)
02 <sup>21</sup>	1210.57060(39)	-2.8	0.6682259(11)	0.000029	8.3498(55)	1.2		

## 4.5 Conclusion

HBS was generated in a tube furnace at a temperature of 1300 °C. The infrared spectra of the unstable HBS molecule in the  $\nu_1$  and  $\nu_3$  fundamental regions have been recorded at high resolution using a Fourier transform spectrometer. Two fundamentals and 28 hot bands involving 33 vibrationally excited states located up to 6000  $\text{cm}^{-1}$  above the ground state were assigned for the main isotopologue,  $\text{H}^{11}\text{B}^{32}\text{S}$ . Similarly, for  $\text{H}^{10}\text{B}^{32}\text{S}$ , two fundamentals and 7 hot bands involving 12 vibrationally excited states located up to 4000  $\text{cm}^{-1}$  above the ground state were assigned. Spectroscopic constants were obtained for many vibrationally excited states of the two isotopologues for the first time. Taking into account the  $l$ -resonance effects in the  $\nu_2 = 2$  states, deperturbed spectroscopic constants have been obtained using the PGOPHER program. However, no obvious evidence for the Fermi resonance between  $\nu_3 = 1$  and  $\nu_2 = 2$  states was found as previously reported by Bizzocchi and Esposti<sup>73</sup>; thus they are fitted separately in the present study.

An ab initio potential energy surface was constructed using coupled cluster method [CCSD(T)-F12a] in conjunction with a triple-zeta quality basis set (cc-pVTZ-F12). Variational calculations were performed based on the calculated surface to predict spectroscopic constants. The fitted experimental constants were compared with predicted values from variational calculations. Good agreement has been found between the predicted and fitted experimental values.

# Chapter 5

## Direct fit of experimental ro-vibrational intensities to the dipole moment function: application to HCl

### 5.1 Introduction

The knowledge of accurate spectroscopic line parameters of hydrogen chloride (HCl) is important in modeling and interpreting spectra of stellar<sup>18</sup> and planetary<sup>19</sup> atmospheres. It is also required for the remote sensing of the Earth atmosphere<sup>20, 21</sup>, laser physics<sup>22, 23</sup> and precision measurements. Due to their importance, spectral parameters of HCl have been included in the HITRAN spectroscopic database<sup>24</sup> for three decades<sup>25</sup>. In the most recent HITRAN compilation<sup>24</sup> (with the exception of the pure rotational band) the line positions were calculated using the potential-energy surface of Coxon and Hajigeorgiou<sup>97</sup>, while the intensities were based on the dipole moment function (DMF) of Ogilvie et al.<sup>28</sup>, slightly modified to incorporate high-accuracy measurements of the fundamental band by Pine et al.<sup>98</sup>.

We have recently embarked on the task of updating and extending the existing HITRAN data for all hydrogen halides by improving existing line parameters and including more lines, bands and isotopologues<sup>26</sup>.

During the evaluation of the existing intensity data for HCl, we have found significant discrepancies between most commonly used semi-empirical dipole moment functions<sup>27-32</sup>. It is unfortunate that almost none of these DMFs have been used for intensity calculations that can be compared with experimental values. In the evaluation process, it was found that the use of the dipole moment function derived by Kiriya et al.<sup>32</sup> leads to severe discrepancies in line intensities (up to 40% even for low vibrational levels) when compared with the best available experimental data. Moreover, being considered as the most recent and extensive semi-empirical work, Ref.<sup>32</sup> was used to construct a piecewise dipole moment function at near-equilibrium internuclear distances by Buldakov and Cherepanov<sup>99</sup>. It was also used as an “experimental” function in order to evaluate recent theoretical calculations by Harrison<sup>100</sup> and in the calculation of the Einstein  $A$ -coefficients for vibrational transitions in the HCl laser<sup>101</sup>.

In 1955, Herman and Wallis derived a methodology to describe the influence of the vibration-rotation interaction on line intensities of rovibrational bands of diatomic molecules<sup>102</sup>. Subsequently, their approach was modified and widely used as a standard method of determining the rotationless dipole moment matrix element for the rovibrational bands by fitting the existing experimental data. These rotationless dipole moment matrix elements are employed in a second step to determine the power series (or Padé approximants) coefficients of the electronic dipole moment function<sup>27-29</sup>. However this method cannot be applied to a single line-intensity measurement since Herman-Wallis fitting is basically a polynomial fit of measurements of many lines within one rovibrational band.

There have been several new line-intensity measurements of HCl. Although these measurements are quite precise, they often only contain information for one or two lines of an entire vibrational band<sup>103, 104</sup>. In order to utilize the individual high-quality measurements for intensity

calculations, a direct fit approach was developed in this work. Furthermore, because the intensity measurements in the literature are often inconsistent, careful selection and appropriate weighting of the data were carried out. Ultimately, a new DMF for HCl was derived, fitted to the best available (and appropriately weighted) experimental data using this direct fit approach. The ro-vibrational line intensities derived from our function were compared with the ones based on previously reported DMF's, HITRAN, and experimental data.

## 5.2 Methodology and previous results

Traditionally the DMF of a diatomic molecule as a function of the internuclear distance,  $r$ , is given by the power series

$$\mu(r) = \sum_i M_i x^i, \quad (5.1)$$

where  $x = \frac{r-r_e}{r_e}$ ,  $r_e$  is the equilibrium separation and  $i = 0, 1, 2 \dots$ . Some of the previous works (Refs.<sup>28</sup> and Refs.<sup>31</sup> for instance) employed the accepted approach developed by Tipping and Herman<sup>105</sup> of using only pure vibrational matrix elements to determine the DMF. In order to obtain pure vibrational matrix elements, one can take available measurements and fit them separately for every band (in the case of HCl the measured bands used in this work have  $v = 0$  as a lower state) to the Herman-Wallis expression:

$$|\langle vJ' | \mu(x) | 0J'' \rangle|^2 = |R_{v0}(0)|^2 (1 + C_v m + D_v m^2 + \dots), \quad (5.2)$$

where  $R_{v0}(0)$  is a rotationless part,  $C_v$  and  $D_v$  are the Herman-Wallis coefficients, with  $m = -J$  for the P-branch and  $J + 1$  for the R-branch. In order to derive the  $M_i$  coefficients from Eq. (5.1), these obtained rotationless matrix elements  $R_{v0}(0)$  are then fit to:

$$R_{v0}(0) = \sum_i M_i \langle v | x^i | 0 \rangle, \quad (5.3)$$

where the expectation values  $\langle v|x^i|0\rangle$  can be determined from the potential energy function. In the case of the HCl molecule, bands with  $v'' = 0$  and  $v' = 0$  to 7 are available in the literature, and in Eq.(5.3)  $i$  is usually taken to run from 0 to 7. The double and single primes correspond to lower and upper state respectively.

In 2001, Kiriyaama et al.<sup>32</sup> had suggested that inclusion of rotational components into the fit can allow for a better determination of the  $M_i$  coefficients through fitting to a larger amount of points

$$|\langle vJ'|\mu(x)|0J''\rangle| = \sum_{i=1}^n M_i \langle vJ'|x^i|0J''\rangle \quad (5.4)$$

They had chosen experimental values from Pine et al.<sup>98</sup> for the fundamental band, Toth<sup>27</sup> for the first overtone, Ogilvie and Lee<sup>31</sup> for the second overtone, and Zughul<sup>106</sup> for bands 4 - 0 through 7 - 0. These experimental values were fitted (in Herman-Wallis-type manner) to Eq. (5.5) (reproduced exactly from Eq. (3.6) in the PhD thesis<sup>107</sup>) with the order of the polynomial being determined using the Gauss criterion<sup>32, 107</sup>:

$$\langle vJ'|\mu(x)|0J''\rangle = \sum_{i=1}^n c_i m^i. \quad (5.5)$$

Note that Eq. (5.5) is different from Eq. (5.2), where squares of transition dipole moments are fitted rather than the actual values. Although this probably does not have a dramatic impact, it is more physically correct to follow the traditional approach of fitting the squares, i.e. it is more correct to use Eq. (5.2).

The polynomials were then used to calculate ro-vibrational matrix elements, from which the  $M_i$  coefficients were determined using Eq. (5.4). The  $M_i$  coefficients determined in Ref.<sup>32</sup> are given in Table 5.1. Unfortunately, if one uses these coefficients to calculate ro-vibrational transition dipole moments, the results drastically differ from experimental values including those that were used as input in Ref.<sup>32</sup>. Moreover, if one compares the rotationless matrix elements from Ref.<sup>32</sup> with those determined in the original experimental works<sup>27, 31, 98, 108</sup> one can notice

significant differences even in these parameters, especially in the fundamental and first overtone bands. The source of the discrepancy becomes obvious if one takes the ratios of the squares of the Kiriyaama et al.<sup>32</sup> rotationless matrix elements to the ones determined in the original work of Pine et al.<sup>98</sup> and Toth et al.<sup>27</sup>. Both ratios are very close to 0.76 a value matching the isotopic abundance of H<sup>35</sup>Cl (0.757587), which mistakenly was not accounted for in the Kiriyaama et al.<sup>32</sup> analysis of the intensities directly measured in Refs.<sup>27, 98</sup>. In Refs.<sup>31, 108</sup> the reported experimental intensities are at 100% abundance (i.e. the actual experimental intensities were already divided by natural abundance), and therefore for the second through sixth overtones there is no error made by Kiriyaama et al.<sup>32</sup>.

In order to derive the new DMF, we identified the best available experimental results for each band and used the rotationless parameters derived in the original experimental work with proper weights. In general we used the Pine et al.<sup>98</sup> results for the fundamental band, Toth et al.<sup>27</sup> for the 2 - 0 band, Ogilvie and Lee<sup>31</sup> for the second overtone, and Zughul<sup>108</sup> for bands 4 - 0 through 7 - 0. We also added several individual ro-vibrational transition dipole moments that were measured with lower uncertainty (for instance the R(3) line in the first overtone measured by Ortwein et al.<sup>104</sup>). The rotationless value in the pure rotational band was taken as 1.10857 according to the recommendation of Ogilvie and Tipping<sup>109</sup>. We then used an overdetermined system of linear equations (Eq. (4)), that were solved using a weighted least squares method.

## 5.3 Details of the calculations and the results

To begin with, a potential energy function for  $\text{H}^{35}\text{Cl}$  was constructed using the purely numerical RKR method with the Dunham coefficients from Parekunnel et al.<sup>110</sup>. This RKR potential was then employed to calculate the transition wavenumbers, lower-state energies and the expectation values  $\langle vJ' | x^l | 0J'' \rangle$  using Le Roy's LEVEL program. Then the dipole moment matrix elements were evaluated from the measured line intensities. A sequence of signs of the dipole moment matrix elements (+ - + - - + -) was adopted as in the previous studies<sup>29, 31</sup>. Table 5.2 lists the dipole moment matrix elements derived in this study from the experimental intensities and their experimental uncertainties. A grand fit of all listed dipole moment matrix elements to the system of linear equations (Eq. (5.4), eighth order) was carried out using a weighted least squares fit program that was modified for the present study. Eight coefficients of dipole moment function,  $M_0, M_1, M_2, \dots, M_7$ , were subsequently determined and their values are listed in Table 5.1. For comparison, the coefficients of the dipole moment function coefficients determined by Ogilvie and Lee<sup>31</sup> and Kiriyama et al.<sup>32</sup> are included in Table 5.1. Finally, the three dipole moment functions listed in Table 5.1 are plotted against internuclear distance in Fig. 5.1. While the dipole moment function derived in this work does not differ drastically from the one derived in Ref.<sup>31</sup>, it clearly differs from the one derived in Ref.<sup>32</sup>. While the coefficients of  $M_i$  in Table 5.1 were derived using slightly different potentials and value of  $r_e$ , this cannot account for such a large difference. The reason for this discrepancy is an incorrect treatment of experimental intensities by Kiriyama et al.<sup>32</sup>. In the mean time we are confident in the quality of the RKR potential which is discussed in section 5.5.

It was found that adoption of the experimental uncertainties reported in the original publications (when available) did not offer the best fit to all the data. Thus adjustments were made (generally by increasing reported uncertainties) with the aim of reducing the overall deviation of the fitting. The uncertainties adopted for each line in our final fit are listed in Table 5.2.

The inner and outer classical turning points on the RKR potential for  $v = 7$  were found to be approximately 0.986 and 1.925 Å, which suggests that the present DMF is valid within this range.

By combining the wavefunctions and the dipole moment function, the Einstein A-coefficients were calculated for  $\Delta v = 0, 1, 2, 3, 4, 5, 6, 7$  up to  $v' = 7$ , and were converted to line intensities in HITRAN units. The corresponding file is given in the supplementary material. The file contains only the H<sup>35</sup>Cl lines, but the intensities for H<sup>37</sup>Cl, D<sup>35</sup>Cl and D<sup>37</sup>Cl isotopologues will be included in the global line list <sup>26</sup>. With the purpose of evaluating the influence of the DMF on reproducing line intensities, the line intensities calculated using LEVEL with the same wavefunctions but different DMFs were compared with experimental line intensities for the fundamental band and overtone bands up to  $v' = 7$ . HITRAN intensities were also included in the comparisons. The results of the comparisons are plotted in Figs. 5.2 to 5.7.

Table 5.1: Dipole moment function coefficients of HCl in units of debye. The number listed in parentheses is the standard error in the last digits of a given value.

	Present		
	study	Ogilvie and Lee <sup>31</sup>	Kiryama et al. <sup>32</sup>
$M_0$	1.093164(86)	1.093004(75)	1.095056(1)
$M_1$	1.23679(135)	1.23614(44)	1.076259(152)
$M_2$	0.01518(375)	0.02063(530)	-0.001429(155)
$M_3$	-1.5377(96)	-1.5318(131)	-1.252768(94)
$M_4$	-0.8729(342)	-0.9188(264)	-0.383620(52)
$M_5$	-0.4066(639)	-0.3519(425)	0.104152(100)
$M_6$	-0.7531(3011)	-0.4367(725)	-0.223482(1828)
$M_7$	1.9268(8062)	0.3513(2068)	2.024332(4263)

Table 5.2: Matrix elements  $M_{\nu 0}(m)$  of electric dipole moment of HCl in units of Debye. The subscripts  $\nu$  and 0 of  $M_{\nu 0}(m)$  represent the  $\nu$ th upper vibrational level and the ground vibrational level, respectively. Pine et al.<sup>98</sup> results were used for the fundamental band, Toth et al.<sup>27</sup> for the 2-0 band, Ogilvie and Lee<sup>31</sup> for the second overtone, and Zughul<sup>106</sup> for bands 4-0 through 7-0.

$m$	$M_{10}(m)$ $\times 10^2$		$M_{20}(m)$ $\times 10^3$		$M_{30}(m)$ $\times 10^4$		$M_{40}(m)$ $\times 10^5$		$M_{50}(m)$ $\times 10^6$		$M_{60}(m)$ $\times 10^6$		$M_{70}(m)$ $\times 10^6$	
-10	8.25672	2%												
-9	8.16347	2%												
-8	8.05362	2%	-8.46115	15%										
-7	7.96856	2%	-8.32351	15%	5.75723	25%	-2.88234	10%	-8.08881	20%	5.90593	25%		
-6	7.88346	2%	-8.25410	15%			-2.86567	10%	-7.99619	20%	5.96547	25%	-2.80935	30%
-5	7.77839	2%			5.74559	25%	-2.85896	10%	-7.95635	20%	6.03207	25%	-2.89648	30%
-4	7.67912	2%	-8.03939	15%	5.62528	25%	-2.87052	10%	-7.97178	20%	6.11274	25%	-3.01341	30%
-4			-8.07161 <sup>b)</sup>	4%										
-3	7.58356	2%			5.62737	25%	-2.90552	10%	-8.05581	20%	6.23252	25%	-3.24595	30%
-3					5.52761 <sup>c)</sup>	8%								
-2	7.48244	2%	-8.19298	15%	5.55171	25%	-2.96318	10%	-8.20179	20%	6.39073	25%	-3.07238	30%
-1	7.38562	2%	-8.09780	15%	5.69102	25%	-3.05364	10%	-8.42494	20%	6.60576	25%	-3.15826	30%

Table 5.2 continued.

1	7.19426	2%	-7.88354	15%	5.53129	25%	-3.15801	10%	-8.64716	20%	6.84937	25%	-3.28765	30%
2	7.10403	2%			5.67157	25%	-3.16065	10%	-8.62136	20%	6.86504	25%	-3.39395	30%
3	7.02272	2%			5.89590	25%	-3.19973	10%	-8.62304	20%	6.92039	25%	-3.49778	30%
4	6.94008	2%	-7.99267 <sup>a)</sup>	1%	5.68341	25%	-3.23565	10%	-8.68729	20%	7.00533	25%		
			-8.01496 <sup>b)</sup>	4%										
5	6.84209	2%	-7.75373	15%	6.24240	25%	-3.28203	10%	-8.74468	20%	7.11035	25%		
6	6.76418	2%	-7.98751	15%	6.37095	25%	-3.34624	10%	-8.82735	20%	7.23259	25%	-3.62641	30%
7	6.66449	2%	-7.73836	15%			-3.41058	10%	-8.91616	20%	7.36529	25%	-3.76753	30%
8	6.56930	2%	-7.92135	15%	6.13255	25%	-3.47490	10%	-8.99751	20%	7.50939	25%	-3.80380	30%
9	6.45739	2%	-7.72395	15%	6.40364	25%	-3.53754	10%	-9.10332	20%	7.65756	25%	-3.80741	30%
10	6.39033	2%	-7.95144	15%			-3.60597	10%	-9.21302	20%	7.78105	25%		
11	6.29444	2%												

<sup>a)</sup>Value calculated from line intensity reported by Ortwein et al.<sup>104</sup>, <sup>b)</sup>value calculated from line intensity reported by De Rosa et al.<sup>103</sup>, <sup>c)</sup>value calculated from line intensity reported by Stanton et al.<sup>111</sup>

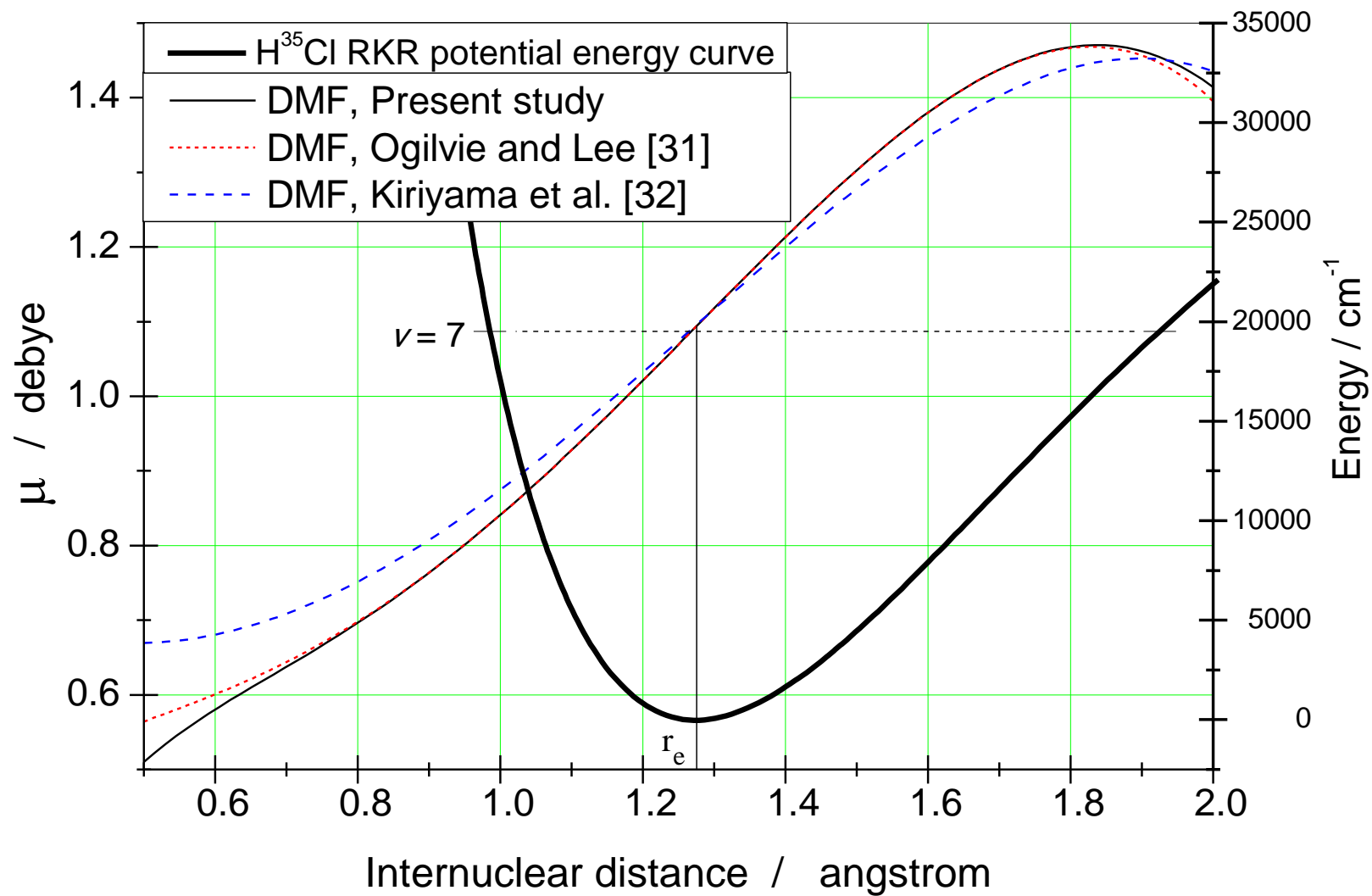


Figure 5.1: Dipole moment functions of HCl using the  $M_i$  coefficients from Table 5.1.

### 5.3.1 Line intensity of the fundamental band

In Fig. 5.2, all the calculated line intensities for the fundamental band of  $\text{H}^{35}\text{Cl}$ , including HITRAN, are compared with measurements of Pine et al.<sup>98</sup> and the percentage differences were plotted against  $m$ -values. The results clearly show that the line intensities calculated in present study, Ref.<sup>31</sup>, and HITRAN, are all within the 1% experimental error limit claimed by Pine et al.<sup>98</sup>. Furthermore, all three calculations agree well with each other in a unique pattern.

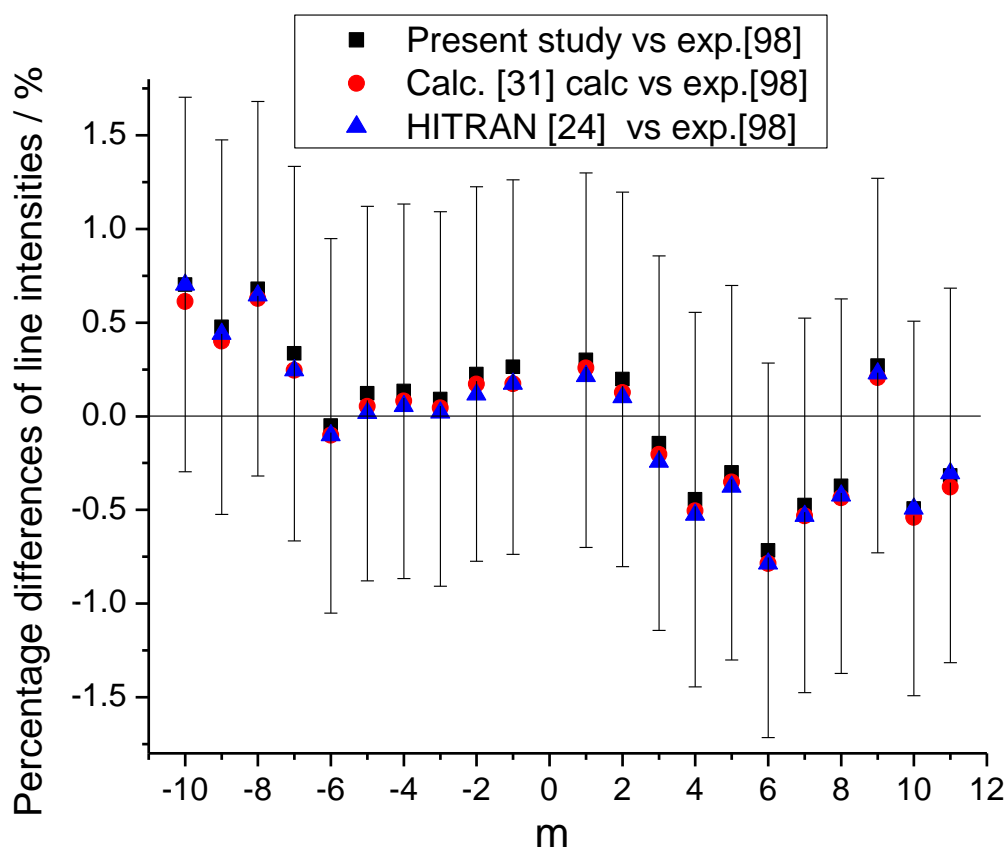


Figure 5.2: Comparison of the empirical line intensities with Pine et al. experimental values of the  $\text{H}^{35}\text{Cl}$  fundamental band.

### 5.3.2 Line intensity of the first overtone band

In Fig. 5.3, measurements by Toth et al.<sup>27</sup>, intensities derived from the DMF of Ogilvie and Lee<sup>31</sup>, and HITRAN intensities for the 2 - 0 band of

$\text{H}^{35}\text{Cl}$  were compared with the present study. Additionally, the latest high-precision measurements by Ortwein et al.<sup>104</sup> and De Rosa et al.<sup>103</sup> were also compared with present study. From Fig. 5.3, it is apparent that both our DMF and the DMF by Ogilvie and Lee<sup>31</sup> reproduced the line intensities of the 2 - 0 band very well. However, HITRAN line intensities appear to be underestimated by about 7%. The intensity of the R(3) line calculated from our DMF has shown slightly better agreement to the measurement by Ortwein et al.<sup>104</sup> ( $\sim 0.2\%$ ) than the intensity derived from the DMF by Ogilvie and Lee ( $\sim 1\%$ ). However the differences are insignificant and both are within experimental uncertainties.

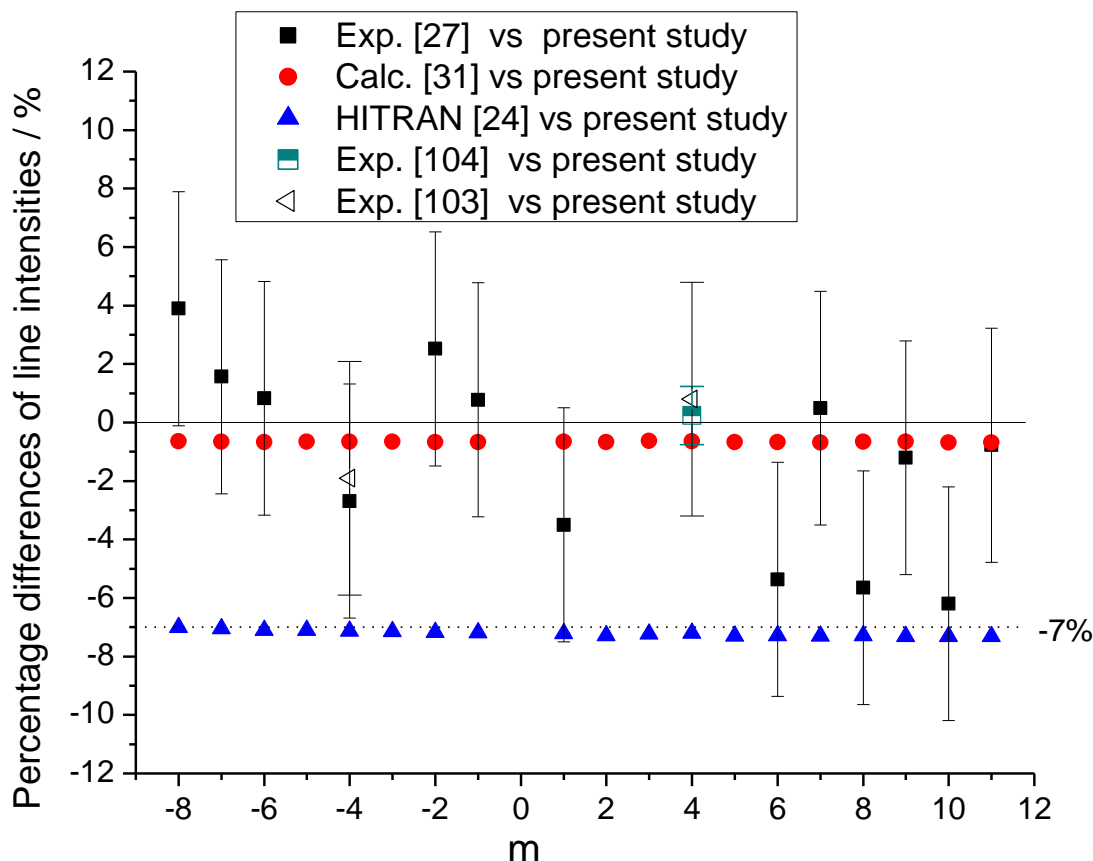


Figure 5.3: Comparison of the line-intensities of the  $\text{H}^{35}\text{Cl}$  2-0 band comparison with present study as a reference.

### 5.3.3 Line intensity of the second overtone band

A similar comparison was carried out for the 3 - 0 band. The HITRAN line intensities seem to be systematically underestimated by 17.5%. The reason for this is that in the semi-empirical DMF used for calculating HITRAN intensities, outdated low-resolution measurements by Benedict et al.<sup>112</sup> were used as an input. The values from Ref.<sup>112</sup> have shown large differences from more recent measurements by Ogilvie and Lee<sup>31</sup> and Stanton et al.<sup>111</sup> that were used as input parameters in this work. Interestingly, for the 3 - 0 band of  $\text{H}^{35}\text{Cl}$ , our calculation has shown better agreement with measurements by Ogilvie and Lee than the intensities derived from the semi-empirical DMF derived in the same work<sup>31</sup>.

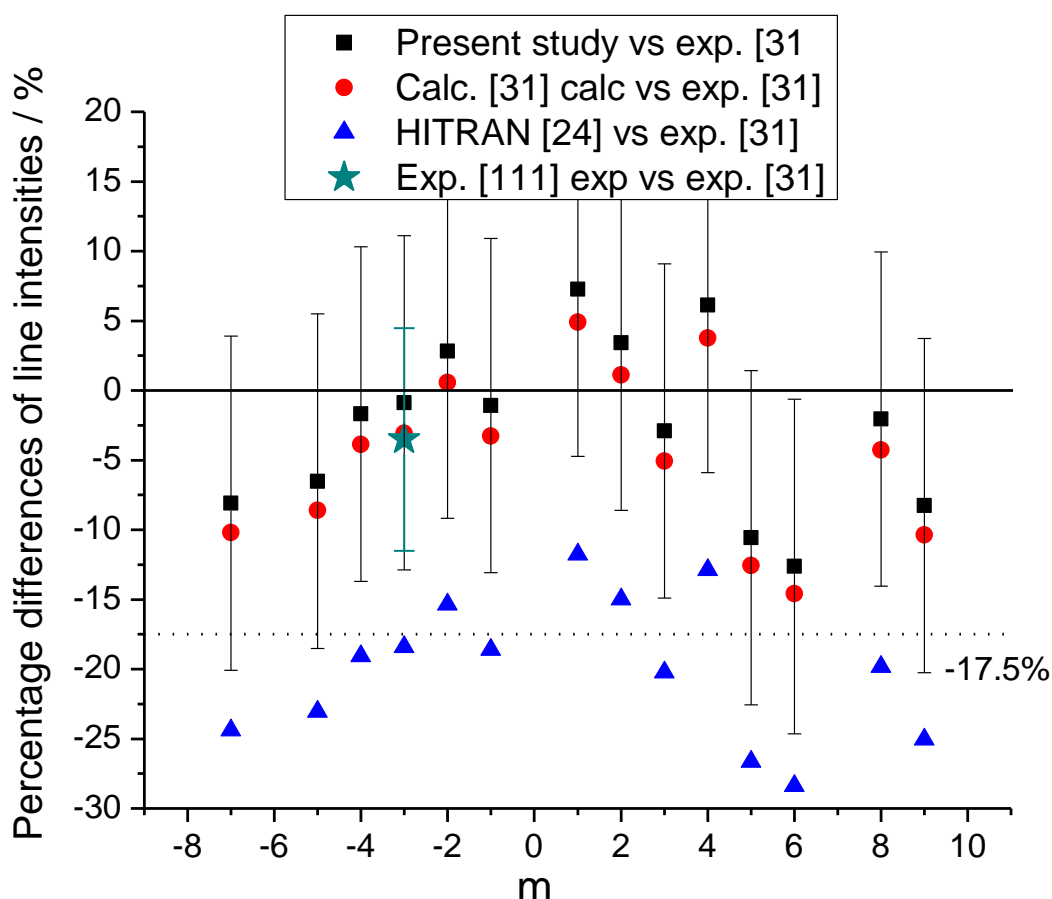


Figure 5.4: Comparison of the line-intensities of the  $\text{H}^{35}\text{Cl}$  3-0 band with experimental values [31] as a reference.

### 5.3.4 Line intensity of the 4 - 0, 5 - 0, 6 - 0 and 7 - 0 bands

Three papers have been published by Zughul et al. on the line intensity measurements of the 4 - 0 to 7 - 0 overtone bands of HCl<sup>106, 108, 113</sup> which report analysis of the same spectra recorded at Kitt Peak Observatory with a Fourier transform spectrometer (FTS). However, the reported line intensities are inconsistent in Ref.<sup>113</sup> and Ref.<sup>108</sup>. Although Ref.<sup>108</sup> and Ref.<sup>106</sup> have reported the same line intensities for the 4 - 0, 5 - 0 and 6 - 0 overtone bands, the published dipole moment matrix elements derived from these intensities are different. No explanations for these discrepancies are offered in any of the three papers<sup>106, 108, 113</sup>. The only other intensity measurements for the 5 - 0 and 6 - 0 overtone bands were carried out by Reddy using the photoacoustic method<sup>114</sup> with much larger reported uncertainty. The discrepancies between line intensities reported by Reddy<sup>114</sup> and Ref.<sup>108</sup> are about 10% to 25%. Taking into account the reported uncertainty of their measurements, the line intensities reported in Ref.<sup>108</sup> were adopted. A sequence of uncertainties, 10%, 20%, 25%, and 30% were employed for the 4 - 0, 5 - 0, 6 - 0 and 7 - 0 bands in our direct DMF fitting as relative weightings.

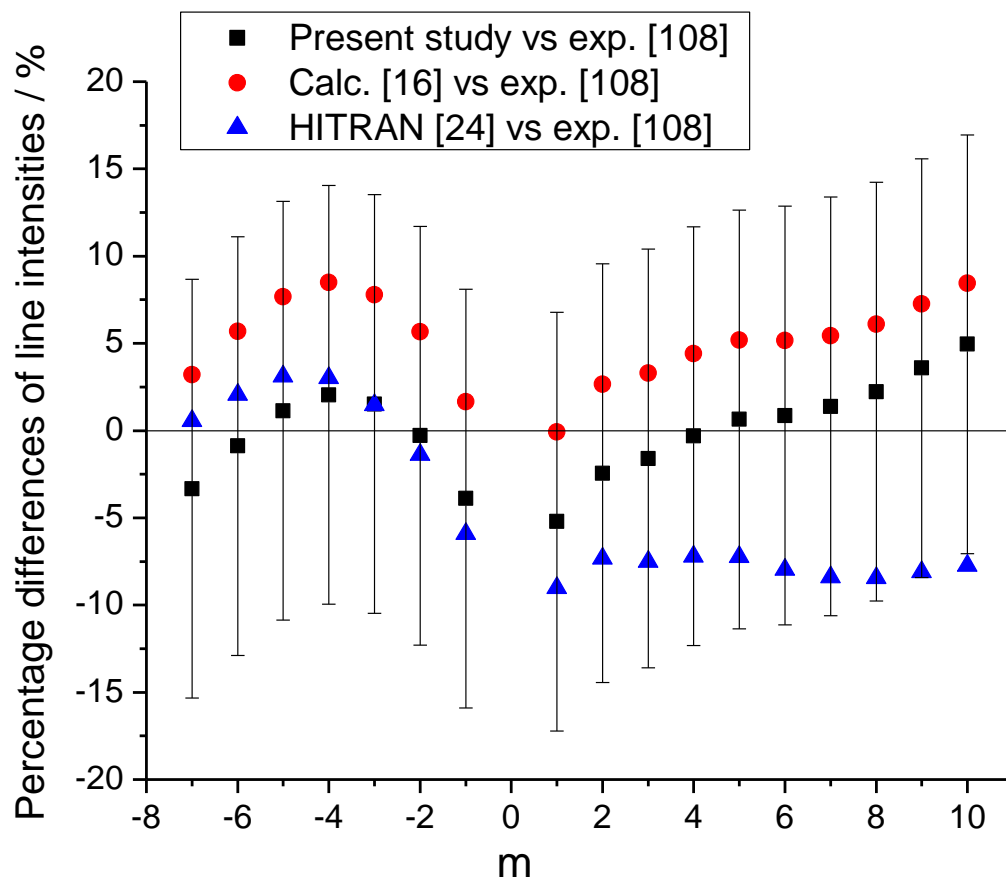


Figure 5.5: Comparison of the line-intensities of the  $\text{H}^{35}\text{Cl}$  4-0 band with experimental values [108] as a reference.

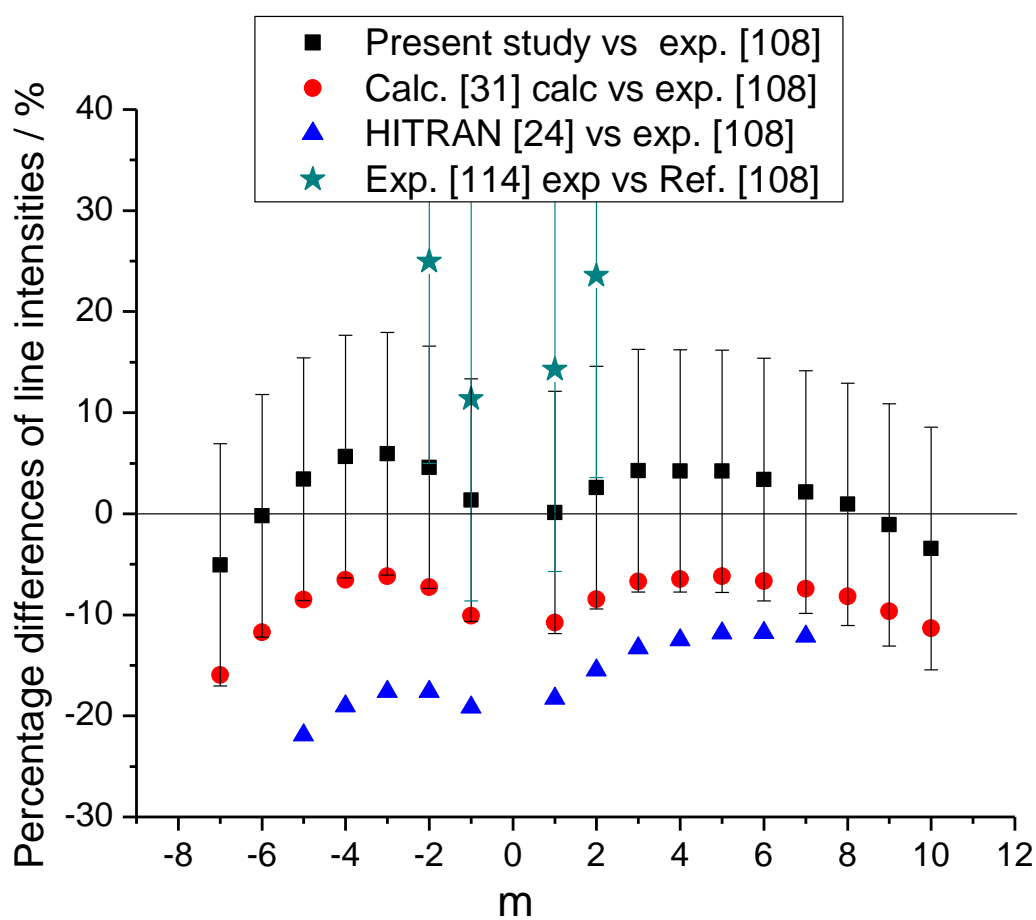


Figure 5.6: Comparison of the line-intensities of the  $\text{H}^{35}\text{Cl}$  5-0 band with experimental values [108] as a reference.

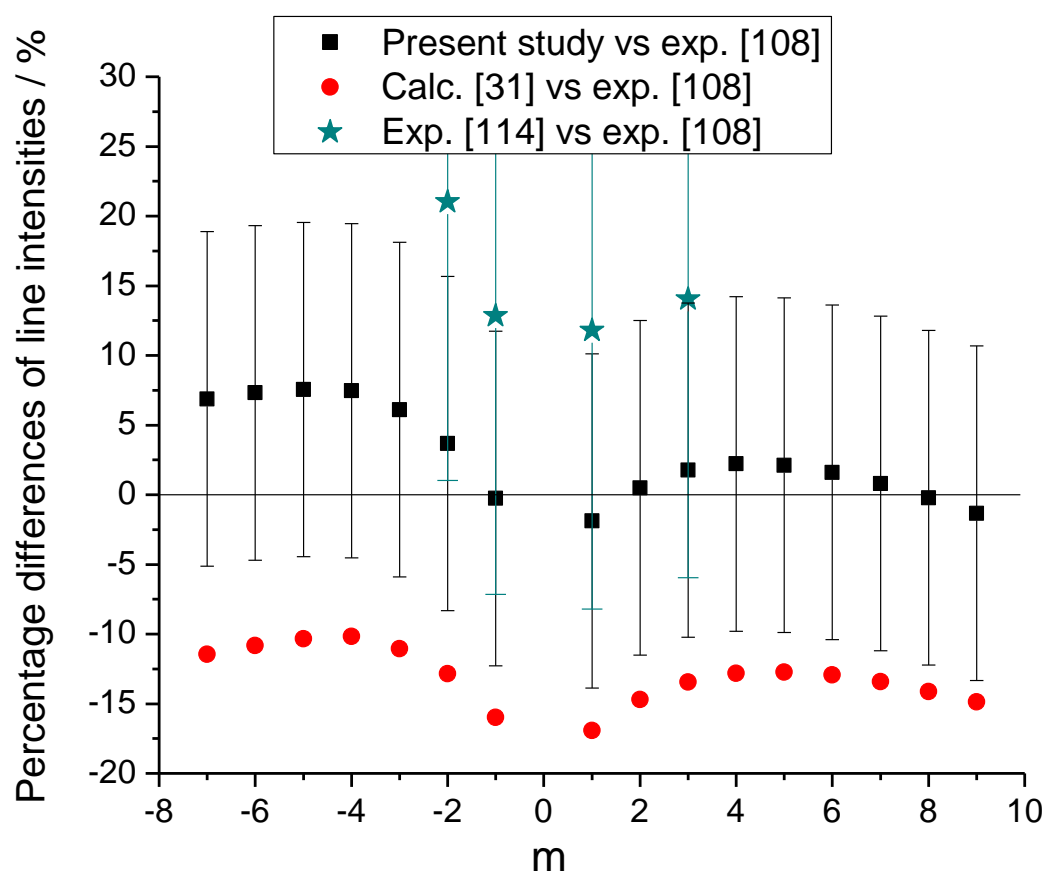


Figure 5.7: Comparison of the line-intensities of the  $\text{H}^{35}\text{Cl}$  6-0 band with experimental values [108] as a reference.

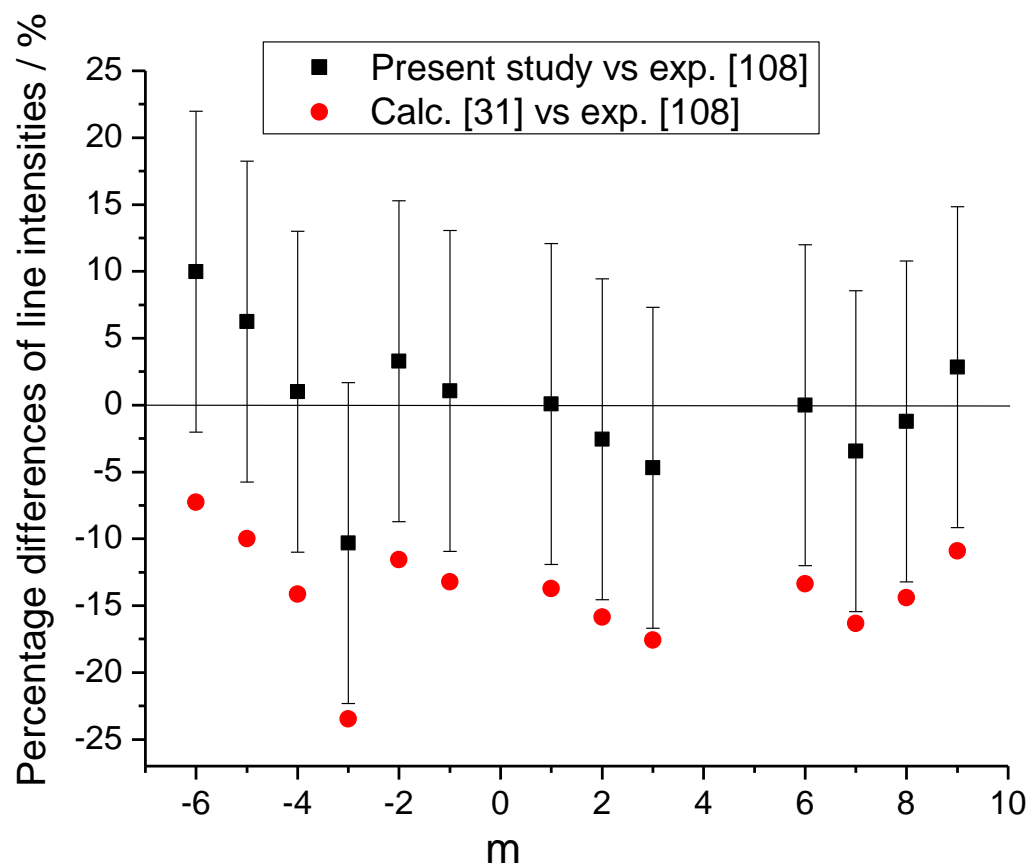


Figure 5.8: Comparison of the line-intensities of the  $\text{H}^{35}\text{Cl}$  7-0 band with experimental values [108] as a reference.

As shown in Fig. 5.5 to Fig. 5.8, line intensities calculated with the DMF derived here are in a better agreement with measurements from Ref.<sup>108</sup> for the 4 - 0 to 7 - 0 bands compared with both the intensities calculated from the DMF derived by Ogilvie and Lee<sup>31</sup> (that also used data from Ref.<sup>108</sup> as an input) and HITRAN intensities<sup>24</sup>. For the 5 - 0 and 6 - 0 bands, photoacoustic measurements by Reddy<sup>114</sup> were also included in the comparison and show a rather large discrepancy of +10% to +25%. Strangely, the difference between our calculations and intensity measurements from Ref.<sup>108</sup> show a quadratic dependence on the rotational quantum number. The source of this unusual behavior is unclear. Additional experiments in these high overtones are desirable in order to confirm the values reported in Ref.<sup>115</sup>.

## 5.4 Conclusion

The coefficients of a power series expansion of the dipole moment function of HCl valid for an internuclear range of 0.986 and 1.925 Å have been determined using a direct fit approach using the best available and appropriately weighted experimental data. Using wavefunctions derived from the Rydberg-Klein-Rees method and our DMF, line intensities were calculated numerically for  $\Delta v = 0, 1, 2, 3, 4, 5, 6, 7$  up to  $v' = 7$  bands using the LEVEL program. Calculation of the exact vibration-rotational matrix elements can involve complex algebra (see Refs.<sup>116, 117</sup>, for instance), but the use of LEVEL significantly simplifies the entire procedure. Comparisons were made between line intensities from the present study, the Ogilvie and Lee DMF<sup>31</sup>, HITRAN, and experimental measurements. The results have clearly shown that the DMF can be constructed directly from the experimental rovibrational dipole moment matrix elements, thereby avoiding Herman-Wallis fits of the individual bands and allowing inclusion of sparse data in the individual bands. Moreover, the inclusion of rotational dipole moment matrix elements gave a better prediction of line

intensities for the high- $J$  lines. Appropriate weighting of the data in the fit is important and can be easily implemented. We would like to emphasize that the inclusion of experimental uncertainties is crucial in the construction of semi-empirical models.

## 5.5 Future work

The methodology developed in this work will be applied to recalculate intensities of all hydrogen halides in the HITRAN database. In addition, intensities for the deuterated species, not presently available in HITRAN<sup>24</sup> will be produced<sup>26</sup>. Although the RKR potential used in this work seems to reproduce the experimental line positions quite accurately, it will be interesting to evaluate the effect on the result when using the exact experimental potential. We performed such an evaluation using an empirical potential provided to us by John Coxon and Photos Hajigeorgiou and adopted into LEVEL by Robert Le Roy. This potential is an improved version over the one these authors published previously in Ref.<sup>97</sup>.

Fig. 5.9 shows the comparison between transition dipole moments calculated using the RKR potential and the precise empirical potential to the experimental values. It is apparent from this figure that the difference is marginal. This fact has clearly demonstrated that, for the purpose of calculating line intensities, the RKR potential is sufficient as long as it is based on a accurate set of spectroscopic constants. Based on this fact, even supposing Ref.<sup>32</sup> had used a different potential from the current study, its influence on the intensity calculation is insignificant.

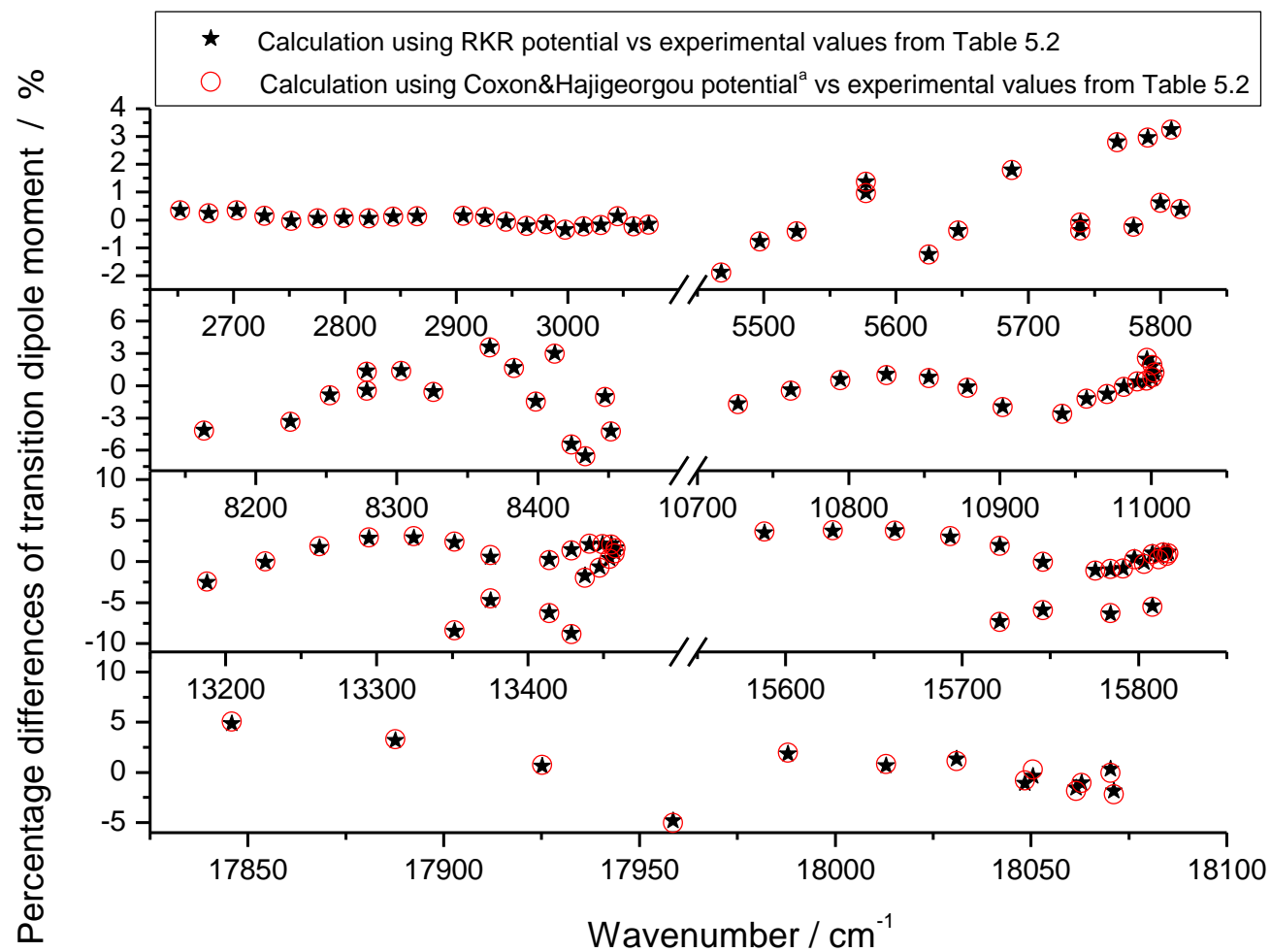


Figure 5.9: Transition dipole moment comparison with experimental values of 1-0, 2-0, 3-0, 4-0, 5-0, 6-0 and 7-0 bands of H<sup>35</sup>Cl. (a) Private communication with J. Coxon and P. Hajigeorgiou.

While the DMF in the polynomial form derived in this work is valid within the range of internuclear separations probed by experiments, a method of extrapolating the DMF will need to be developed. In particular, it is known that the fit of the data to Padé approximants rather than polynomials provides better predictions<sup>28</sup> beyond the range of experimental data. Alternatively, the theoretical calculations, such as those in Ref. <sup>100</sup> need to be evaluated, as they can be used outside the range of validity of semi-empirical DMFs. In general, the idea of implementing piecewise a semi-empirical DMF as proposed by Buldakov and Cherepanov<sup>99</sup> seems to be attractive. Unfortunately, when constructing their piecewise DMF, Buldakov and Cherepanov used the erroneous values of Kiriyaama et al.<sup>32</sup>, which undermined their results.

# Chapter 6

## Einstein A coefficients and absolute line intensities for the $E^2\Pi-X^2\Sigma^+$ transition of CaH

### 6.1 Introduction

CaH is an important molecule in astrophysics, having been identified in the spectra of sunspots<sup>33, 34</sup> and cool brown dwarfs<sup>35, 36</sup> through the observation of bands belonging to the  $A^2\Pi-X^2\Sigma^+$  and  $B^2\Sigma^+-X^2\Sigma^+$  transitions. The CaH bands are particularly strong in M dwarfs and are used to identify M<sup>37</sup> and L<sup>38, 39</sup> type subdwarfs in which metal hydrides are enhanced relative to metal oxides such as TiO. Subdwarfs are metal-poor objects and have very low abundances of heavy elements compared to normal stars like the Sun. The observation of metal hydrides and oxides is, therefore, used as a tool to monitor temperature and composition of the atmospheres of these objects.

As the number of new classes of stellar objects has grown<sup>40-42</sup>, the understanding of their atmospheres, evolution, and spectral characteristics remains far from complete. Considerable attempts have been made to develop models to determine their atmospheric parameters

such as chemical composition, pressure, surface gravity and temperature. Opacities for the molecular species found in the atmospheres of these objects are needed to achieve this goal. However, complete molecular opacity data for many species found in these atmospheres are still lacking, limiting the development of adequate atmospheric models for cool stars and brown dwarfs.

Among the hydride molecules, molecular opacities have been calculated for the  $A^6\Sigma^+-X^6\Sigma^+$  transition of CrH<sup>118</sup>, the  $F^4\Delta-X^4\Delta$  transition of FeH<sup>119</sup>, the  $A^4\Phi-X^4\Phi$  transition of TiH<sup>120</sup>, and the  $A^2\Pi-X^2\Sigma^+$  and  $B^2\Sigma^+-X^2\Sigma^+$  transitions of MgH<sup>121</sup>. In a more recent study, Hargreaves et al.<sup>2</sup> have created a line list at 2200 K for the near-infrared  $E^4\Pi-A^4\Pi$  and  $E^4\Pi-X^4\Delta$  transitions of FeH based on laboratory spectra and an ab initio calculation of the band strengths. For CaH, Weck et al.<sup>43</sup> have performed theoretical calculations on the rovibrationally-resolved transitions involving the  $A^2\Pi$ ,  $B^2\Sigma^+$ ,  $B'^2\Sigma^+$ , and  $E^2\Pi$  excited states and the  $X^2\Sigma^+$  ground states. Their results were in good agreement with the available theoretical and experimental data for the vibrational energy levels and band oscillator strengths. Since the  $A^2\Pi$  and  $B^2\Sigma^+$  states of CaH are affected by strong interactions between the two states and some other close-lying electronic states, a qualitative fit of the observed transitions is still lacking. A deperturbation analysis of the two transitions is therefore necessary in order to obtain a complete set of spectroscopic constants, including the interaction parameters. Work in this direction is currently being undertaken and the results will enable the calculation of molecular opacities for the  $A^2\Pi-X^2\Sigma^+$  and  $B^2\Sigma^+-X^2\Sigma^+$  transitions of CaH using high-resolution experimental data.

Recently we have completed a high resolution analysis of the  $E^2\Pi-X^2\Sigma^+$  transition of CaH<sup>44</sup> observed in the 20100-20700  $\text{cm}^{-1}$  spectral region. The spectra were recorded using a Bruker IFS 120 HR Fourier transform spectrometer, and a rotational analysis of the 0-0 and 1-1 bands was carried out in order to obtain an improved set of spectroscopic parameters

for the  $E^2\Pi$  and  $X^2\Sigma^+$  states<sup>44</sup>. These results, combined with the transition dipole moment function of the  $E^2\Pi$ - $X^2\Sigma^+$  transition determined by Weck et al.<sup>43</sup>, have enabled the calculation of Einstein A coefficients and absolute line intensities using the computer programs LEVEL<sup>122</sup> and PGOPHER (version 7.1.108.13)<sup>46</sup>. Line lists and Einstein A coefficients for different bands of the  $E^2\Pi$ - $X^2\Sigma^+$  transition have been generated. A summary of the theoretical approach applied, and the results of our calculations will be presented.

## 6.2 Methodology

The knowledge of absolute line intensities and Einstein A coefficients of molecular species is of fundamental importance with applications in areas such as astrophysics and atmospheric science<sup>7</sup>. While Einstein A coefficients can be obtained indirectly by measurements of radiative lifetimes, experimental measurements of absolute line intensities require specific experimental conditions which are difficult to obtain for many high temperature molecular species. The rapid increase in computing power and the recent developments in quantum chemistry have made it possible to compute these data, in addition to making experimental measurements. The use of semi-empirical methods that combine the best available experimental and theoretical data can provide the desired information for important molecular species.

Theoretically, the eigenvalues  $E_{v,J}$  and eigenfunctions  $\psi_{v,J}(r)$  for a diatomic molecule with the potential  $V_J(r)$  can be determined by solving the one-dimensional Schrödinger equation. Methods for determining the potential  $V_J(r)$  include the RKR (Rydberg-Klein-Rees) method, or ab initio calculations. Line intensities for an electronic transition of a diatomic molecule are proportional to the square of the appropriate transition dipole moment matrix element,  $\langle \psi_{v',J'}(r) | \mathcal{R}_e(r) | \psi_{v'',J''}(r) \rangle$ , where  $\mathcal{R}_e(r)$  is

the electronic transition dipole moment. Given the electronic wavefunction,  $\psi_{el}(r)$ , as a function of internuclear distance,  $\mathcal{R}_e(r)$  can be calculated *ab initio*,

$$\mathcal{R}_e(r) = \langle \psi'_{el}(r) | \boldsymbol{\mu}(r) | \psi''_{el}(r) \rangle \quad \text{Eq. 6. 1}$$

where  $\boldsymbol{\mu}(r)$  is the electric dipole moment operator.

The calculation of transition dipole moment matrix elements of the form  $\langle \psi_{v',j'}(r) | \mathcal{R}_e(r) | \psi_{v'',j''}(r) \rangle$  is rather involved. However, we have shown in a previous study on HCl<sup>123</sup> that Le Roy's LEVEL program can significantly simplify this procedure and produce transition dipole moment matrix elements with sufficient accuracy for many purposes. Once transition dipole moment matrix elements are extracted from LEVEL, Einstein A coefficients can be calculated with the aid of the PGOPHER program<sup>46</sup> by the relation<sup>48</sup>:

$$A_{j' \rightarrow j''} = 3.13618932 \times 10^{-7} \nu^3 \frac{\theta}{2j'+1} \left| \langle \psi_{v',j'} | \mathcal{R}_e(r) | \psi_{v'',j''} \rangle \right|^2 \quad \text{Eq. 6. 2}$$

where  $A_{j' \rightarrow j''}$  has the units of  $\text{s}^{-1}$ ,  $\nu$  is the transition wavenumber ( $\text{cm}^{-1}$ ),  $\theta$  is the rotational line strength factor (Hönl-London factor) which will be discussed in detail later, and  $\mathcal{R}_e$  is the electronic transition dipole moment in debye.

### 6.2.1 Hönl-London Factors

In general, the line strength,  $\mathcal{S}$ , for the one-photon electric-dipole-allowed  $aJ' - bJ''$  transition of a diatomic molecule is given by the integral<sup>48</sup>:

$$S_{aJ',bJ''} = \sum_{p,M',M''} |\langle \Psi_{aJ'M'} | T_p^1(\mu) | \Psi_{bJ''M''} \rangle|^2 \quad \text{Eq. 6. 3}$$

where  $\Psi_{aJ'M'}$  and  $\Psi_{bJ''M''}$  are the wavefunctions for the magnetic substates of the upper and lower states, respectively,  $J'$  and  $J''$  the total angular momenta,  $M'$  and  $M''$  their associated components (in a space-fixed coordinate system),  $a$  and  $b$  any other necessary quantum numbers, and  $T_p^1(\mu)$  are the spherical tensor components (in a space-fixed coordinate system) of the transition dipole moment operator.

In order to derive expressions for the line strength,  $T_p^1(\mu)$  must be expressed in terms of the molecule-fixed components  $T_q^1$  using Wigner  $\mathfrak{D}$  matrices<sup>124</sup>.

$$T_p^1(\mu) = \sum_q \mathfrak{D}_{pq}^1(\omega)^* T_q^1(\mu) \quad \text{Eq. 6. 4}$$

Using case (a) basis functions of the form  $|\eta\Lambda; v; S\Sigma; J\Omega M\rangle$  (i.e., a non-parity basis set; refer to Ref.<sup>124</sup> for definitions of the quantum numbers), assuming the radiation is isotropic, and using the Wigner-Eckart theorem,  $S^{basis}$  can be written as<sup>124</sup>:

$$\begin{aligned}
& S_{\eta'\Lambda'v'S'\Sigma'J'\Omega',\eta''\Lambda''v''S''\Sigma''J''\Omega''}^{basis} \\
&= 3 \sum_{M',M''} |\langle \eta'\Lambda'; v'; S'\Sigma'; J'\Omega'M' | T_{p=0}^1(\mu) | \eta''\Lambda''; v''; S''\Sigma''; J''\Omega''M'' \rangle|^2 \\
&= 3 \sum_{M',M''} \left| \sum_q \langle \eta'\Lambda'; v'; S'\Sigma'; J'\Omega'M' | \mathcal{D}_{0q}^1(\omega)^* T_q^1(\mu) | \eta''\Lambda''; v''; S''\Sigma''; J''\Omega''M'' \rangle \right|^2 \\
&= 3 \sum_{M',M''} \left| \sum_q \langle \eta'\Lambda^{s'} | T_q^1(\mu) | \eta''\Lambda^{s''} \rangle \langle S'\Sigma' | S''\Sigma'' \rangle \langle v' | v'' \rangle \langle J'\Omega'M' | \mathcal{D}_{0q}^1(\omega)^* | J''\Omega''M'' \rangle \right|^2 \\
&= 3 \delta_{S'S''} \delta_{\Sigma'\Sigma''} q_{v'v''} \\
&\quad \sum_{M',M''} \left| \sum_q (-1)^{J'-M'} \begin{pmatrix} J' & 1 & J'' \\ -M' & 0 & M'' \end{pmatrix} \langle J'\Omega' | \mathcal{D}_{-q}^1(\omega)^* | J''\Omega'' \rangle \langle \eta'\Lambda^{s'} | T_q^1(\mu) | \eta''\Lambda^{s''} \rangle \right|^2 \\
&= \delta_{S'S''} \delta_{\Sigma'\Sigma''} q_{v'v''} \\
&\quad \left| \sum_q (-1)^{J'-\Omega'} \begin{pmatrix} J' & 1 & J'' \\ -\Omega' & q & \Omega'' \end{pmatrix} \sqrt{(2J'+1)(2J''+1)} \langle \eta'\Lambda^{s'} | T_q^1(\mu) | \eta''\Lambda^{s''} \rangle \right|^2 \\
&= \delta_{S'S''} \delta_{\Sigma'\Sigma''} q_{v'v''} |\mathcal{R}_e|^2 \Theta_{J'\Omega',J''\Omega''} \tag{Eq. 6.5}
\end{aligned}$$

where  $|\mathcal{R}_e|^2 = |\langle \eta'\Lambda^{s'} | T_{\Lambda'-\Lambda''}^1(\mu) | \eta''\Lambda^{s''} \rangle|^2$

and  $\Theta_{J'\Omega',J''\Omega''} = (2J'+1)(2J''+1) \begin{pmatrix} J' & 1 & J'' \\ -\Omega' & \Omega' - \Omega'' & \Omega'' \end{pmatrix}^2$ .

In this definition,  $q_{v'v''}$  is the Franck-Condon factor,  $\mathcal{R}_e$  the electronic transition dipole moment of the molecule, and  $\Theta_{J'\Omega',J''\Omega''}$  the (non-parity) Hönl-London factors (HLFs). The derivation of Eq. 6.5 makes use of the Franck-Condon principle.

The HLFs for singlet-singlet transitions were originally derived by Hönl and London in 1925<sup>125</sup>. Analytical formulae of HLFs for higher

multiplicity transitions have subsequently been derived during the last century<sup>126-135</sup>. Generally published formulae agree with respect to the relative intensities within a band, however there are often discrepancies by a factor of two or more for the absolute intensities for certain types of transitions. Some of the ambiguities regarding HLFs in the literature were summarized by Hansson and Watson<sup>135</sup> in 2005 for singlet-singlet transitions. Their derivation also showed that the use of parity basis functions introduces an additional factor of two in absolute intensities for the perpendicular transitions  ${}^1\Pi\text{-}{}^1\Sigma$  and  ${}^1\Sigma\text{-}{}^1\Pi$ . For all other singlet-singlet transitions, the use of parity basis functions, as in Eq. 6.6, produces the same expressions for HLFs due to the symmetry relations between the matrix elements.

$$|\eta^{2S+1}\Lambda|_{\Omega} v J M \text{ par} = \pm 1\rangle = \frac{1}{\sqrt{2}} \{ |\eta\Lambda^s; v; S\Sigma; J\Omega M\rangle \pm (-1)^{J-S+s} |\eta-\Lambda^s; v; S - \Sigma; J-\Omega M\rangle \} \quad \text{Eq. 6. 6}$$

Hansson and Watson's conclusions for perpendicular  ${}^1\Pi\text{-}{}^1\Sigma$  and  ${}^1\Sigma\text{-}{}^1\Pi$  transitions can be extended to higher multiplicity even-electron  $\Pi\text{-}\Sigma$  and  $\Sigma\text{-}\Pi$  transitions. In such cases, the associated basis function for the  $\Sigma = 0$  component of a  $\Sigma$  state is no longer written as a linear combination, but as a single function of the form

$$|\eta^{2S+1}\Sigma_0^{(s)} v J M \text{ par} = J - S + s\rangle = |\eta\Lambda = 0^{(s)}; v; S\Sigma = 0; J\Omega = 0M\rangle \quad \text{Eq. 6. 7}$$

(For odd-electron systems, all wavefunctions are of the form given in Eq. 6.6) It is obvious that any  $\Pi\text{-}\Sigma$  /  $\Sigma\text{-}\Pi$  matrix elements involving the basis function in Eq. 6.7 must be a factor of two higher than the corresponding matrix element derived in a non-parity basis set. General expressions for HLFs in a case (a) parity basis set ( $\theta_{J'\Omega' \text{ par}', J''\Omega'' \text{ par}''}$ ) are given in Table 6.1. Note that for the purposes of this table we define  $\Lambda \geq 0$ . Furthermore,

values of  $\Omega$  must satisfy the requirement  $\Delta\Sigma=0$ . The entries in Table 6.1 of Hansson and Watson<sup>135</sup> can be viewed as a special case of those in the present Table 6.1, with  $\Omega = \Lambda$  ( $\Sigma=0$  for singlet states).

Table 6.1:  $\theta_{J'\Omega'par',J''\Omega''par''}$

Transition	P	Q	R
$\Delta\Lambda = 0$	$\frac{(J'' - \Omega'')(J'' + \Omega'')}{J''}$	$\frac{(2J'' + 1)\Omega''^2}{J''(J'' + 1)}$	$\frac{(J'' + 1 - \Omega'')(J'' + 1 + \Omega'')}{J'' + 1}$
$\Delta\Lambda = -1$	$w' \frac{(J'' - 1 + \Omega'')(J'' + \Omega'')}{2J''}$	$w' \frac{(2J'' + 1)(J'' + \Omega'')(J'' + 1 - \Omega'')}{2J''(J'' + 1)}$	$w' \frac{(J'' + 1 - \Omega'')(J'' + 2 - \Omega'')}{2(J'' + 1)}$
$\Delta\Lambda = +1$	$w'' \frac{(J'' - 1 - \Omega'')(J'' - \Omega'')}{2J''}$	$w'' \frac{(2J'' + 1)(J'' - \Omega'')(J'' + 1 + \Omega'')}{2J''(J'' + 1)}$	$w'' \frac{(J'' + 1 + \Omega'')(J'' + 2 + \Omega'')}{2(J'' + 1)}$

where  $w' = 1 + \delta_{\Lambda'0}\delta_{\Sigma'0}$  and  $w'' = 1 + \delta_{\Lambda''0}\delta_{\Sigma''0}$ .

Note that the total line strength calculated in a basis set with defined parity,  $S_{\eta'\Lambda'v'S'\Sigma'J'\Omega'par',\eta''\Lambda''v''S''\Sigma''J''\Omega''par''}^{basis}$ , will differ from Eq. 6.5 when  $w'$  or  $w''$  equals 2. The (parity) HLFs,  $\theta_{J'\Omega'par',J''\Omega''par''}$ , in Table 6.1 reduce to the (non-parity) HLFs,  $\theta_{J'\Omega',J''\Omega''}$ , by setting  $w' = w'' = 1$ . Furthermore, it can be shown that the normal “sum rule”<sup>133-135</sup> for HLFs still applies, where the sum is taken over all possible spin-components and  $\Lambda$ -doublets,

$$\sum \theta_{J'\Omega',J''\Omega''} = \sum \theta_{J'\Omega'par',J''\Omega''par''} = (2 - \delta_{\Lambda'0}\delta_{\Lambda''0})(2S + 1)(2J + 1)$$

Eq. 6. 8

## 6.2.2 Calculation of Hönl-London Factors for a ${}^2\Pi$ - ${}^2\Sigma^+$ Transition

As we have seen, obtaining analytical formulae for HLFs using Hund’s case-(a) basis functions is rather straightforward. However, applying these to real molecules requires more work. The Hamiltonian matrices of the lower and upper states need to be diagonalised to produce wavefunctions which are simply linear combinations of the basis functions. The line strength for a particular rovibronic line can then be computed by transforming the basis-calculated transition dipole moment matrix elements using the coefficients from the diagonalisation, and squaring the result.

For the purpose of validation, we have re-derived analytical HLFs for a  ${}^2\Pi$ - ${}^2\Sigma^+$  transition to compare with the output of PGOPHER; these were first derived by Earls in 1935<sup>128</sup>. Analytical expressions for the eigenstates of a  ${}^2\Pi$  state intermediate between Hund’s cases (a) and (b) are derived in the Appendix using a simple version of the  $N^2$  Hamiltonian<sup>124</sup>.  ${}^2\Sigma^+$  eigenstates can be found in various text books, e.g.<sup>48</sup>. General expressions for these HLFs are given in Table 6.2, with analytical expressions (upon

substitution of Wigner 3-j symbols, etc.) for 12 branches of a  ${}^2\Pi-{}^2\Sigma^+$  transitions listed in Table 6.3. The parity for each entry in Tables 6.2 and 6.3 is determined by that of the lower  ${}^2\Sigma^+$  state: for  $F_1$ , the parity of each  $J$ -level is equated with  $(-1)^{J-1/2}$ ; for  $F_2$ , with  $(-1)^{J+1/2}$ . Upper-state parities must satisfy the relationship  $par'par'' = -1$ .

Table 6.2: General HLF expressions for a  ${}^2\Pi\text{-}{}^2\Sigma^+$  transition in which the  ${}^2\Pi$  state is intermediate between Hund's cases (a) and (b). Refer to text for further details.

${}^2\Pi$ (upper)	${}^2\Sigma^+$ (lower)	$\Theta_{J'\Omega'par'J''\Omega''par''}^a$
F <sub>1</sub>	F <sub>1</sub>	$(2J' + 1)(2J'' + 1) \left\{ \beta_{J'}^2 \begin{pmatrix} J' & 1 & J'' \\ -\frac{3}{2} & 1 & \frac{1}{2} \end{pmatrix}^2 + \alpha_{J'}^2 \begin{pmatrix} J' & 1 & J'' \\ -\frac{1}{2} & 1 & -\frac{1}{2} \end{pmatrix}^2 - 2\alpha_{J'}^2\beta_{J'}^2 \begin{pmatrix} J' & 1 & J'' \\ -\frac{3}{2} & 1 & \frac{1}{2} \end{pmatrix} \begin{pmatrix} J' & 1 & J'' \\ -\frac{1}{2} & 1 & -\frac{1}{2} \end{pmatrix} \right\}$
F <sub>1</sub>	F <sub>2</sub>	$(2J' + 1)(2J'' + 1) \left\{ \beta_{J'}^2 \begin{pmatrix} J' & 1 & J'' \\ -\frac{3}{2} & 1 & \frac{1}{2} \end{pmatrix}^2 + \alpha_{J'}^2 \begin{pmatrix} J' & 1 & J'' \\ -\frac{1}{2} & 1 & -\frac{1}{2} \end{pmatrix}^2 + 2\alpha_{J'}^2\beta_{J'}^2 \begin{pmatrix} J' & 1 & J'' \\ -\frac{3}{2} & 1 & \frac{1}{2} \end{pmatrix} \begin{pmatrix} J' & 1 & J'' \\ -\frac{1}{2} & 1 & -\frac{1}{2} \end{pmatrix} \right\}$
F <sub>2</sub>	F <sub>1</sub>	$(2J' + 1)(2J'' + 1) \left\{ \alpha_{J'}^2 \begin{pmatrix} J' & 1 & J'' \\ -\frac{3}{2} & 1 & \frac{1}{2} \end{pmatrix}^2 + \beta_{J'}^2 \begin{pmatrix} J' & 1 & J'' \\ -\frac{1}{2} & 1 & -\frac{1}{2} \end{pmatrix}^2 + 2\alpha_{J'}^2\beta_{J'}^2 \begin{pmatrix} J' & 1 & J'' \\ -\frac{3}{2} & 1 & \frac{1}{2} \end{pmatrix} \begin{pmatrix} J' & 1 & J'' \\ -\frac{1}{2} & 1 & -\frac{1}{2} \end{pmatrix} \right\}$
F <sub>2</sub>	F <sub>2</sub>	$(2J' + 1)(2J'' + 1) \left\{ \alpha_{J'}^2 \begin{pmatrix} J' & 1 & J'' \\ -\frac{3}{2} & 1 & \frac{1}{2} \end{pmatrix}^2 + \beta_{J'}^2 \begin{pmatrix} J' & 1 & J'' \\ -\frac{1}{2} & 1 & -\frac{1}{2} \end{pmatrix}^2 - 2\alpha_{J'}^2\beta_{J'}^2 \begin{pmatrix} J' & 1 & J'' \\ -\frac{3}{2} & 1 & \frac{1}{2} \end{pmatrix} \begin{pmatrix} J' & 1 & J'' \\ -\frac{1}{2} & 1 & -\frac{1}{2} \end{pmatrix} \right\}$
F <sub>1</sub> ( $J'=0.5$ ) <sup>b</sup>	F <sub>1</sub> /F <sub>2</sub>	$2(2J'' + 1) \begin{pmatrix} \frac{1}{2} & 1 & J'' \\ -\frac{1}{2} & 1 & -\frac{1}{2} \end{pmatrix}^2$

$$^a \alpha_J = \left[ \frac{X_J + (Y-2)}{2X_J} \right]^{\frac{1}{2}} \text{ and } \beta_J = \left[ \frac{X_J - (Y-2)}{2X_J} \right]^{\frac{1}{2}}$$

<sup>b</sup> For the E  ${}^2\Pi$  state of CaH, the special case of  $J' = 0.5$  corresponds to F<sub>1</sub>.

Table 6.3: Hönl-London Factors for  ${}^2\Pi\text{-}{}^2\Sigma^+$  transitions.

${}^2\Pi\text{-}{}^2\Sigma^+$	$\theta_{J'\Omega'par'J''\Omega''par''}^a$
$P_1(J)$	$\frac{(2J-1)^2 + (2J-1)X_{J-1}^{-1}(4J^2 - 4J - 7 + 2Y)}{8J}$
$Q_1(J)$	$\frac{(2J+1)[(4J^2 + 4J - 1) + X_J^{-1}(8J^3 + 12J^2 - 2J - 7 + 2Y)]}{8J(J+1)}$
$R_1(J)$	$\frac{(2J+3)^2 + (2J+3)X_{J+1}^{-1}(4J^2 + 12J + 9 - 2Y)}{8(J+1)}$
$P_{12}(J)$	$\frac{(2J-1)^2 - (2J-1)X_{J-1}^{-1}(4J^2 - 4J + 1 - 2Y)}{8J}$
$Q_{12}(J)$	$\frac{(2J+1)[(4J^2 + 4J - 1) - X_J^{-1}(8J^3 + 12J^2 - 2J + 1 - 2Y)]}{8J(J+1)}$
$R_{12}(J)$	$\frac{(2J+3)^2 - (2J+3)X_{J+1}^{-1}(4J^2 + 12J + 1 + 2Y)}{8(J+1)}$
$P_2(J)$	$\frac{(2J-1)^2 + (2J-1)X_{J-1}^{-1}(4J^2 - 4J + 1 - 2Y)}{8J}$
$Q_2(J)$	$\frac{(2J+1)[(4J^2 + 4J - 1) + X_J^{-1}(8J^3 + 12J^2 - 2J + 1 - 2Y)]}{8J(J+1)}$
$R_2(J)$	$\frac{(2J+3)^2 + (2J+3)X_{J+1}^{-1}(4J^2 + 12J + 1 + 2Y)}{8(J+1)}$
$P_{21}(J)$	$\frac{(2J-1)^2 - (2J-1)X_{J-1}^{-1}(4J^2 - 4J - 7 + 2Y)}{8J}$
$Q_{21}(J)$	$\frac{(2J+1)[(4J^2 + 4J - 1) - X_J^{-1}(8J^3 + 12J^2 - 2J - 7 + 2Y)]}{8J(J+1)}$
$R_{21}(J)$	$\frac{(2J+3)^2 - (2J+3)X_{J+1}^{-1}(4J^2 + 12J + 9 - 2Y)}{8(J+1)}$
$Q_{12}(0.5), Q_1(0.5)^b$	$\frac{4}{3}$
$P_{12}(1.5), P_1(1.5)^b$	$\frac{2}{3}$

<sup>a</sup>  $X_J = \left\{ (Y-2)^2 + 4 \left[ \left( J + \frac{1}{2} \right)^2 - 1 \right] \right\}^{\frac{1}{2}}$ ;  $Y = A/B$

<sup>b</sup> For the E  ${}^2\Pi$  state of CaH, the special case of  $J' = 0.5$  corresponds to F<sub>1</sub>.

Using the definitions outlined in this chapter, the HLFs derived for a  ${}^2\Pi\text{-}{}^2\Sigma$  transition (Table 6.3) are four times larger than the values calculated by Earls et al.<sup>128</sup>. The outputs of PGOPHER for the HLFs are consistent with the analytical formulae in Table 6.3, providing confidence in using PGOPHER to calculate Einstein A coefficients and line intensities.

## 6.3 Details of the calculations and the results

Potential energy functions,  $V_J(r)$ , for both the  $E^2\Pi$  and  $X^2\Sigma^+$  states of CaH were constructed using the purely numerical RKR method with the Kaiser correction<sup>136</sup> and the effective Dunham coefficients from Ram et al.<sup>44</sup>. These RKR potential curves were then employed in the LEVEL program to calculate the wavefunctions,  $\psi_{v,J}$ . Note that the current version of LEVEL is limited to singlet-singlet electronic transitions. Therefore, we use LEVEL and the high-level ab initio electronic transition dipole moments,  $\mathcal{R}_e(r)$ , from Weck et al. for the  $E^2\Pi\text{-}X^2\Sigma^+$  transition<sup>43</sup>, to calculate transition dipole moment matrix elements for R(0) lines of a  ${}^1\Pi\text{-}{}^1\Sigma$  transition, i.e.  $\langle v'J'_{=1}|\mathcal{R}_e(r)|v''J''_{=0}\rangle$ , for all 10 bands with  $v'=0,1$  and  $v''=0,1,2,3,4$ ; these are listed in Table 6.4. Considering the minor differences between  $\langle v'J'_{=1}|\mathcal{R}_e(r)|v''J''_{=0}\rangle$  and  $\langle v'J'_{=0}|\mathcal{R}_e(r)|v''J''_{=0}\rangle$ , less than 1% in this case,  $\langle v'J'_{=1}|\mathcal{R}_e(r)|v''J''_{=0}\rangle$  was used as the ‘rotationless matrix element’ in order to avoid Herman-Wallis fitting.

Einstein A coefficients and absolute line intensities for all 10 bands of the  $E^2\Pi\text{-}X^2\Sigma^+$  transition of CaH were calculated using PGOPHER. Firstly, the rovibronic transition wavenumbers were calculated using the spectroscopic constants derived by Shayesteh et al.<sup>137</sup> for  $v=0\text{-}4$  of the  $X^2\Sigma^+$

state and Ram et al.<sup>44</sup> for  $\nu=0,1$  of the  $E^2\Pi$  state. Next, the transition dipole moment matrix elements for R(0) lines of a  $^1\Pi-^1\Sigma$  transition listed in Table 6.4 for the 10 bands were inserted into PGOPHER and absolute line intensities calculated.

The absolute line intensities were used to determine the rotational temperature of the CaH sample in the experiments of Ref.<sup>44</sup>. PGOPHER has a useful function to determine the rotational temperature ( $T_R$ ).  $T_R$  was determined as  $778 \pm 3^\circ\text{C}$ , which compares well with the estimated experimental temperature of  $780^\circ\text{C}$ <sup>44</sup>. In the present study, the vibrational temperature,  $T_v$ , was set to equal to  $T_R$ .

Figure 6.1 shows the contour fit result using PGOPHER. The unfitted feature marked with triangle in the residuals is due to the weak argon atomic lines. In addition, two lines were locally perturbed and their positions have been marked with asterisks. These two perturbed lines were previously reported in Ref.<sup>44</sup>. The 1-1 band did not fit well due to the presence of perturbations. The  $E^2\Pi$  state probably interacts with the  $D^2\Sigma^+$  state or the higher vibrational levels of the  $B^2\Sigma^+$  state. As reported in Ref.<sup>44</sup>, the  $D^2\Sigma^+$  state lies only  $2132\text{ cm}^{-1}$  above the  $E^2\Pi$  state.

Finally, PGOPHER was used to generate a line list (including line positions, Einstein A coefficients and absolute line intensities) for the 10 bands of the  $E^2\Pi-X^2\Sigma^+$  transition of CaH for  $J$ -values up to 50.5. The line positions of the 0-0 band agree well with the experimental values apart from two locally perturbed lines. However, due to the perturbations in the 1-1 band as reported by Ram et al., the line positions have a larger standard deviation of  $0.02\text{ cm}^{-1}$ <sup>44</sup>. For the intensities, an overview of the comparison of experimental and simulated spectrum of 0-0 and 1-1 bands of  $E^2\Pi-X^2\Sigma^+$  transition of CaH is provided in Fig. 6.1. Similarly, a comparison for the  $Q_1$  and  $Q_2$  branches is provided in Fig. 6.2. As shown in Fig. 6.1 and 6.2, the simulated spectra agree very well with the experimental spectra.

There are four main sources of error in our calculations:

- 1) The uncertainty of the ab initio transition dipole moments, which were not discussed in Ref.<sup>43</sup>
- 2) The error from that transition dipole moment matrix elements for a  ${}^1\Pi\text{-}{}^1\Sigma$  transition are the same as the CaH  $E^2\Pi - X^2\Sigma^+$  transition. At lowest  $J$ , the difference is likely to be very small because this is basically equivalent to the validity of the Hund's case (a) basis. Furthermore, as demonstrated in Ref. <sup>123</sup>, the errors caused by using wave functions from RKR potentials are small.
- 3) Uncertainty by not including the rotation-vibration interaction, i.e., Herman-Wallis effect<sup>138</sup> in the calculation of line intensities.
- 4) Interaction of the  $E^2\Pi$  state with a close-lying  ${}^2\Sigma^+$  state. There is another  $D^2\Sigma^+$  state lying only  $2312\text{ cm}^{-1}$  above  $E^2\Pi$  state. Symmetry requires any resulting state mixing to be  $J$ -dependent.

Although, the uncertainty arising from source 2, 3 and 4 is hard to evaluate, the overall effect can be estimated by the standard deviation of the intensity fit which is less than 10% for  $Q_1$ ,  $Q_2$  and 15% for  $P_1$ ,  $P_2$  and  $R_1$ ,  $R_2$  branches.

Recently, Liu et al. have measured the lifetime of the  $A^2\Pi$  state of CaH<sup>139</sup>, which allows us to check our Hönl-London factors for a  ${}^2\Pi\text{-}{}^2\Sigma^+$  transition. Using the transition dipole moment function for the  $A^2\Pi\text{-}X^2\Sigma^+$  transition of CaH from Weck et al.<sup>43</sup>, the transition dipole moment at the ground state equilibrium geometry is 5.694 debye. Since the X and A state potentials are fairly similar, this value seems reasonable. Liu et al. quote a value of 5.655 debye as determined from the lifetime, which is in good agreement with the value derived from Weck et al. A final check was performed by calculating the lifetime using the value 5.694 debye for the transition dipole moment. PGOPHER gives a lifetime around 33 ns for the  ${}^2\Pi$  state, which is in good agreement with the measured lifetime 33.2 ns<sup>139</sup>.

Table 6.4: LEVEL outputs for a  ${}^2\Pi-{}^2\Sigma^+$  transition of CaH using RKR potentials and transition dipole moment function from Ref.<sup>43</sup>.

$\Delta J (J'')$	$v'$	$v''$	(Einstein A)/s <sup>-1</sup>	* $\langle v'J'   R   v''J'' \rangle$ /debye
R(0)	0	0	$1.04395 \times 10^6$	0.767167
R(0)	0	1	$1.58329 \times 10^3$	-0.032876
R(0)	0	2	$6.97259 \times 10^2$	0.024089
R(0)	0	3	$8.86349 \times 10^{-1}$	0.000952
R(0)	0	4	$7.46177 \times 10^{-3}$	-0.000097
R(0)	1	0	$4.16855 \times 10^3$	0.044494
R(0)	1	1	$1.05409 \times 10^6$	0.774310
R(0)	1	2	$1.90705 \times 10^2$	-0.011430
R(0)	1	3	$2.66231 \times 10^3$	0.047015
R(0)	1	4	$5.94906 \times 10^{-2}$	-0.000246

\* Vibronic transition moment input to PGOPHER.

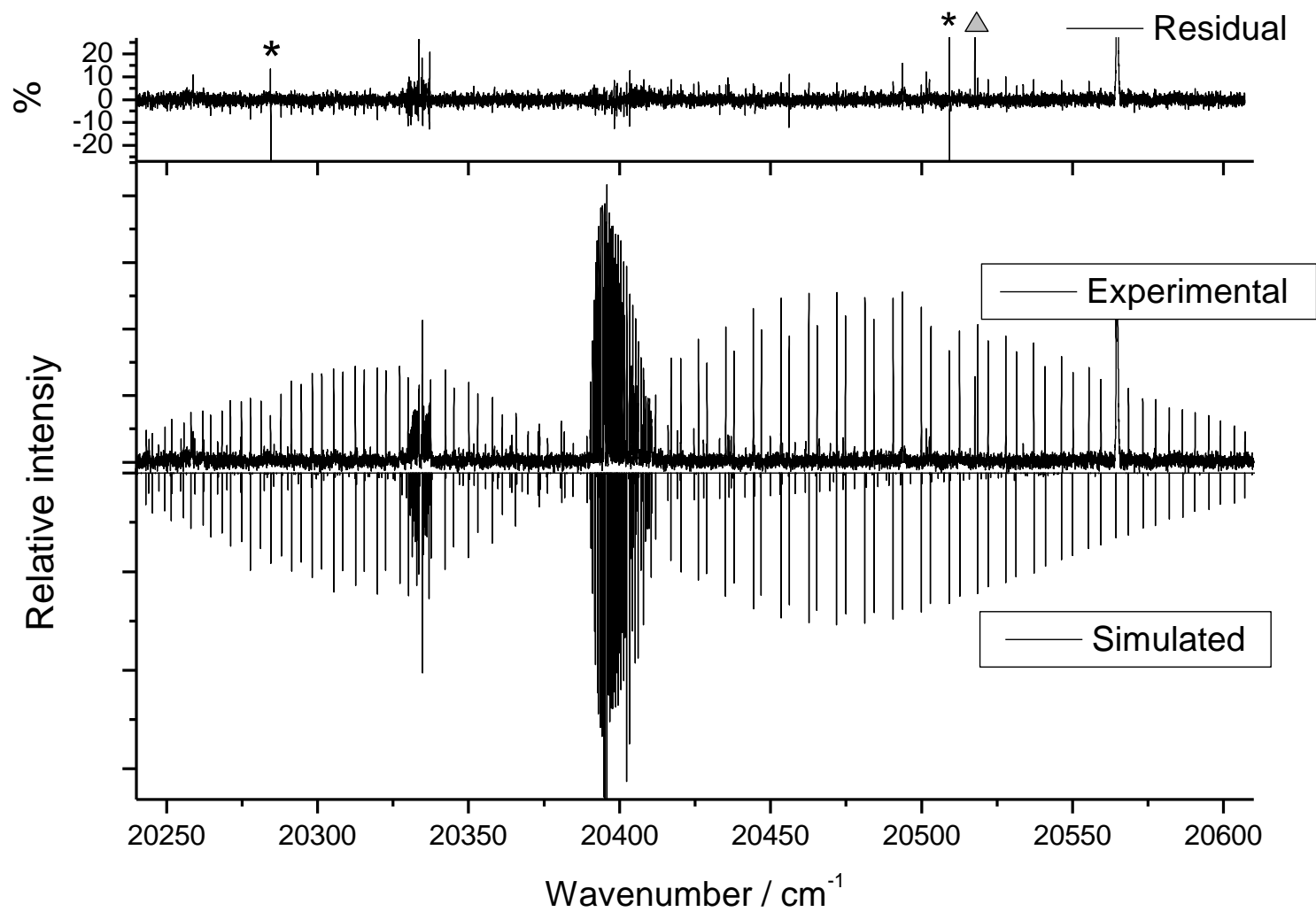


Figure 6.1: Overview of experimental (upper curve) and simulated (lower curve) spectra for the 0-0 and 1-1 bands of the  $E^2\Pi-X^2\Sigma^+$  transition of CaH. In the top panel, the residuals (observed minus calculated spectra) are displayed as a percentage with the largest peak in the experimental spectrum set to 100%.

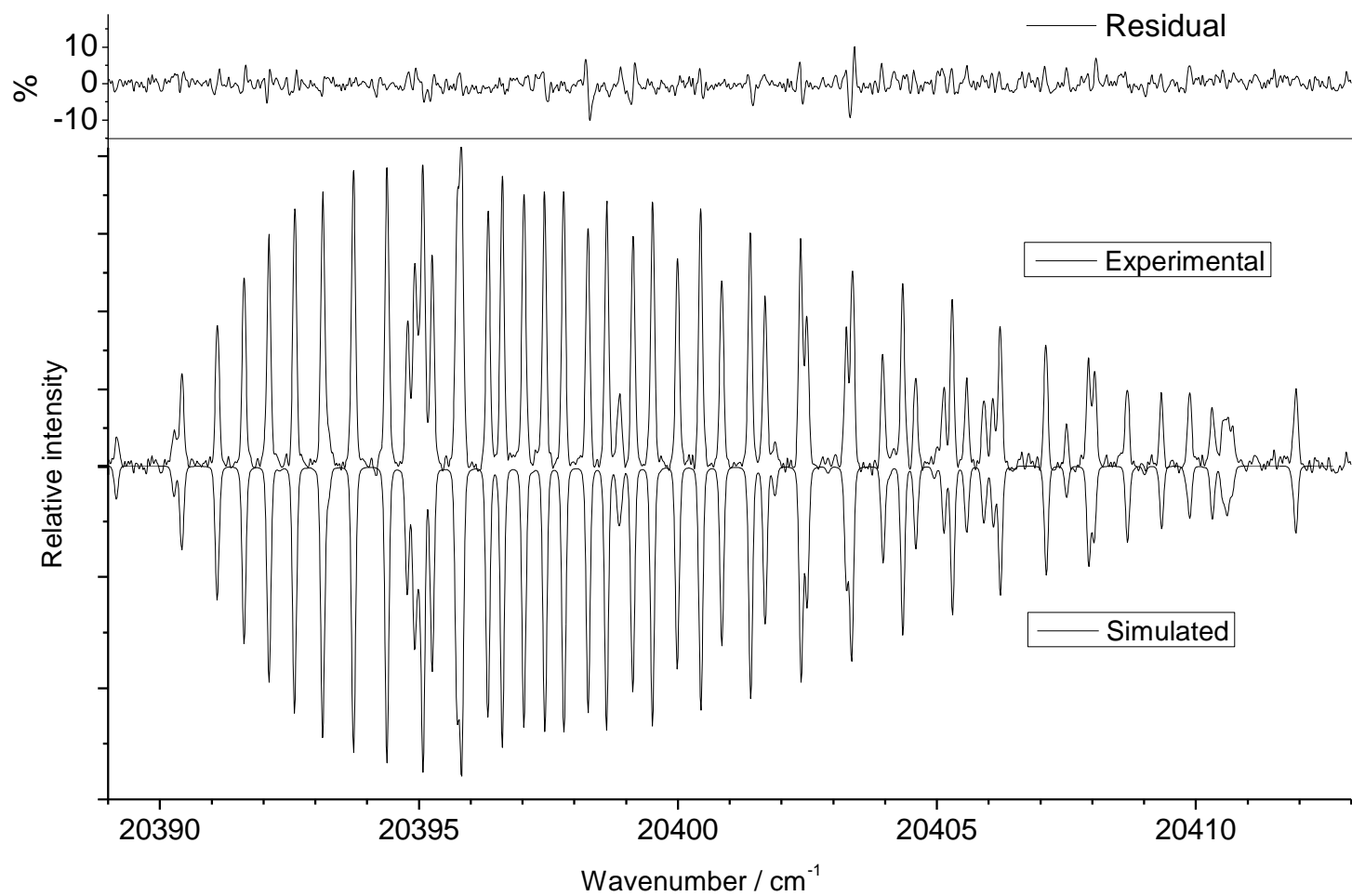


Figure 6.2: Experimental (upper) and simulated (lower) spectra of the  $Q_1$  and  $Q_2$  branches of the 0-0 band of the  $E^2\Pi-X^2\Sigma^+$  transition of CaH. In the top panel, the residuals are displayed as a percentage with the largest peak in the experimental spectrum set to 100%.

## 6.4 Conclusion and future work

Computed transition dipole moments<sup>43</sup> and the spectroscopic constants from a recent study<sup>44</sup> have been used with the PGOPHER program to generate line lists containing Einstein A coefficients and absolute line intensities for 10 bands of the E<sup>2</sup>Π-X<sup>2</sup>Σ<sup>+</sup> transition of CaH for  $J$ -values up to 50.5. The line intensities have enabled the determination of a rotational temperature,  $T_R$ , of  $778 \pm 3^\circ\text{C}$  for the CaH sample in Ref.<sup>44</sup>. The calculated line intensities agree well with experimental values, with a standard deviation of 10% for Q<sub>1</sub>, Q<sub>2</sub> and 15% for P<sub>1</sub>, P<sub>2</sub> and R<sub>1</sub>, R<sub>2</sub> branches.

Analytical formulae for Hönl-London factors have been derived for a <sup>2</sup>Π - <sup>2</sup>Σ<sup>+</sup> transition using a spherical tensor approach, with the <sup>2</sup>Π state intermediate between Hund's case (a) and case (b) coupling. Our derived formulae are a factor of 4 larger than those by Earls et al.<sup>128</sup>. A further examination reveals that our derivation agrees with the sum rule in Ref.<sup>134</sup>, which has become standard. Our analytical formulae for HLFs in Table 6.3 agree with values given by PGOPHER for the <sup>2</sup>Π - <sup>2</sup>Σ<sup>+</sup> transition. These HLFs were validated by comparing the upper-state lifetime calculated by PGOPHER for the A<sup>2</sup>Π - X<sup>2</sup>Σ<sup>+</sup> transition of CaH (using *ab initio* transition dipole moments<sup>43</sup>) with the experimental lifetime<sup>139</sup>; these are in good agreement.

The present study has demonstrated that the use of LEVEL and PGOPHER significantly simplifies the procedure of calculating Einstein A coefficients and absolute line intensities. However, some improvements are still needed. The current version of PGOPHER cannot accept internuclear distance dependent  $\mathcal{R}_e(r)$  to calculate the transition dipole moments. Thus rotation-vibration interaction, i.e., Herman-Wallis effect<sup>138</sup> was ignored in calculating the line intensities.

# Chapter 7

## High Resolution Laser Excitation Spectroscopy of Barium Monosulfide

### 7.1 Introduction

The interest in solid BaS dates back to the early 17<sup>th</sup> century when a white mineral (barite, BaSO<sub>4</sub>) was found near Bologna, Italy. After reduction of the powder with charcoal at high temperature to form at least some BaS, the material ('Bologna stone') became phosphorescent. Bologna stone drew the attention of various of alchemists, chemists and philosophers due to its 'magic' property of emitting light in darkness for hours<sup>140</sup>. It was an important object for scientific study of luminescent phenomena<sup>141</sup>. In modern chemistry, the inorganic compound BaS has been used as precursor to other barium compounds including BaCO<sub>3</sub> and the pigment lithopone, ZnS/BaSO<sub>4</sub><sup>142</sup>. Barium sulfide also finds application as an optical material<sup>143-145</sup>. Alkaline earth metal sulfides including BaS have drawn the attention of spectroscopists for their potential astrophysical applications<sup>146</sup>.

The electronic states of diatomic oxides and sulfides have been extensively studied in the past few decades<sup>147-153</sup>. Studies of the low-lying electronic states of BaS may be traced back to 1937 when Mathur observed only a region of continuous absorption and measured its latent heat of vaporization<sup>154</sup>. In 1971, Barrow et al. rotationally analyzed

several bands of the  $A^1\Sigma^+ - X^1\Sigma^+$  and the  $B^1\Sigma^+ - X^1\Sigma^+$  transitions using absorption spectroscopy at moderate resolution<sup>147</sup>. Preliminary constants were derived for the  $A^1\Sigma^+$  and  $B^1\Sigma^+$  states in this work and the  $A^1\Sigma^+$  state was found to be extensively perturbed by several other low-lying electronic states, which were later identified as the  $A^1\Pi$  and the  $a^3\Pi$  states by Cummins et al<sup>148</sup>.

The molecular beam electric resonance technique was used to derive a dipole moment of  $10.86 \pm 0.02$  D for the ground state of BaS<sup>151</sup>. The first pure rotational measurement was carried out by Tiemann et al. in 1976<sup>153</sup>. In this work, the rotational transitions below 70 GHz for the main barium sulfide isotopologue  $^{138}\text{Ba}^{32}\text{S}$  were analyzed<sup>153</sup>. Four years later, Helms et al. extended the measurements to six isotopologues of BaS in the 55–339 GHz spectral range which yielded accurate Durham constants for the ground state<sup>149</sup>. In 1981, Cummins et al. investigated three low lying electronic states,  $A^1\Sigma^+$ ,  $A^1\Pi$  and  $a^3\Pi$ , using dispersed fluorescence spectroscopy<sup>148</sup>. A cw argon ion laser was used to excite BaS molecules to the  $B^1\Sigma^+$  state. Fluorescence spectra of the  $B^1\Sigma^+ - A^1\Sigma^+$ ,  $B^1\Sigma^+ - A^1\Pi$  and  $B^1\Sigma^+ - a^3\Pi$  transitions were rotationally assigned. In conjunction with the data from Barrow et al., they were able to analyze the mutual perturbations between the  $A^1\Sigma^+$ , the  $A^1\Pi$  and the  $a^3\Pi$  states and obtain deperturbed constants. Very recently, Janczyk and Ziurys performed a pure rotational study of BaS ( $X^1\Sigma^+$ ) in the frequency range of 355-396 GHz<sup>150</sup>. This work tackled all six isotopologues,  $^{138}\text{Ba}^{32}\text{S}$ ,  $^{137}\text{Ba}^{32}\text{S}$ ,  $^{136}\text{Ba}^{32}\text{S}$ ,  $^{135}\text{Ba}^{32}\text{S}$ ,  $^{134}\text{Ba}^{32}\text{S}$ , and  $^{138}\text{Ba}^{34}\text{S}$  and the results covered the vibrational levels from  $v=0$  to  $v=6$ .

In this chapter, we report on high resolution laser excitation spectra of the  $A^1\Pi - X^1\Sigma^+$  and  $a^3\Pi - X^1\Sigma^+$  electronic transitions in the 12100-12765  $\text{cm}^{-1}$  spectral region. Our new observations contain the 2-1, 3-1, 3-2, 4-2, 5-2 and 5-3 vibrational bands of the  $A^1\Pi - X^1\Sigma^+$  transition and the 4-1, 5-1, 5-2 vibrational bands of the  $a^3\Pi_1 - X^1\Sigma^+$  transition. A large number of lines were measured for both transitions for the main

isotopologue  $^{138}\text{Ba}^{32}\text{S}$  (67.5%). The measured wavenumbers together with the microwave data from Helms et al.<sup>149</sup>, Tiemann et al.<sup>153</sup>, sub-millimeter data from Janczyk and Ziurys<sup>150</sup> and the lines for the  $A^1\Sigma^+-X^1\Sigma^+$  transition from Morbi and Bernath<sup>152</sup> were fitted simultaneously. Spectroscopic constants of the  $A^1\Pi$  and the  $a^3\Pi_1$  states were obtained and perturbations were observed for the  $A^1\Pi$  state.

## 7.2 Experimental detail

Barium sulfide was synthesized by reacting barium atoms with carbon disulfide ( $\text{CS}_2$ ) in a Broida-type oven. The setup of Broida-type oven can be found elsewhere in detail<sup>8</sup> as well as in chapter 2. In brief, about 5 grams of barium metal was placed in an alumina crucible which was resistively heated by a tungsten wire basket to vaporize the metal. Reagent grade  $\text{CS}_2$  vapor from a liquid reservoir was then introduced as the oxidant. In order to prevent formation of  $\text{BaO}$ , the reservoir was pumped for two minutes prior to the experiment to remove all dissolved oxygen from the  $\text{CS}_2$ . Argon was used as the carrier gas to entrain Ba vapor into the reaction zone of the oven. The partial pressure of argon and  $\text{CS}_2$  used in the experiment were 2.3 Torr and 8 mTorr, respectively. When the oven reached an appropriate temperature a grey chemiluminescent flame approximately 2 cm high, with a slightly bluish color was observed after  $\text{CS}_2$  vapor was introduced.

A continuous-wave single-mode ring-type titanium:sapphire laser (Coherent 899-29) were used to excite the BaS molecules. The output power of the laser varied from 200 to 500 mW when scanning over the 12000-12750  $\text{cm}^{-1}$  spectral region. The laser beam was introduced from above the oven into the flame through a Brewster window on top of the oven. Fluorescence could be observed through an infrared viewer during scanning. Maximum fluorescence was achieved by tweaking the partial pressure of argon carrier gas and  $\text{CS}_2$  oxidant. The fluorescence was

collected and aligned using two lenses and was focused into a monochromator (3 mm slit width) which functioned as a band-pass filter. The monochromator was then set at 858.0 nm which was approximately the calculated 1-0 band origin of the  $A^1\Pi - X^1\Sigma^+$  transition of BaS. This monochromator position was fixed while the laser was scanned through the spectral range of interest. As the laser was scanned, the optical signal from the monochromator was detected using a photo multiplier tube (PMT). Phase-sensitive detection was realized by chopping the laser beam and feeding the electronic signal from the PMT into a lock-in amplifier which was phase-locked by a reference signal from the mechanical chopper. The output of the lock-in amplifier was then sent to the PC which controlled the laser scanning. Spectra were recorded every  $5\text{ cm}^{-1}$  segments at a scan speed of 2 GHz per second. In order to calibrate the laser frequency simultaneously, the laser beam was split and a small portion (5%) was sent to a heated  $I_2$  cell to record the  $I_2$  absorption spectra together with BaS spectra. The BaS spectra were observed from 12100 to  $12765\text{ cm}^{-1}$ . Figure 7.1 shows a section of the recorded laser excitation spectrum of BaS showing the branch structure of the 4-2 band of the  $A^1\Pi - X^1\Sigma^+$  transition. The signal-to-noise ratio is estimated to be on the order of 100 for the most intense lines.

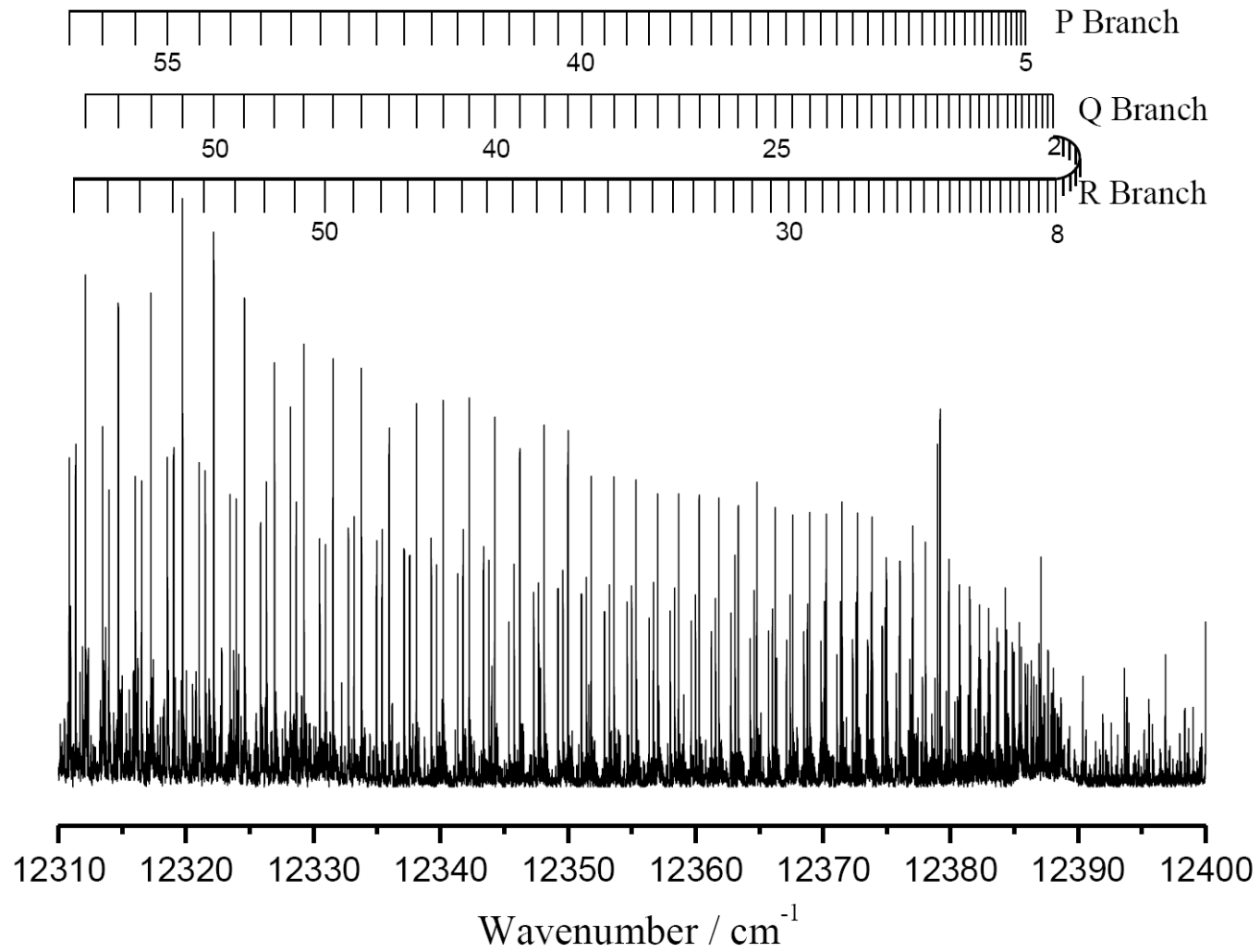


Figure 7.1: The laser excitation spectrum of the  $v' = 4 - v'' = 2$  band of the  $A^1\Pi - X^1\Sigma^+$  transition of BaS. The  $J$  assignments are labelled on the top of the spectrum.

In order to analyse the spectra, the line positions were firstly fitted with a Voigt lineshape function using M. Carleer's WSpectra program<sup>65</sup>. The absolute frequency was calibrated with the absorption spectrum of heated iodine using the ALTAS database<sup>155</sup>. A Loomis-Wood program was then employed to identify the bands with the  $J$  values assigned using lower state combination differences.

## 7.3 Results and discussion

### 7.3.1 Rotational assignment

Our measurements contain a large number of lines belonging to different isotopologues of BaS. So far only the bands of the main isotopologue  $^{138}\text{Ba}^{32}\text{S}$  (67.5%) have been analysed. The band structure of a typical band of the  $A^1\Pi - X^1\Sigma^+$  transition is illustrated by the 4-2 band shown in Fig. 7.1. As shown in Fig. 7.1, the rotational structure of each band of this transition consists of three branches, one P, one Q, and one R branch. The Q branch is the most intense, and the R and P branches have similar intensity. The rotational assignments for lines of the P and R branches were made using lower state combination differences. Sub-millimeter data from Janczyk and Ziurys<sup>150</sup> for the ground state was used to confirm the absolute  $J$  assignments. Lines of Q branch were then fitted together with P and R branches using a weighted least-squares fit program called lsqWIN. The complete rotational term values including the first order centrifugal distortion term used in the least-squares fit are expressed as follows for a  $^1\Sigma^+$  and a  $^1\Pi$  state, respectively:

$$F_{\Sigma}(v, J) = B_v J(J + 1) - D_v [J(J + 1)]^2,$$

and

$$F_{\Pi}(v, J) = B_v J(J + 1) - D_v [J(J + 1)]^2 \pm \frac{1}{2} q_v [J(J + 1)]^2.$$

In total, six vibrational bands including the 2-1, 3-1, 3-2, 4-2, 5-2, and the 5-3 band of the  $A^1\Pi - X^1\Sigma^+$  transition were rotationally analyzed.

As reported by Cummins et al., the  $a^3\Pi$  state lies very close to the  $A^1\Pi$  state<sup>148</sup>. The  $a^3\Pi$  state may be treated approximately as a Hund's case (c) state where each of the three spin components,  $^3\Pi_{0\pm}(F_1)$ ,  $^3\Pi_1(F_2)$  and  $^3\Pi_2(F_3)$  is viewed as a separate electronic state. The approximate selection rule  $\Delta S = 0$  does not hold strictly when there is a large spin-orbit interaction in heavy molecules such as BaS. For a Hund's case (c) state, only the quantum number  $\Omega$ , the projection of the total electronic angular momentum about the internuclear axis, is well defined in addition to  $J$  and parity. As a result, the selection rule is:  $\Delta\Omega = 0, \pm 1$ .

On account of the above selection rule, only the sub-bands,  $^3\Pi_{0+}^{-1}\Sigma^+$  and  $^3\Pi_1^{-1}\Sigma^+$  occur. The structure of these bands is of the same as that of singlet bands, namely  $^3\Pi_{0+}^{-1}\Sigma^+$  transitions are similar to  $^1\Sigma^+ \rightarrow ^1\Sigma^+$  transitions (one P and one R branch); and  $^3\Pi_1^{-1}\Sigma^+$  transitions are similar to  $^1\Pi \rightarrow ^1\Sigma$  transitions (one P, one R and one Q branch). The observed bands of the  $a^3\Pi_1 - X^1\Sigma^+$  transition of BaS are fairly strong, nearly one third of the strongest  $A^1\Pi - X^1\Sigma^+$  band. A similar approach as for the  $A^1\Pi - X^1\Sigma^+$  transition was used to perform the rotational assignments and rotational constants derived from the least-squares fit are listed in Table 7.3. No local perturbations were observed in the bands that were rotationally analyzed.

### 7.3.2 Vibrational assignment

The vibrational assignment of the BaS spectra was facilitated by the vibrational parameters reported by Cummins et al.<sup>148</sup>. They have performed a perturbation analysis accounting for the  $X^1\Sigma^+ \sim A^1\Pi \sim a^3\Pi$  mutual perturbations and the deperturbed locations of the  $A^1\Pi$  state and the  $a^3\Pi_1$  spin component were reported. The observed  $A^1\Pi$  and  $a^3\Pi_1$  band

origins shifted from their deperturbed positions by the spin-orbit interaction. Thus, the  $A^1\Pi$  energy should be raised and  $a^3\Pi_1$  should be lowered by  $91\text{ cm}^{-1}$  in order to predict our observed band origins. Table 7.1, which is a Deslandres table, shows the calculated band positions of the  $A^1\Pi - X^1\Sigma^+$  transition using the customary expression<sup>51</sup> and the vibrational parameters derived by Cummins et al. including the spin-orbit shift. The predict band positions have an accuracy better than  $0.5\text{ cm}^{-1}$  and are in good agreement with the observed band heads. According to the Deslandres table, nine vibrational bands of the main isotopologue  $^{138}\text{Ba}^{32}\text{S}$  are within the scanned spectral region of  $12100\text{-}12760\text{ cm}^{-1}$ . However, only six of them were observed. To explain this, Franck-Condon factors were calculated for  $v' \leq 6$  and  $v'' \leq 4$  of the  $A^1\Pi - X^1\Sigma^+$  transition of BaS. A program called LEVEL was used to accomplish the Franck-Condon calculation with the potentials calculated using the RKR method for both states. The RKR potentials were constructed using the derived vibrational constants in Table 7.4 for the  $A^1\Pi$  state and Ref. <sup>152</sup> for the  $X^1\Sigma^+$  states. Figure 7.2 shows the 3-D bar plot of the calculated Franck-Condon factors for the transitions involving  $v' = 0 - 6$  and  $v'' = 0 - 4$ . Possible vibrational bands in our experimental region are marked with asterisks. As can be seen in this plot, the Franck-Condon factors for the  $0 - 0$ ,  $1 - 0$  and  $2 - 0$  bands are much smaller than the others. This explains why these bands were not present in the scanned spectra. It is worth to be noted that the spectra were recorded over four days and the oven conditions changed from time to time so the experimental band intensities are unreliable. However, there is a rough agreement in the intensity trends between the observed spectra and the calculated results. The vibrational assignments of the  $a^3\Pi_1 - X^1\Sigma^+$  bands were also assisted by a Deslandres table calculated using constants from Ref.<sup>148</sup>.

Table 7.1: Deslandres table of band origins of the  $A^1\Pi - X^1\Sigma^+$  transition of  $^{138}\text{Ba}^{32}\text{S}$

$v' \setminus v''$	0		1		2		3
0	12116.0	377.6	11738.4	375.9	11362.5	374.1	10988.4
	259.1		259.1		259.1		259.1
1	12375.1	377.6	11997.5	375.9	11621.6	374.1	11247.5
	257.3		257.3		257.3		257.3
2	12632.4	377.6	12254.7*	375.9	11878.9	374.1	11504.7
	255.4		255.4		255.4		255.4
3	12887.8	377.6	12510.1*	375.9	12134.3*	374.1	11760.1
	253.5		253.5		253.5		253.5
4	13141.3	377.6	12763.7	375.9	12387.8*	374.1	12013.7
	251.7		251.7		251.7		251.7
5	13393.0	377.6	13015.4	375.9	12639.5*	374.1	12265.4*

Note: bands observed in present study are marked with (\*).

Table 7.2: Franck-Condon factors for the  $A^1\Pi - X^1\Sigma^+$  transition of  $^{138}\text{Ba}^{32}\text{S}$ 

$v' \setminus v''$	0	1	2	3	4
0	6.82E-06	9.26E-05	6.15E-04	2.67E-03	8.49E-03
1	7.00E-05	7.96E-04	4.35E-03	1.51E-02	3.70E-02
2	3.68E-04	3.47E-03	1.53E-02	4.11E-02	7.40E-02
3	1.33E-03	1.02E-02	3.53E-02	7.04E-02	8.51E-02
4	3.67E-03	2.27E-02	5.97E-02	8.25E-02	5.56E-02
5	8.32E-03	4.04E-02	7.75E-02	6.55E-02	1.41E-02
6	1.61E-02	5.99E-02	7.79E-02	3.08E-02	4.64E-04

\*Observed bands in this study are highlighted in square boxes.

Table 7.3: Molecular parameters of BaS from a global least-squares fit

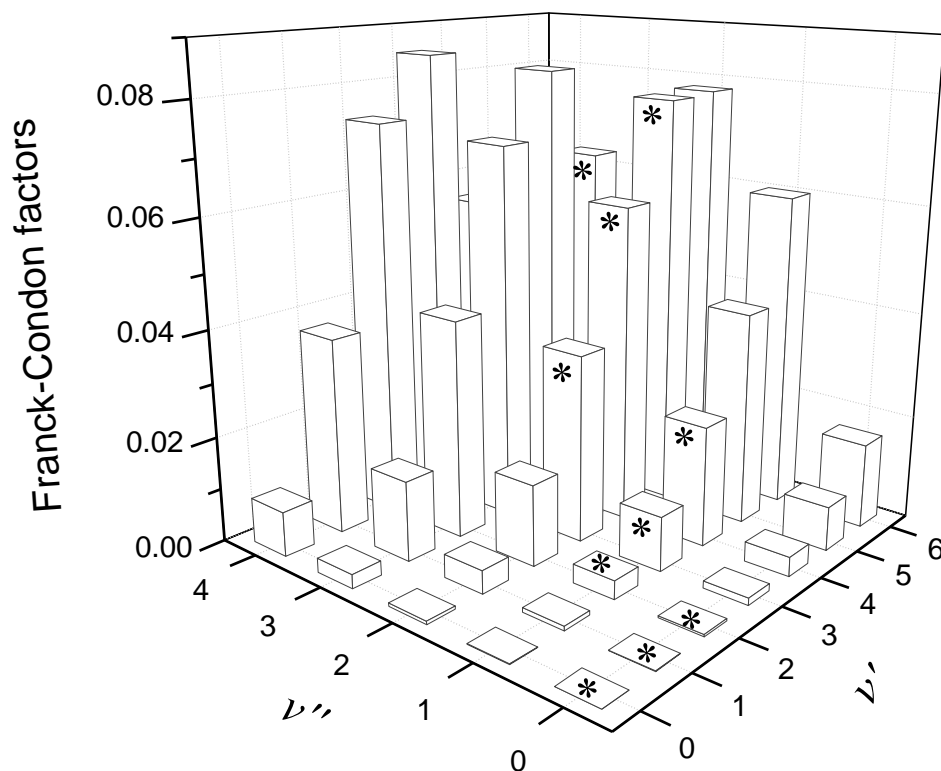
State	$v$	$T_v$ /cm <sup>-1</sup>	$B_v$ /cm <sup>-1</sup>	$D_v$ /10 <sup>-8</sup> ×cm <sup>-1</sup>	$q_v$ /10 <sup>-5</sup> ×cm <sup>-1</sup>
X <sup>1</sup> Σ <sup>+</sup>	0	0	0.1031565471(24)	3.066280(39)	~
	1	377.62824(50)	0.1028405690(53)	3.071952(73)	~
	2	753.51028(54)	0.1025237193(38)	3.077753(53)	~
	3	1127.63272(59)	0.1022059039(81)	3.08265(11)	~
A <sup>1</sup> Σ <sup>+</sup>	2	15027.17407(92)	0.0904153(36)	-26.934(278)	~
	3	15302.17546(58)	0.0913988(20)	-0.530(128)	~
	4	15579.49514(62)	0.0915935(25)	10.857(191)	~
	5	15859.72426(71)	0.0914360(35)	17.002(370)	~
	6	16140.5525(12)	0.0913638(47)	11.652(412)	~
	7	16421.0228(22)	0.0896986(83)	-36.139(680)	~
	8	16696.97824(90)	0.0901358(17)	-2.895(79)	~
	9	16969.88155(80)	0.0899553(19)	4.366(108)	~
	A <sup>1</sup> Π	2	12632.40645(85)	0.08091439(61)	3.006(11)
3		12887.71574(57)	0.08059585(29)	3.2940(66)	-1.911(14)
4		13141.37110(61)	0.08028891(23)	3.2474(33)	-2.026(15)
5		13392.98500(59)	0.08003811(18)	3.5521(25)	1.9984(77)
-		-	-	-	-
a <sup>3</sup> Π <sub>1</sub>	4	12710.42715(62)	0.08048896(31)	3.1077(48)	0.984(20)
	5	12962.70210(57)	0.08017305(26)	3.3140(50)	1.2022(96)

Note: numbers in parentheses are one standard deviation uncertainty in the last digits.

Table 7.4: Derived equilibrium spectroscopic constants for BaS

State	$T_e$ /cm <sup>-1</sup>	$\omega_e$ /cm <sup>-1</sup>	$\omega_e x_e$ /cm <sup>-1</sup>	$B_e$ /10 <sup>-2</sup> ×cm <sup>-1</sup>	$\alpha_e$ /10 <sup>-4</sup> ×cm <sup>-1</sup>	$R_e$ (Å)
A <sup>1</sup> Π	12175.230(785)	260.961(397)	0.9270(476)	8.1577(61)	2.81(13)	2.8217(86)
a <sup>3</sup> Π <sub>1</sub>	~	~	~	8.191056(57)	3.1590(98)	2.815919(80)

Note: numbers in parentheses are one standard deviation uncertainty in the last digits.



In the BaS spectra bands with Q heads at 12233, 12265, 12664, 12699  $\text{cm}^{-1}$  were found. A careful investigation suggested that these bands belong to the  $A^2\Pi_{3/2}-X^2\Sigma^+$  transition of BaF<sup>156</sup>. It is not clear where the BaF impurity came from, either from the CS<sub>2</sub> solvent or some fluoride salts in the oven from previous experiments.

A final fit was performed varying all the constants for both ground and excited states. Morbi's data<sup>152</sup> were also included in our global fit. Local perturbations were found for Q lines between  $J=64$  and  $J=76$  from the  $v = 4$  of the  $a^3\Pi_1$  state to  $v = 1$  of the  $X^1\Sigma^+$  state. These lines were de-weighted in the global fit. Table 7.3 presents the rotational constants for all the bands included in our final fit. The values of the  $\Lambda$ -doubling constants,  $q_v$ , are irregular in the vibrational levels of the  $A^1\Pi$  state because of interactions with nearby electronic states. The precision of our line positions is estimated to be 0.002  $\text{cm}^{-1}$  for unblended lines. Equilibrium molecular parameters were derived using rotational constants in Table 7.3. Due to global perturbations the band constants are an irregular function of  $v$ ; as a consequence there are large errors in the derived equilibrium constants.

## 7.4 Conclusions:

The present laser spectroscopic investigation of the  $A^1\Pi$  and  $a^3\Pi_1$  states of BaS has improved the molecular constants of the two states<sup>148</sup>. The line width of our data is about 0.018  $\text{cm}^{-1}$ , limited by Doppler broadening in the flame in the Broida oven. Transitions involving  $a^3\Pi_{0+}$  spin component were not observed in this work. Calculations of Franck-Condon factors for the  $A^1\Pi-X^1\Sigma^+$  transition were performed, which explained why the 0-0, 1-0 and 2-0 bands were not measured.

High resolution laser excitation spectra from the ground  $X^1\Sigma^+$  to the  $A^1\Pi$  and the  $a^3\Pi$  states in the 12100-12765  $\text{cm}^{-1}$  spectral region have been

recorded and analysed. Our new measurements contain the 2-1, 3-1, 3-2, 4-2, 5-2, 5-3 vibrational bands of the  $A^1\Pi - X^1\Sigma^+$  transition and the 4-1, 5-1, 5-2 vibrational bands of the  $a^3\Pi_1 - X^1\Sigma^+$  transition. A large number of lines were measured for both transitions for the main isotopologue. The measured wavenumbers together with the microwave data<sup>149, 153</sup>, sub-millimeter data<sup>150</sup> and lines for the  $A^1\Sigma^+ - X^1\Sigma^+$  transition from Morbi and Bernath<sup>152</sup> were fitted together to obtain improved spectroscopic constants for the  $A^1\Pi$  and  $a^3\Pi_1$  states. From the individual band parameters, equilibrium constants were derived for the  $A^1\Pi$  and  $a^3\Pi_1$  states. However, these equilibrium constants have large uncertainties due to the global perturbations among the  $A^1\Sigma^+$ ,  $A^1\Pi$  and  $a^3\Pi$  states as observed by Cummins et al.<sup>148</sup>.

# Chapter 8

## Future work

### 8.1 Boron-containing species

#### 8.1.1 HBO and FBO

In Chapters 3 and 4 the infrared spectra of BO and HBS were analysed and the spectroscopic constants were obtained. Computational study of HBS was performed using the recently developed CCSD(T)-F12 method. One on hand, the computational work strongly supported our assignment of hot bands; on the other hand, our experimental results served as a benchmark to test the current theory of quantum chemistry<sup>91</sup>. In addition to BO band HBS, infrared spectra of HBO and FBO were also recorded (see Figures 8.1, 8.2 and 8.3). Further analysis of these spectra is in working progress.

Previous infrared investigation of HBO was undertaken by Kawashima et al.<sup>63</sup> in 1986. They recorded a few lines of the  $\nu_3$  fundamental band of H<sup>11</sup>BO by diode laser spectroscopy. One year later, they determined the rotational constants and nuclear quadruple coupling constants for H<sup>11</sup>BO and H<sup>10</sup>BO using a millimeter-wave spectrometer<sup>157</sup>. In 1989, they extended their microwave observations on HBO and determined the molecular constants with improved accuracy and reliability<sup>158</sup>. So far, however, no HBO spectra have been recorded for the  $\nu_1$  and  $\nu_2$  fundamental bands, or for hot bands. Therefore, we have undertaken Fourier transform IR measurements of HBO in our laboratory. Our new observations in the 1200-4000 cm<sup>-1</sup> region contain the  $\nu_1$  and

$\nu_3$  fundamental modes,  $2\nu_2$  and  $2\nu_3$  overtone bands, plus numerous hot bands. However, the assignment of the more than twenty hot bands associated with each of  $\nu_1$  and  $\nu_3$  is very difficult. Similar to the study of HBS in Chapter 4, ab initio calculations were vital for the assignment of the hot bands. We thus followed the same procedure to finish our assignments of the HBO hot bands.

The first low resolution spectrum of FBO was recorded by Yoder<sup>159</sup> by heating the mixture of  $\text{BF}_3$  and air to 3000-5000 Kelvin in a d.c. arc jet. In 1979, Boyer<sup>160</sup> carried out an infrared measurement of FBO by reacting  $\text{BF}_3$  with  $\text{O}_2$  in the shock-tube. In 1987, Kawashima et al.<sup>161</sup> recorded the first high resolution infrared spectra of FBO in the region 2050-2140  $\text{cm}^{-1}$ . They have assigned the  $\nu_1$  fundamental mode (B-O stretching) of  $\text{F}^{11}\text{BO}$  and  $\text{F}^{10}\text{BO}$ , and the  $\nu_1 + \nu_2 - \nu_2$  hot band of  $\text{F}^{11}\text{BO}$ . The microwave measurement was carried out by Gatehouse et al.<sup>162</sup> in the 8–26 GHz frequency range using a pulsed jet cavity Fourier transform microwave spectrometer. Our new observation of FBO in 2000-2200  $\text{cm}^{-1}$  region has improved SNR and contains many more hot bands.

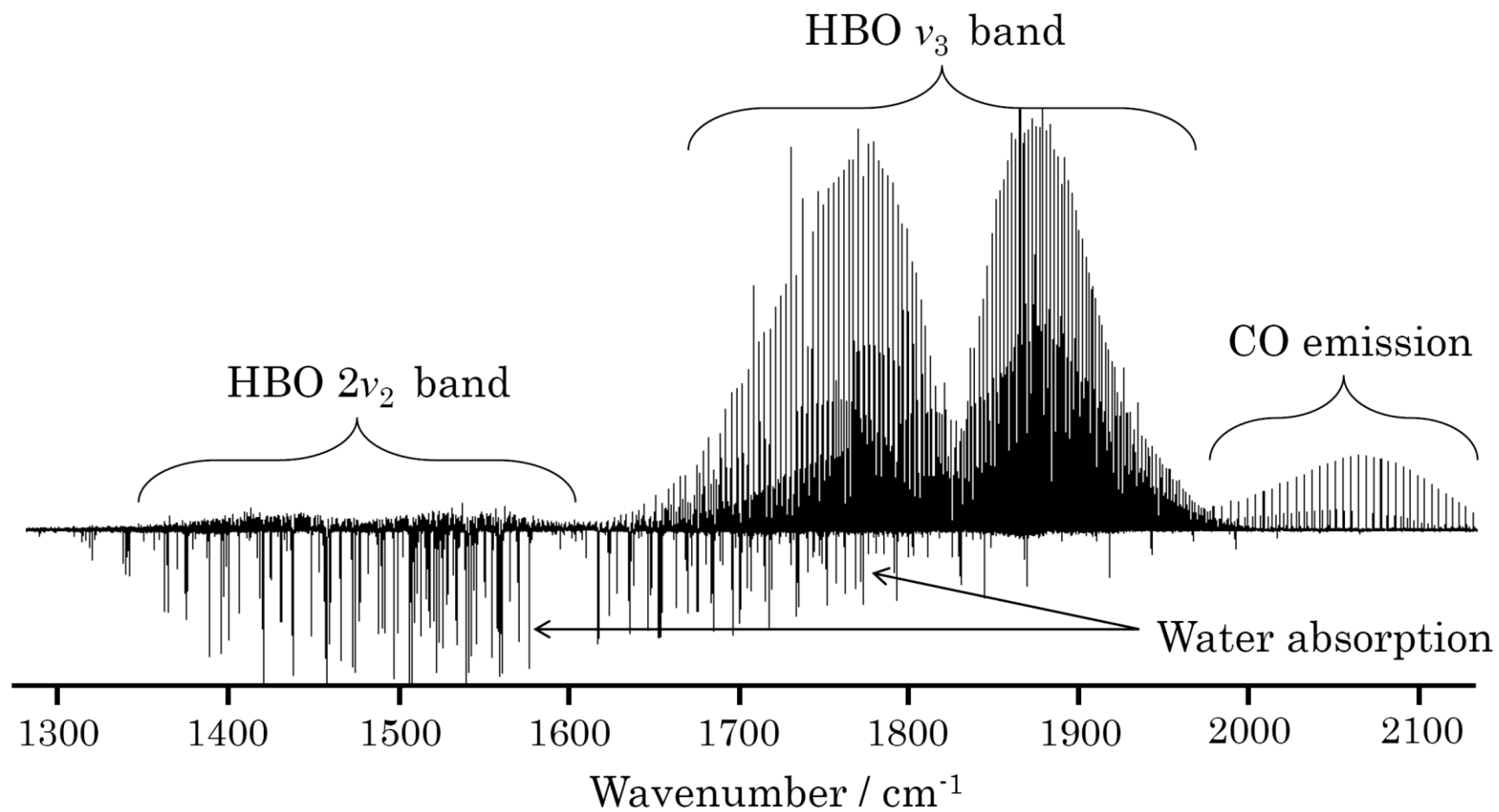


Figure 8.1: High resolution Fourier transform emission spectrum of HBO  $\nu_3$  fundamental and  $2\nu_2$  overtone bands.

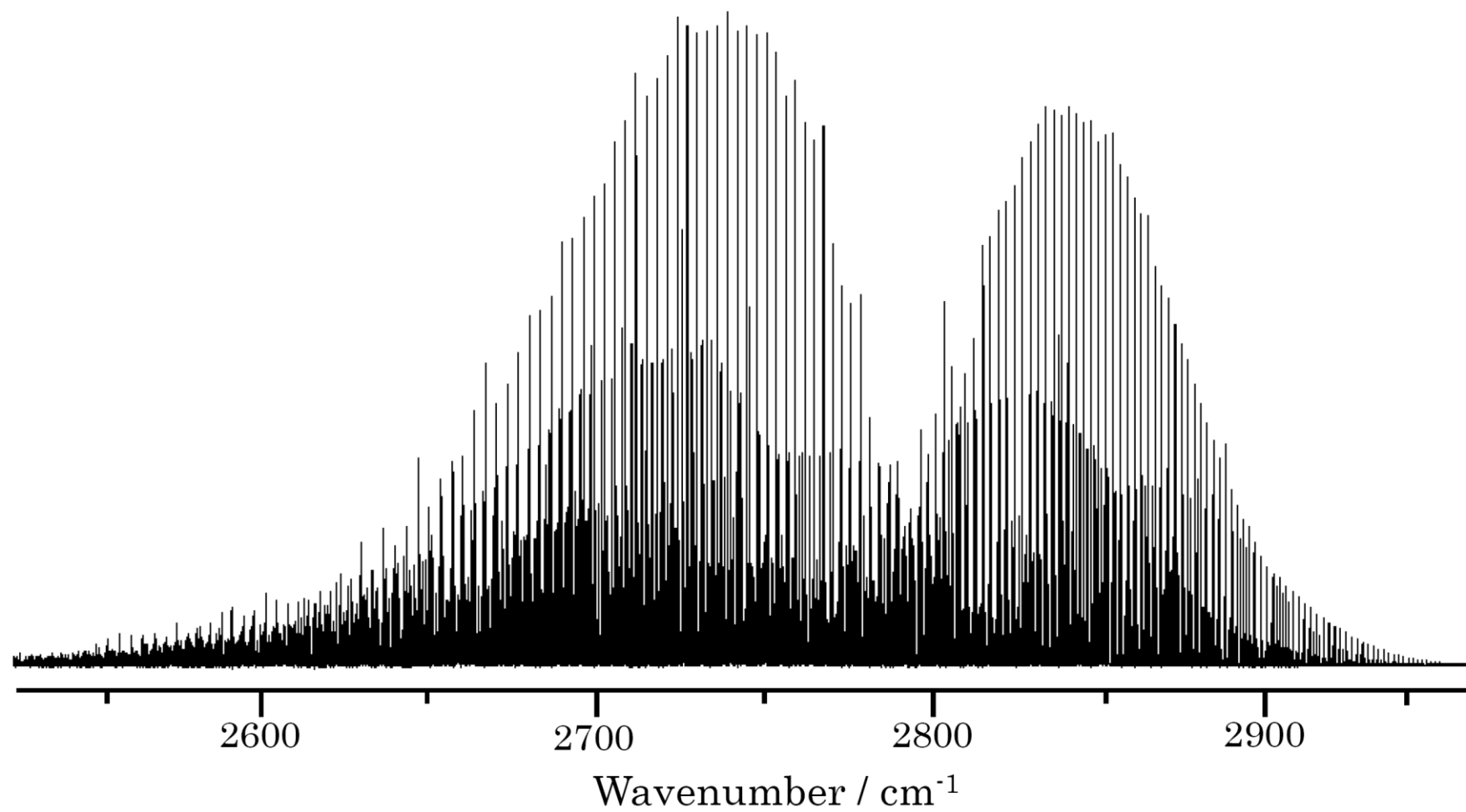


Figure 8.2: High resolution Fourier transform emission spectrum of HBO  $v_1$  fundemantal band.

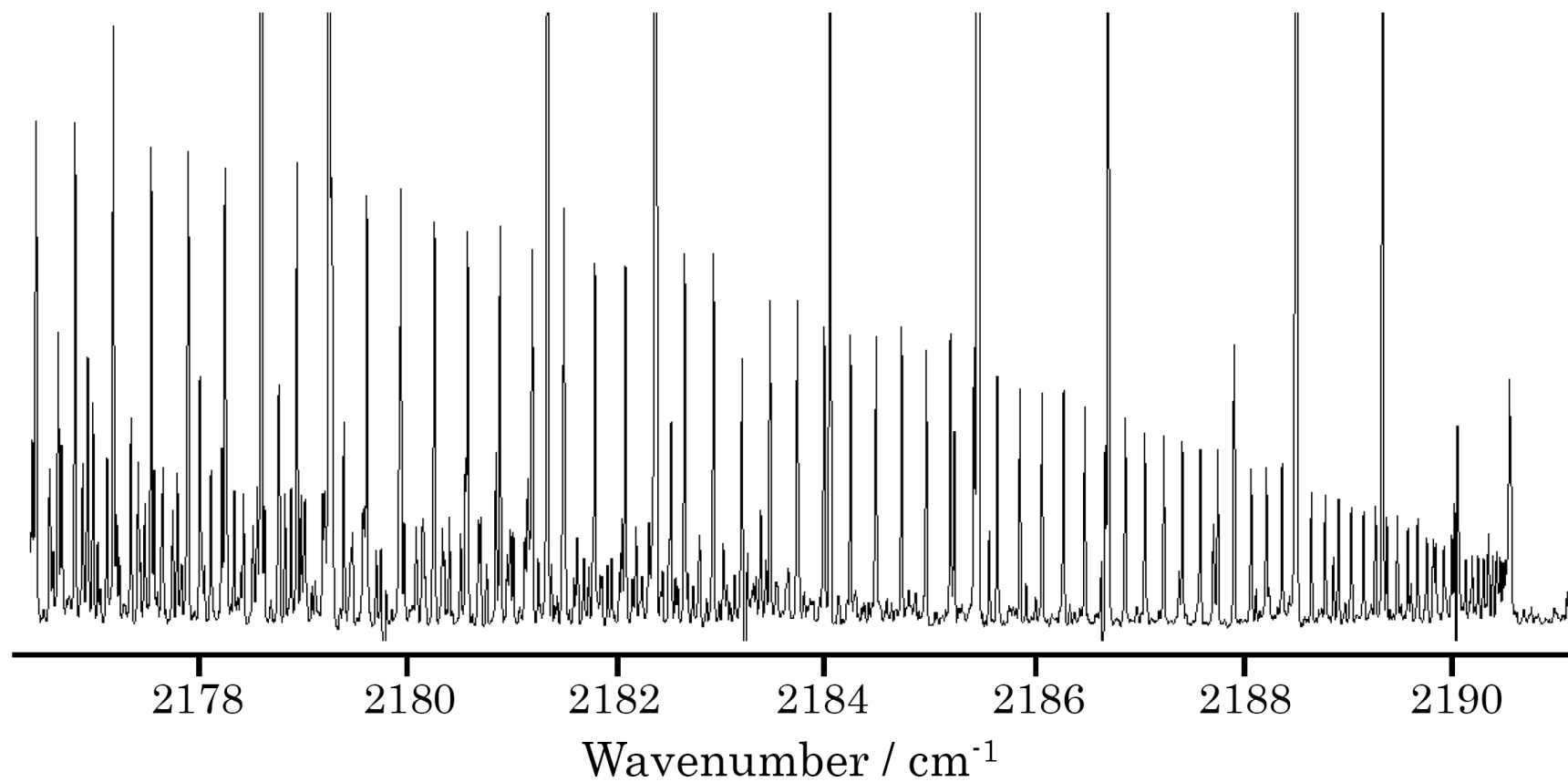


Figure 8.3: An extended portion of the high resolution Fourier transform emission spectrum of FBO  $\nu_1$  fundamental band.

## 8.1.2 Pure boron clusters

In recent years, there has been an increasing interest in boron-containing molecules due to their possible applications in hydrogen storage, semi-conducting materials and boron nano-technology. Among all these systems, pure boron clusters have possibly been the most controversial topic in the past 10 years<sup>163-171</sup>. Early studies mainly focused on their geometries. Recent theoretical studies have shown an interesting feature for these boron clusters: they are all planar or quasi-planar structures, rather than 3-D structures like the famous boranes. The successful synthesis of B<sub>9</sub> and B<sub>16</sub> in L.S. Wang's group using laser ablation and photoelectron spectroscopy also confirmed the planar geometries<sup>164</sup>.

Aromaticity and multi-aromaticity were suggested as the explanation of the planarity and high stability of boron clusters<sup>169</sup>. The concept of aromaticity was originally introduced in organic chemistry. In 2001, it was extended to all-metal clusters and later main-group element and transition metal clusters. As a Light element with a simple electronic structure, boron is still surprising us with an unusual chemical bonding and other interesting phenomena. Thus, understanding the structure and properties of boron clusters is fundamentally important. However, there has been very little quantitative experimental study of boron clusters. One of the possible reasons for this is the difficulty in synthesizing the molecules.

A microwave plasma source has proved to be an effective ways of making these special gas-phase molecules. The microwave discharge experimental setup in our lab has been successful in synthesizing the small carbon clusters such as C<sub>2</sub> and C<sub>3</sub> from isopropanol<sup>172</sup>. Our goal is to synthesis small boron clusters such as B<sub>3</sub> using diborane mixed in an argon carrier gas and record its infrared spectra at high resolution.

## 8.2 List lists of hydrogen halides

Hydrogen halides (namely HBr, HCl, HF, HI and their isotopologues) are present in a variety of planetary and stellar atmospheres. In order to correctly interpret and model the spectra of hydrogen halides one needs to have an accurate set of reference spectral parameters for these species. Such lists already exist in the HITRAN database, however their use is limited to temperatures that do not exceed 300 K, whereas stellar and some planetary atmospheres can reach thousands of Kelvin. Moreover the amount of isotopic species of these molecules in HITRAN is also limited (for example the deuterated species are not given).

In Chapter 5, a new method of constructing ro-vibrational dipole moment functions has been derived and applied to HCl. The methodology developed in this work will be applied to recalculate intensities of all hydrogen halides in the HITRAN database. The resulting line lists will be indispensable for interpretation of planetary and stellar atmospheres.

# Appendix A

## Line lists for HBS

Table A1: Line list (in  $\text{cm}^{-1}$ ) of  $\nu_3$  fundamental of  $\text{H}^{11}\text{B}^{32}\text{S}$ .

$J'$	$J''$	Observed	Obs.-Calc.	Uncertainty
1	0	1173.6358	0.0003	0.0005
2	1	1174.8952	0.0003	0.0005
3	2	1176.1441	-0.0033	1000
4	3	1177.3929	-0.0001	0.0005
5	4	1178.6319	0.0002	0.0005
6	5	1179.8629	-0.0005	0.001
7	6	1181.0885	0.0003	0.0005
8	7	1182.3063	0.0003	0.0005
9	8	1183.5170	0.0001	0.0005
10	9	1184.7206	-0.0001	0.0005
11	10	1185.9176	0.0001	0.0005
12	11	1187.1073	0.0000	0.0005
13	12	1188.2900	0.0001	0.0005
14	13	1189.4657	0.0001	0.0005
15	14	1190.6342	0.0001	0.0005
16	15	1191.7955	0.0000	0.0005
17	16	1192.9499	0.0001	0.0005
18	17	1194.0969	0.0000	0.0005
19	18	1195.2368	-0.0001	0.0005
20	19	1196.3696	0.0000	0.0005
21	20	1197.4952	0.0001	0.0005
22	21	1198.6135	0.0000	0.0005
23	22	1199.7245	-0.0001	0.0005
24	23	1200.8281	-0.0002	0.0005
25	24	1201.9248	-0.0001	0.0005
26	25	1203.0142	0.0002	0.0005
27	26	1204.0959	0.0000	0.0005
28	27	1205.1705	0.0001	0.0005
29	28	1206.2376	0.0000	0.0005
30	29	1207.2973	-0.0001	0.0005
31	30	1208.3500	0.0002	0.0005
32	31	1209.3948	0.0001	0.0005
33	32	1210.4321	-0.0001	0.0005
34	33	1211.4623	0.0000	0.0005

---

35	34	1212.4847	-0.0002	0.0005
36	35	1213.4998	-0.0001	0.0005
37	36	1214.5073	-0.0001	0.0005
38	37	1215.5074	0.0000	0.0005
39	38	1216.4999	0.0000	0.0005
40	39	1217.4846	-0.0001	0.0005
41	40	1218.4622	0.0002	0.0005
42	41	1219.4314	-0.0002	0.0005
43	42	1220.3934	-0.0001	0.0005
44	43	1221.3477	-0.0001	0.0005
45	44	1222.2946	0.0001	0.0005
46	45	1223.2336	0.0002	0.0005
47	46	1224.1646	0.0001	0.0005
48	47	1225.0883	0.0002	0.0005
49	48	1226.0037	-0.0001	0.0005
50	49	1226.9116	0.0000	0.0005
51	50	1227.8116	-0.0002	0.0005
52	51	1228.7039	-0.0002	0.0005
53	52	1229.5886	0.0001	0.0005
54	53	1230.4650	0.0000	0.0005
55	54	1231.3336	-0.0001	0.0005
56	55	1232.1943	-0.0002	0.0005
57	56	1233.0477	0.0004	0.0005
58	57	1233.8921	-0.0001	0.0005
59	58	1234.7296	0.0005	0.0005
60	59	1235.5579	-0.0002	0.0005
61	60	1236.3791	0.0001	0.0005
62	61	1237.1911	-0.0008	0.002
63	62	1237.9966	-0.0001	0.0005
64	63	1238.7937	0.0002	0.0005
65	64	1239.5825	0.0003	0.0005
66	65	1240.3631	0.0003	0.0005
67	66	1241.1352	0.0000	0.0005
68	67	1241.8993	-0.0003	0.0005
69	68	1242.6558	0.0001	0.0005
70	69	1243.4037	0.0001	0.0005
71	70	1244.1439	0.0006	0.002
72	71	1244.8747	-0.0001	0.0005
73	72	1245.5979	-0.0001	0.0005
74	73	1246.3124	-0.0006	0.002
75	74	1247.0197	0.0000	0.0005
0	1	1171.0959	-0.0003	0.0005
1	2	1169.8169	0.0006	0.002
2	3	1168.5292	-0.0004	0.0005
3	4	1167.2361	0.0000	0.0005

---

---

4	5	1165.9361	0.0003	0.0005
5	6	1164.6285	-0.0003	0.0005
6	7	1163.3146	-0.0004	0.0005
7	8	1161.9944	-0.0001	0.0005
8	9	1160.6673	0.0001	0.0005
9	10	1159.3334	0.0000	0.0005
10	11	1157.9927	-0.0001	0.0005
11	12	1156.6456	0.0000	0.0005
12	13	1155.2918	0.0001	0.0005
13	14	1153.9312	0.0000	0.0005
14	15	1152.5641	0.0000	0.0005
15	16	1151.1904	0.0000	0.0005
16	17	1149.8102	0.0001	0.0005
17	18	1148.4233	-0.0001	0.0005
18	19	1147.0300	0.0000	0.0005
19	20	1145.6300	-0.0001	0.0005
20	21	1144.2236	0.0000	0.0005
21	22	1142.8106	-0.0001	0.0005
22	23	1141.3913	0.0000	0.0005
23	24	1139.9654	-0.0001	0.0005
24	25	1138.5333	0.0000	0.0005
25	26	1137.0945	-0.0001	0.0005
26	27	1135.6497	0.0003	0.0005
27	28	1134.1979	0.0000	0.0005
28	29	1132.7399	-0.0001	0.0005
29	30	1131.2753	-0.0004	0.0005
30	31	1129.8051	0.0000	0.0005
31	32	1128.3280	-0.0001	0.0005
32	33	1126.8449	0.0001	0.0005
33	34	1125.3549	-0.0003	0.0005
34	35	1123.8593	0.0000	0.0005
35	36	1122.3571	0.0000	0.0005
36	37	1120.8487	0.0000	0.0005
37	38	1119.3340	0.0000	0.0005
38	39	1117.8129	-0.0002	0.0005
39	40	1116.2859	-0.0001	0.0005
40	41	1114.7527	0.0000	0.0005
41	42	1113.2132	0.0000	0.0005
42	43	1111.6676	0.0002	0.0005
43	44	1110.1153	-0.0003	0.0005
44	45	1108.5575	0.0000	0.0005
45	46	1106.9929	-0.0006	0.002
46	47	1105.4234	0.0002	0.0005
47	48	1103.8470	0.0002	0.0005
48	49	1102.2644	0.0000	0.0005

---

49	50	1100.6756	-0.0003	0.0005
50	51	1099.0812	-0.0001	0.0005
51	52	1097.4807	0.0000	0.0005
52	53	1095.8741	0.0001	0.0005
53	54	1094.2608	-0.0007	0.002
54	55	1092.6427	-0.0001	0.0005
55	56	1091.0181	0.0000	0.0005
56	57	1089.3877	0.0001	0.0005
57	58	1087.7510	0.0001	0.0005
58	59	1086.1088	0.0004	0.0005
59	60	1084.4599	-0.0001	0.0005
60	61	1082.8053	-0.0003	0.0005
61	62	1081.1455	0.0001	0.0005
62	63	1079.4793	0.0001	0.0005
63	64	1077.8073	0.0001	0.0005
64	65	1076.1291	-0.0001	0.0005
65	66	1074.4454	-0.0001	0.0005
66	67	1072.7560	0.0001	0.0005
67	68	1071.0606	0.0001	0.0005
68	69	1069.3597	0.0003	0.0005
69	70	1067.6531	0.0007	0.002
70	71	1065.9395	-0.0002	0.0005
71	72	1064.2204	-0.0007	0.002
72	73	1062.4971	0.0003	0.0005
73	74	1060.7669	0.0001	0.0005
74	75	1059.0315	0.0004	0.0005
75	76	1057.2901	0.0004	0.002
76	77	1055.5430	0.0004	0.002
77	78	1053.7894	-0.0004	0.0005
78	79	1052.0305	-0.0008	0.002
79	80	1050.2668	-0.0005	0.0005
80	81	1048.4978	0.0002	0.0005
81	82	1046.7213	-0.0009	0.002

Table A2: Line list (in  $\text{cm}^{-1}$ ) of  $\nu_1$  fundamental of  $\text{H}^{11}\text{B}^{32}\text{S}$ .

$J'$	$J''$	Observed	Obs.-Calc.	Uncertainty
87	88	2603.4163	-0.0005	0.005
86	87	2605.1260	0.0043	0.02
85	86	2606.8236	0.0007	0.004
84	85	2608.5191	-0.0010	0.004
83	84	2610.2137	0.0001	0.004
82	83	2611.9035	0.0004	0.004
81	82	2613.5897	0.0009	0.004
80	81	2615.2682	-0.0022	0.004

---

79	80	2616.9481	-0.0001	0.004
78	79	2618.6168	-0.0050	0.02
77	78	2620.2951	0.0036	0.007
76	77	2621.9569	-0.0001	0.004
75	76	2623.6199	0.0015	0.004
74	75	2625.2759	0.0002	0.004
73	74	2626.9297	0.0009	0.004
72	73	2628.5744	-0.0034	0.01
71	72	2630.2237	0.0013	0.004
70	71	2631.8612	-0.0017	0.005
69	70	2633.4961	-0.0030	0.004
68	69	2635.1312	0.0002	0.004
67	68	2636.7572	-0.0012	0.004
66	67	2638.3827	0.0011	0.004
65	66	2640.0008	0.0006	0.004
64	65	2641.6142	-0.0004	0.004
63	64	2643.2199	-0.0045	0.05
62	63	2644.8302	0.0005	0.004
61	62	2646.4290	-0.0015	0.004
60	61	2648.0256	-0.0012	0.004
59	60	2649.6177	-0.0008	0.002
58	59	2651.2055	-0.0001	0.002
57	58	2652.7874	-0.0006	0.002
56	57	2654.3653	-0.0006	0.002
55	56	2655.9393	0.0003	0.002
54	55	2657.5039	-0.0035	0.006
53	54	2659.0711	-0.0001	0.002
52	53	2660.6321	0.0020	0.004
51	52	2662.1841	-0.0001	0.002
50	51	2663.7292	-0.0043	0.007
49	50	2665.2784	0.0004	0.002
48	49	2666.8162	-0.0014	0.002
47	48	2668.3532	0.0008	0.002
46	47	2669.8823	0.0001	0.002
45	46	2671.4058	-0.0013	0.002
44	45	2672.9266	-0.0004	0.002
43	44	2674.4424	0.0005	0.002
42	43	2675.9522	0.0005	0.002
41	42	2677.4569	0.0003	0.002
40	41	2678.9554	-0.0010	0.002
39	40	2680.4532	0.0021	0.005
38	39	2681.9398	-0.0009	0.002
37	38	2683.4249	-0.0002	0.002
36	37	2684.9041	-0.0004	0.002
35	36	2686.3820	0.0035	0.007

---

---

34	35	2687.8481	0.0007	0.002
33	34	2689.3100	-0.0010	0.002
32	33	2690.7703	0.0008	0.002
31	32	2692.2226	0.0000	0.002
30	31	2693.6709	0.0005	0.002
29	30	2695.1129	-0.0001	0.002
28	29	2696.5506	0.0006	0.002
27	28	2697.9801	-0.0017	0.002
26	27	2699.4059	-0.0023	0.005
25	26	2700.8297	0.0005	0.002
24	25	2702.2432	-0.0016	0.002
23	24	2703.6548	-0.0001	0.002
22	23	2705.0603	0.0008	0.002
21	22	2706.4594	0.0009	0.002
20	21	2707.8518	-0.0003	0.002
19	20	2709.2409	0.0007	0.002
18	19	2710.6235	0.0008	0.002
17	18	2712.0001	0.0005	0.002
16	17	2713.3707	-0.0002	0.002
15	16	2714.7366	0.0000	0.002
14	15	2716.0964	-0.0002	0.002
13	14	2717.4451	-0.0059	10000
12	13	2718.7997	0.0001	0.002
11	12	2720.1423	-0.0004	0.002
10	11	2721.4798	-0.0001	0.002
9	10	2722.8120	0.0006	0.002
8	9	2724.1363	-0.0009	0.002
7	8	2725.4563	-0.0008	0.002
6	7	2726.7719	0.0005	0.002
5	6	2728.0810	0.0013	0.002
4	5	2729.3822	0.0000	0.002
3	4	2730.6815	0.0025	0.004
2	3	2731.9697	-0.0001	0.002
1	0	2737.0733	-0.0006	0.002
3	2	2739.5871	-0.0032	0.007
5	4	2742.0837	0.0010	0.002
6	5	2743.3189	-0.0009	0.002
7	6	2744.5510	0.0001	0.002
8	7	2745.7748	-0.0012	0.002
9	8	2746.9952	0.0003	0.002
10	9	2748.2080	0.0002	0.002
11	10	2749.4152	0.0006	0.002
12	11	2750.6166	0.0013	0.002
13	12	2751.8092	-0.0006	0.002
14	13	2752.9982	0.0001	0.002

---

---

15	14	2754.1798	-0.0005	0.002
16	15	2755.3556	-0.0007	0.002
17	16	2756.5264	0.0003	0.002
18	17	2757.6896	0.0000	0.002
19	18	2758.8451	-0.0020	0.002
20	19	2759.9980	-0.0002	0.002
21	20	2761.1428	-0.0001	0.002
22	21	2762.2808	-0.0008	0.002
23	22	2763.4135	-0.0004	0.002
24	23	2764.5386	-0.0013	0.002
25	24	2765.6596	0.0001	0.002
26	25	2766.7727	-0.0001	0.002
27	26	2767.8800	0.0001	0.002
28	27	2768.9812	0.0007	0.002
29	28	2770.0753	0.0004	0.002
30	29	2771.1632	0.0005	0.002
31	30	2772.2449	0.0007	0.002
32	31	2773.3202	0.0008	0.002
33	32	2774.3877	-0.0004	0.002
34	33	2775.4509	0.0005	0.002
35	34	2776.5065	0.0003	0.002
36	35	2777.5561	0.0004	0.002
37	36	2778.5990	0.0005	0.002
38	37	2779.6353	0.0003	0.002
39	38	2780.6656	0.0006	0.002
41	40	2782.7002	-0.0052	10000
42	41	2783.7168	0.0009	0.002
43	42	2784.7200	0.0001	0.002
44	43	2785.7173	0.0000	0.002
45	44	2786.7078	-0.0003	0.002
46	45	2787.6923	-0.0001	0.002
47	46	2788.6705	0.0004	0.002
48	47	2789.6417	0.0005	0.002
49	48	2790.6053	-0.0005	0.002
50	49	2791.5639	0.0000	0.002
51	50	2792.5152	-0.0001	0.002
52	51	2793.4600	0.0000	0.002
53	52	2794.3972	-0.0009	0.002
54	53	2795.3300	0.0003	0.002
55	54	2796.2549	0.0003	0.002
56	55	2797.1746	0.0018	0.002
57	56	2798.0834	-0.0010	0.002
58	57	2798.9890	-0.0004	0.002
59	58	2799.8879	0.0002	0.002
60	59	2800.7774	-0.0019	0.004

---

61	60	2801.6630	-0.0012	0.002
62	61	2802.5424	0.0000	0.002
63	62	2803.4128	-0.0011	0.002
64	63	2804.2789	0.0001	0.002
65	64	2805.1383	0.0014	0.002
66	65	2805.9881	-0.0003	0.002
67	66	2806.8324	-0.0007	0.002
68	67	2807.6753	0.0043	0.007
69	68	2808.5024	0.0000	0.002
70	69	2809.3275	0.0006	0.002
71	70	2810.1450	0.0004	0.002
72	71	2810.9557	-0.0001	0.002
73	72	2811.7601	0.0000	0.002
74	73	2812.5614	0.0038	0.006
75	74	2813.3484	0.0000	0.002
76	75	2814.1326	0.0002	0.002
77	76	2814.9124	0.0028	0.004
78	77	2815.6796	-0.0006	0.002
79	78	2816.4446	0.0007	0.005
80	79	2817.2061	0.0052	0.02
81	80	2817.9483	-0.0027	0.01
82	81	2818.6947	0.0003	0.002
83	82	2819.4343	0.0032	0.02
84	83	2820.1618	0.0009	0.002
85	84	2820.8831	-0.0009	0.002
86	85	2821.6000	-0.0003	0.002

Table A3: Line list (in  $\text{cm}^{-1}$ ) of  $\nu_3$  fundamental of  $\text{H}^{10}\text{B}^{32}\text{S}$ .

$J'$	$J''$	Observed	Obs.-Calc.	Uncertainty
2	1	1209.7273	0.0023	0.005
3	2	1211.0463	0.0035	0.005
4	3	1212.3533	0.0000	0.001
5	4	1213.6566	0.0002	0.001
6	5	1214.9515	-0.0007	0.001
7	6	1216.2404	-0.0002	0.001
8	7	1217.5204	-0.0012	0.002
9	8	1218.7938	-0.0014	0.002
10	9	1220.0615	0.0001	0.001
11	10	1221.3198	-0.0003	0.001
12	11	1222.5710	-0.0003	0.001
13	12	1223.8162	0.0012	0.002
14	13	1225.0515	0.0003	0.001
15	14	1226.2787	-0.0012	0.002
16	15	1227.5009	-0.0002	0.001

---

17	16	1228.7154	0.0008	0.001
18	17	1229.9205	0.0000	0.001
19	18	1231.1188	-0.0001	0.001
20	19	1232.3098	0.0003	0.001
21	20	1233.4925	0.0000	0.001
22	21	1234.6661	-0.0017	0.005
23	22	1235.8355	0.0002	0.001
24	23	1236.9951	-0.0001	0.001
25	24	1238.1471	-0.0002	0.001
26	25	1239.2919	0.0003	0.001
27	26	1240.4280	-0.0002	0.001
28	27	1241.5567	-0.0001	0.001
29	28	1242.6777	0.0001	0.001
30	29	1243.7907	0.0001	0.001
31	30	1244.8958	0.0001	0.001
32	31	1245.9927	-0.0001	0.001
33	32	1247.0822	0.0001	0.001
34	33	1248.1633	0.0000	0.001
35	34	1249.2365	0.0000	0.001
36	35	1250.3016	-0.0001	0.001
37	36	1251.3588	-0.0002	0.001
38	37	1252.4082	0.0001	0.001
39	38	1253.4493	0.0002	0.001
40	39	1254.4824	0.0002	0.001
41	40	1255.5067	-0.0003	0.001
42	41	1256.5234	-0.0003	0.001
43	42	1257.5322	0.0000	0.001
44	43	1258.5323	-0.0002	0.001
45	44	1259.5254	0.0008	0.001
46	45	1260.5087	0.0002	0.001
47	46	1261.4842	0.0003	0.001
48	47	1262.4514	0.0002	0.001
49	48	1263.4101	-0.0001	0.001
50	49	1264.3605	-0.0003	0.001
51	50	1265.3031	0.0001	0.001
52	51	1266.2370	0.0002	0.001
53	52	1267.1622	-0.0001	0.001
54	53	1268.0795	0.0002	0.001
55	54	1268.9875	-0.0004	0.001
56	55	1269.8878	-0.0001	0.001
57	56	1270.7793	-0.0001	0.001
58	57	1271.6624	0.0000	0.001
59	58	1272.5369	0.0000	0.001
60	59	1273.4027	0.0000	0.001
61	60	1274.2606	0.0007	0.001

---

---

62	61	1275.1086	0.0001	0.001
63	62	1275.9486	0.0001	0.001
2	3	1203.0290	0.0020	0.005
3	4	1201.6650	-0.0008	0.001
4	5	1200.2971	-0.0003	0.001
5	6	1198.9211	-0.0007	0.001
6	7	1197.5391	0.0001	0.001
7	8	1196.1493	0.0001	0.001
8	9	1194.7523	0.0001	0.001
9	10	1193.3492	0.0010	0.002
10	11	1191.9367	-0.0003	0.001
11	12	1190.5197	0.0009	0.001
12	13	1189.0942	0.0005	0.001
13	14	1187.6612	-0.0002	0.001
14	15	1186.2218	-0.0004	0.001
15	16	1184.7762	0.0002	0.001
16	17	1183.3241	0.0013	0.002
17	18	1181.8629	0.0002	0.001
18	19	1180.3956	0.0000	0.001
19	20	1178.9215	-0.0002	0.001
20	21	1177.4408	0.0000	0.001
21	22	1175.9532	0.0001	0.001
22	23	1174.4586	0.0002	0.001
23	24	1172.9567	-0.0004	0.001
24	25	1171.4486	-0.0001	0.001
25	26	1169.9339	0.0003	0.001
26	27	1168.4117	-0.0001	0.001
27	28	1166.8824	-0.0007	0.001
28	29	1165.3475	-0.0001	0.001
29	30	1163.8054	0.0000	0.001
30	31	1162.2564	0.0000	0.001
31	32	1160.7007	-0.0001	0.001
32	33	1159.1378	-0.0006	0.001
33	34	1157.5692	-0.0001	0.001
34	35	1155.9928	-0.0008	0.001
35	36	1154.4113	0.0002	0.001
36	37	1152.8222	0.0001	0.001
37	38	1151.2262	-0.0002	0.001
38	39	1149.6237	-0.0004	0.001
39	40	1148.0158	0.0006	0.001
40	41	1146.3997	0.0000	0.001
41	42	1144.7782	0.0005	0.001
42	43	1143.1494	0.0004	0.001
43	44	1141.5137	-0.0001	0.001
44	45	1139.8722	0.0001	0.001

---

45	46	1138.2242	0.0003	0.001
46	47	1136.5691	-0.0001	0.001
47	48	1134.9084	0.0005	0.001
48	49	1133.2399	-0.0004	0.001
49	50	1131.5655	-0.0006	0.001
50	51	1129.8859	0.0004	0.001
51	52	1128.1984	-0.0001	0.001
52	53	1126.5053	0.0002	0.001
53	54	1124.8055	0.0002	0.001
54	55	1123.0989	-0.0001	0.001
55	56	1121.3881	0.0017	0.005
56	57	1119.6684	0.0009	0.001
57	58	1117.9425	0.0003	0.001
58	59	1116.2107	0.0002	0.001
59	60	1114.4736	0.0010	0.002
60	61	1112.7284	0.0001	0.001
61	62	1110.9770	-0.0008	0.001
62	63	1109.2176	-0.0034	0.01
63	64	1107.4589	0.0010	0.002
64	65	1105.6880	-0.0007	0.001
65	66	1103.9139	0.0008	0.001
66	67	1102.1305	-0.0009	0.001
67	68	1100.3421	-0.0013	0.002

Table A4: Line list (in  $\text{cm}^{-1}$ ) of  $\nu_1$  fundamental of  $\text{H}^{10}\text{B}^{32}\text{S}$ .

$J'$	$J''$	Observed	Obs.-Calc.	Uncertainty
2	1	2754.1015	-0.0005	0.005
3	2	2755.4216	0.0003	0.005
4	3	2756.7263	-0.0074	0.02
5	4	2758.0360	-0.0032	0.005
6	5	2759.3326	-0.0053	0.02
7	6	2760.6310	0.0012	0.005
8	7	2761.9142	-0.0005	0.005
9	8	2763.1936	0.0009	0.005
10	9	2764.4663	0.0025	0.005
11	10	2765.7282	0.0003	0.005
12	11	2766.9828	-0.0023	0.005
13	12	2768.2342	-0.0010	0.005
14	13	2769.4774	-0.0010	0.005
15	14	2770.7124	-0.0022	0.005
16	15	2771.9450	0.0014	0.005
17	16	2773.1647	-0.0010	0.005
18	17	2774.3877	0.0069	0.02
19	18	2775.5923	0.0036	0.005

---

20	19	2776.7894	-0.0001	0.005
21	20	2777.9828	-0.0004	0.005
22	21	2779.1673	-0.0025	0.005
23	22	2780.3476	-0.0018	0.005
24	23	2781.5209	-0.0007	0.005
25	24	2782.7002	0.0134	90.005
26	25	2783.8462	0.0015	0.005
27	26	2784.9941	-0.0015	0.005
28	27	2786.1403	0.0012	0.005
29	28	2787.2773	0.0018	0.005
30	29	2788.4043	-0.0002	0.005
31	30	2789.5221	-0.0043	0.005
32	31	2790.6425	0.0015	0.005
33	32	2791.7504	0.0020	0.005
34	33	2792.8486	0.0003	0.005
35	34	2793.9410	-0.0001	0.005
36	35	2795.0226	-0.0040	0.005
37	36	2796.1032	-0.0014	0.005
38	37	2797.1746	-0.0008	0.005
39	38	2798.2388	0.0000	0.005
40	39	2799.2956	0.0007	0.005
41	40	2800.3454	0.0018	0.005
42	41	2801.3850	0.0001	0.005
43	42	2802.4184	-0.0004	0.005
44	43	2803.4458	0.0005	0.005
45	44	2804.4647	0.0002	0.005
46	45	2805.4707	-0.0054	0.02
47	46	2806.4800	-0.0004	0.005
48	47	2807.4769	-0.0003	0.005
49	48	2808.4651	-0.0013	0.005
50	49	2809.4493	0.0010	0.005
51	50	2810.4238	0.0012	0.005
52	51	2811.3901	0.0006	0.005
53	52	2812.3482	-0.0007	0.005
54	53	2813.3002	-0.0005	0.005
55	54	2814.2433	-0.0018	0.005
56	55	2815.1823	0.0005	0.005
57	56	2816.1105	-0.0006	0.005
58	57	2817.0305	-0.0023	0.005
59	58	2817.9483	0.0014	0.005
60	59	2818.8518	-0.0018	0.005
61	60	2819.7516	-0.0009	0.005
62	61	2820.6422	-0.0017	0.005
63	62	2821.5279	0.0003	0.005
64	63	2822.4065	0.0027	0.005

---

---

65	64	2823.2717	-0.0006	0.005
66	65	2824.1303	-0.0028	0.005
67	66	2824.9863	-0.0001	0.005
68	67	2825.8324	0.0005	0.005
69	68	2826.6711	0.0013	0.005
70	69	2827.5006	0.0006	0.005
4	5	2744.6745	-0.0032	0.005
5	6	2743.3189	0.0143	90.005
6	7	2741.9297	0.0049	0.005
7	8	2740.5304	-0.0079	0.02
8	9	2739.1561	0.0108	90.005
9	10	2737.7450	-0.0007	0.005
10	11	2736.3470	0.0076	0.02
11	12	2734.9255	-0.0012	0.005
12	13	2733.5060	-0.0014	0.005
13	14	2732.0819	0.0003	0.005
14	15	2730.6431	-0.0062	0.02
15	16	2729.2098	-0.0008	0.005
16	17	2727.7648	-0.0006	0.005
17	18	2726.3142	0.0003	0.005
18	19	2724.8555	-0.0004	0.005
19	20	2723.3912	-0.0004	0.005
20	21	2721.9222	0.0013	0.005
21	22	2720.4452	0.0013	0.005
22	23	2718.9655	0.0050	0.02
23	24	2717.4793	0.0083	0.02
24	25	2715.9840	0.0089	0.02
25	26	2714.4735	0.0004	0.005
26	27	2712.9650	0.0001	0.005
27	28	2711.4513	0.0008	0.005
28	29	2709.9313	0.0014	0.005
29	30	2708.4033	0.0001	0.005
30	31	2706.8705	0.0001	0.005
31	32	2705.3358	0.0043	0.005
32	33	2703.7875	0.0009	0.005
33	34	2702.2432	0.0075	0.02
34	35	2700.6785	-0.0002	0.005
35	36	2699.1138	-0.0020	0.005
36	37	2697.5462	-0.0007	0.005
37	38	2695.9717	-0.0004	0.005
38	39	2694.3948	0.0034	0.005
39	40	2692.8056	0.0007	0.005
40	41	2691.2156	0.0032	0.005
41	42	2689.6251	0.0109	90.005
42	43	2688.0114	0.0011	0.005

---

---

44	45	2684.7825	-0.0025	0.005
45	46	2683.1650	0.0012	0.005
46	47	2681.5353	-0.0015	0.005
47	48	2679.9040	-0.0003	0.005
48	49	2678.2697	0.0035	0.005
49	50	2676.6228	0.0004	0.005
50	51	2674.9778	0.0048	0.02
51	52	2673.3118	-0.0064	0.02
52	53	2671.6547	-0.0030	0.02
53	54	2669.9982	0.0064	0.02
54	55	2668.3266	0.0061	0.02
55	56	2666.6431	-0.0007	0.02
56	57	2664.9524	-0.0091	0.02
57	58	2663.2806	0.0067	0.02
58	59	2661.5783	-0.0027	0.02
59	60	2659.8739	-0.0089	0.02
60	61	2658.1766	-0.0026	0.005
61	62	2656.4700	-0.0003	0.005
62	63	2654.7598	0.0035	0.005
63	64	2653.0368	-0.0002	0.005
64	65	2651.2974	-0.0152	90.005
65	66	2649.5825	-0.0004	0.005
66	67	2647.8457	-0.0024	0.005
67	68	2646.1053	-0.0030	0.005
68	69	2644.3770	0.0136	90.005
69	70	2642.6140	0.0006	0.005
70	71	2640.8533	-0.0051	0.02
71	72	2639.1032	0.0049	0.005
72	73	2637.3439	0.0106	0.05

---

## Appendix B

# Analytical expressions for the eigenstates of a ${}^2\Pi$ state

In the following derivations, all the terms and constants have their usual meaning <sup>124</sup>. In order to determine the eigenstates for a  ${}^2\Pi$  state intermediate between Hund's coupling cases (a) and (b), we use a simple version of the  $\mathbf{N}^2$  Hamiltonian incorporating only the following rotational and spin-orbit terms

$$\mathcal{H}_{\text{rot}} = B\mathbf{N}^2 = B(\mathbf{J} - \mathbf{S})^2$$

Eq. C 1

$$\mathcal{H}_{\text{SO}} = AL_zS_z$$

Eq. C 2

There are four case-(a) parity basis functions associated with a  ${}^2\Pi$  state:

$$|{}^2\Pi_{3/2} J M \pm\rangle = \frac{1}{\sqrt{2}} \left\{ \left| \Lambda = 1; S = \frac{1}{2}, \Sigma = \frac{1}{2}; J, \Omega = \frac{3}{2}, M \right\rangle \right. \\ \left. \pm (-1)^{J-1/2} \left| \Lambda = -1; S = \frac{1}{2}, \Sigma = -\frac{1}{2}; J, \Omega = -\frac{3}{2}, M \right\rangle \right\}$$

Eq. C 3

$$|{}^2\Pi_{1/2} J M \pm\rangle = \frac{1}{\sqrt{2}} \left\{ \left| \Lambda = 1; S = \frac{1}{2}, \Sigma = -\frac{1}{2}; J, \Omega = \frac{1}{2}, M \right\rangle \right. \\ \left. \pm (-1)^{J-1/2} \left| \Lambda = -1; S = \frac{1}{2}, \Sigma = \frac{1}{2}; J, \Omega = -\frac{1}{2}, M \right\rangle \right\}$$

Eq. C 4

Using these basis functions and the Hamilton terms in Eq.C3 and Eq. C4, the following matrix elements are obtained <sup>124</sup>:

Table C1. Matrix elements of  $\mathcal{H}_{\text{rot}} + \mathcal{H}_{\text{SO}}$  for a  ${}^2\Pi$  state.

$\mathcal{H}_{\text{rot}} + \mathcal{H}_{\text{SO}}$	$ {}^2\Pi_{3/2} J M \pm\rangle$	$ {}^2\Pi_{1/2} J M \pm\rangle$
$\langle {}^2\Pi_{3/2} J M \pm  $	$\frac{A}{2} + B \left[ \left( J + \frac{1}{2} \right)^2 - 1 \right]$	$-B \left[ \left( J + \frac{1}{2} \right)^2 - 1 \right]^{1/2}$
$\langle {}^2\Pi_{1/2} J M \pm  $	$-B \left[ \left( J + \frac{1}{2} \right)^2 - 1 \right]^{1/2}$	$-\frac{A}{2} + B \left[ \left( J + \frac{1}{2} \right)^2 + 1 \right]$

Note that the matrix elements are identical for each  $\pm$  parity block. Diagonalisation of the matrix in Table C1 provides the following eigenvalues (for  $J \geq 1.5$ ):

$$E(\pm) = B(J+1)^2 \pm \frac{1}{2} \left\{ (A-2B)^2 + 4B^2 \left[ \left( J + \frac{1}{2} \right)^2 - 1 \right] \right\}^{1/2} = B \left( J + \frac{1}{2} \right)^2 \pm \frac{1}{2} B X_J$$

Eq. C 5

$$\text{where } X_J = \left\{ (Y-2)^2 + 4 \left[ \left( J + \frac{1}{2} \right)^2 - 1 \right] \right\}^{1/2}, \quad Y = \frac{A}{B}$$

Note that the + and – signs in Eq. C5 refer to the upper (F<sub>2</sub>) and lower (F<sub>1</sub>) levels, respectively, and not to the parity. The associated eigenfunctions are:

$$|F_2 \pm\rangle = \alpha_J |^2\Pi_{3/2} J M \pm\rangle - \beta_J |^2\Pi_{1/2} J M \pm\rangle$$

Eq. C 6

$$|F_1 \pm\rangle = \beta_J |^2\Pi_{3/2} J M \pm\rangle + \alpha_J |^2\Pi_{1/2} J M \pm\rangle$$

Eq. C 7

where  $\alpha_J = \left[ \frac{X_J + (Y-2)}{2X_J} \right]^{\frac{1}{2}}$  and  $\beta_J = \left[ \frac{X_J - (Y-2)}{2X_J} \right]^{\frac{1}{2}}$

In the special case when  $J = 0.5$ , and assuming  $A > 0$ , the eigenvalue and eigenvector is given by

$$E(J = \frac{1}{2}) = -\frac{A}{2} + 2B$$

Eq. C 8

$$|F_1 \pm\rangle = |^2\Pi_{1/2} J M \pm\rangle$$

Eq. C 9

# List of references

1. Papoušek, D., ed. *Vibrational-Rotational Spectroscopy and Molecular Dynamics*. 1997, World Scientific Press.
2. Hargreaves, R. J., Hinkle, K. H., Bauschlicher, C. W., Wende, S., Seifahrt, A., and Bernath, P. F., *Astronomical Journal* **140**, 919 (2010).
3. Laurretta, D. S. and Lodders, K., *Earth and Planetary Science Letters* **146**, 315 (1997).
4. Yeh, C. L. and Kuo, K. K., *Progress in Energy and Combustion Science* **22**, 511 (1996).
5. Yuasa, S., Yoshida, T., Kawashima, M., and Isoda, H., *Combustion and Flame* **113**, 380 (1998).
6. Bernath, P. F., *Chemical Society Reviews* **25**, 111 (1996).
7. Bernath, P. F., *International Reviews in Physical Chemistry* **28**, 681 (2009).
8. Bernath, P. F., *Science* **254**, 665 (1991).
9. Bernath, P. F., *Annual Review of Physical Chemistry* **41**, 91 (1990).
10. Bernath, P. F., *Spectroscopy and Photochemistry of Polyatomic Alkaline Earth Containing Molecules*, in *Advances in Photochemistry 2007*, John Wiley & Sons, Inc. p. 1.
11. Jyrki Kauppinen, J. P., ed. *Fourier transforms in spectroscopy*. 2000, WILEY-VCH.
12. W.Demtröder, ed. *Laser Spectroscopy*. 1981, Springer-Verlag.
13. Lefebvre-Brion, H. and Field, R. W., eds. *The spectra and dynamics of diatomic molecules*. 2004, ELSEVIER ACADEMIC PRESS.
14. Fakioglu, E., Yürüm, Y. and Nejat Veziroğlu, T., *International Journal of Hydrogen Energy* **29**, 1371 (2004).
15. J.M. Martinez-Val, S. E., M. Piera and G. Velarde, , *Physics Letters A* **216**, 142 (1996).
16. He, S.-G., Sunahori, F. X. and Clouthier, D. J., *Journal of the American Chemical Society* **127**, 10814 (2005).

17. Cheesman, A., Smith, J. A., Ashfold, M. N. R., Langford, N., Wright, S., and Duxbury, G., *The Journal of Physical Chemistry A* **110**, 2821 (2006).
18. Bernath, P. F., *Int. Rev. Phys. Chem.* **28**, 681 (2009).
19. Krasnopolsky, V. A., *Icarus* **208**, 539 (2010).
20. Lary, D. J. and Aulov, O., *Journal of Geophysical Research (Atmospheres)* **113**, D15S04 (2008).
21. Mahieu, E., et al., *Geophysical Research Letters* **32**, (2005).
22. Miller, H. C., Mccord, J., Hager, G. D., Davis, S. J., Kessler, W. J., and Oakes, D. B., *Journal of Applied Physics* **84**, 3467 (1998).
23. Vasil'ev, S. V., Kuz'mina, M. A., Basiev, T. T., and Hager, G., *Quantum Electronics* **33**, 201 (2003).
24. Rothman, L. S., et al., *JQSRT* **110**, 533 (2009).
25. Rothman, L. S., Goldman, A., Gillis, J. R., Tipping, R. H., Brown, L. R., Margolis, J. S., Maki, A. G., and Young, L. D. G., *Appl. Opt.* **20**, 1323 (1981).
26. Li, G., Gordon, I. E., Le Roy, R. J., Hajigeorgiou, P. G., Coxon, J. A., Bernath, P. F., and Rothman, L. S., *Extensive line lists of hydrogen halides and their isotopologues based on the most accurate potential energy surfaces and dipole moment functions*, in *JQSRT2010*. p. in preparation.
27. Toth, R. A., Hunt, R. H. and Plyler, E. K., *J. Mol. Spectrosc.* **35**, 110 (1970).
28. Ogilvie, J. F., Rodwell, W. R. and Tipping, R. H., *J. Chem. Phys.* **73**, 5221 (1980).
29. Tipping, R. H. and Ogilvie, J. F., *J. Mol. Spectrosc.* **96**, 442 (1982).
30. Kobayashi, M. and Suzuki, I., *Journal of Molecular Spectroscopy* **116**, 422 (1986).
31. Ogilvie, J. F. and Lee, Y.-P., *Chem. Phys. Lett.* **159**, 239 (1989).
32. Kiriya, F., Rao, B. S. and Nangia, V. K., *Journal of Quantitative Spectroscopy and Radiative Transfer* **69**, 35 (2001).
33. Olmsted, C. M., *Astrophysical Journal* **27**, 66 (1908).
34. Eagle, A., *Astrophysical Journal* **30**, 231 (1909).

35. Kirkpatrick, J. D., *Annu. Rev. Astron. Astrophys.* **43**, 195 (2005).
36. Burrows, A., Hubbard, W. B., Lunine, J. I., and Liebert, J., *Reviews of Modern Physics* **73**, 719 (2001).
37. Lepine, S., Shara, M. M. and Rich, R. M., *Astrophysical Journal* **585**, L69 (2003).
38. Lepine, S., Rich, R. M. and Shara, M. M., *Astrophysical Journal* **591**, L49 (2003).
39. Burgasser, A. J., Cruz, K. L. and Kirkpatrick, J. D., *Astrophysical Journal* **657**, 494 (2007).
40. Stone, R. C., Monet, D. G., Monet, A. K. B., Walker, R. L., Ables, H. D., Bird, A. R., and Harris, F. H., *Astronomical Journal* **111**, 1721 (1996).
41. Tinney, C. G., *Monthly Notices of the Royal Astronomical Society* **281**, 644 (1996).
42. Mera, D., Chabrier, G. and Baraffe, I., *Astrophysical Journal* **459**, L87 (1996).
43. Weck, P. F., Stancil, P. C. and Kirby, K., *Journal of Chemical Physics* **118**, 9997 (2003).
44. Ram, R. S., Tereszchuk, K., Gordon, I. E., Walker, K. A., and Bernath, P. F., *Journal of Molecular Spectroscopy* **266**, 86 (2011).
45. Le Roy, R. J., *LEVEL 8.0, University of Waterloo Chemical Physics Research Report CP-663, see* <http://scienide2.uwaterloo.ca/~rleroy/level/>, 2007.
46. Western, C., M., *PGOPHER, a Program for Simulating Rotational Structure, C. M. Western, University of Bristol, http://pgopher.chm.bris.ac.uk*, 2010.
47. H.-J. Werner, P. J. K., G. Knizia, F. R. Manby, M. Schütz, P. Celani, T. Korona, R. Lindh, A. Mitrushenkov, G. Rauhut, K. R. Shamasundar, T. B. Adler, R. D. Amos, A. Bernhardsson, A. Berning, D. L. Cooper, M. J. O. Deegan, A. J. Dobbyn, F. Eckert, E. Goll, C. Hampel, A. Hesselmann, G. Hetzer, T. Hrenar, G. Jansen, C. Köppl, Y. Liu, A. W. Lloyd, R. A. Mata, A. J. May, S. J. McNicholas, W. Meyer, M. E. Mura, A. Nicklaß, D. P. O'Neill, P. Palmieri, K. Pflüger, R. Pitzer, M. Reiher, T. Shiozaki, H. Stoll, A. J. Stone, R. Tarroni, T. Thorsteinsson, M. Wang, A. Wolf . , *MOLPRO, version 2010.1, a package of ab initio programs*, 2010, Cardiff, UK.

48. Bernath, P. F., ed. *Spectra of Atoms and Molecules*. Second Edition ed. 2005, Oxford University Press.
49. Le Roy, R. J., *RKR1 2.0*, University of Waterloo Chemical Physics Research Report CP-657R, see <http://scienide2.uwaterloo.ca/~rlroy/rkr/>. 2004.
50. Rees, A. L. G., Proc. Phys. Soc. **59**, 998 (1947).
51. Herzberg, G., *Molecular Spectra and Molecular Structure, vol. 1.*, Vol. vol.1. 1989, Malabar, Florida: Krieger publishing company.
52. Hollas, J. M., ed. *High resolution spectroscopy*. 2nd ed. 1998, John Wiley & Sons.
53. Naylor, D. A. and Tahic, M. K., Journal of the Optical Society of America a-Optics Image Science and Vision **24**, 3644 (2007).
54. West, P. W., Llacer, A. J. and Cimerman, C., Mikrochimica Acta **1165** (1962).
55. Fakioglu, E., Yurum, Y. and Veziroglu, T. N., Int. J. Hydrog. Energy **29**, 1371 (2004).
56. Martinezval, J. M., Eliezer, S., Piera, M., and Velarde, G., Phys. Lett. A **216**, 142 (1996).
57. Mulliken, R. S., Phys. Rev. **25**, 259 (1925).
58. Coxon, J. A., Foster, S. C. and Naxakis, S., J. Mol. Spectrosc. **105**, 465 (1984).
59. Melen, F., Dubois, I. and Bredohl, H., J. Phys. B-At. Mol. Opt. Phys. **18**, 2423 (1985).
60. Tanimoto, M., Saito, S. and Hirota, E., Journal of Chemical Physics **84**, 1210 (1986).
61. Stancu, G. D., Ropcke, J. and Davies, P. B., J. Mol. Spectrosc. **223**, 181 (2004).
62. Bernath, P. F., Chem. Soc. Rev. **25**, 111 (1996).
63. Kawashima, Y., Kawaguchi, K. and Hirota, E., Chemical Physics Letters **131**, 205 (1986).
64. Maki, A. G. and Wells, J. S., *Wavenumber Calibration Tables From Heterodyne Frequency Measurements* 1991, Washington: U.S. Government Printing Office.

65. Carleer, M. R., *WSpectra: A Windows (R) program to measure accurately the line intensities of high resolution Fourier transform spectra*. Remote Sensing of Clouds and the Atmosphere V, ed. Russell, J. E. S. K. L. O. Vol. 4168. 2000. 337.
66. Bernath, P. F., *Spectra of Atoms and Molecules*. 2nd ed 2005, New York: Oxford University Press. 439.
67. Kirk, R. W. and Timms, P. L., *Chemical Communications (London)* 18 (1967).
68. Pearson, E. F. and McCormic.Rv, *Journal of Chemical Physics* **58**, 1619 (1973).
69. Pearson, E. F., Norris, C. L. and Flygare, W. H., *Journal of Chemical Physics* **60**, 1761 (1974).
70. Sams, R. L. and Maki, A. G., *Journal of Molecular Structure* **26**, 107 (1975).
71. Turner, P. and Mills, I., *Molecular Physics* **46**, 161 (1982).
72. Bizzocchi, L., Esposti, C. D. and Dore, L., *Journal of Molecular Spectroscopy* **215**, 228 (2002).
73. Bizzocchi, L. and Esposti, C. D., *Journal of Molecular Spectroscopy* **241**, 67 (2007).
74. Bizzocchi, L., Degli Esposti, C. and Dore, L., *Physical Chemistry Chemical Physics* **10**, 658 (2008).
75. Fehlner, T. P. and Turner, D. W., *Journal of the American Chemical Society* **95**, 7175 (1973).
76. Kroto, H. W., Suffolk, R. J. and Westwood, N. P. C., *Chemical Physics Letters* **22**, 495 (1973).
77. Suffolk, R. J., Cooper, T. A., Pantelides, E., Watts, J. D., and Kroto, H. W., *Journal of the Chemical Society, Dalton Transactions* 2041 (1988).
78. Chau, F. T., Tang, Y. W. and Song, X., *Journal of Electron Spectroscopy and Related Phenomena* **70**, 39 (1994).
79. Ennis, L. E. and Hitchcock, A. P., *Journal of Chemical Physics* **111**, 3468 (1999).
80. Hitchcock, A. P., Ennis, L. E., Lehmann, J. F., and Denk, M. K., *Journal of Electron Spectroscopy and Related Phenomena* **114**, 1037 (2001).

81. Talaty, E. R., Huang, Y. and Zandler, M. E., *Journal of the American Chemical Society* **113**, 779 (1991).
82. Gropen, O. and Wisløff-Nilssen, E., *Journal of Molecular Structure* **32**, 21 (1976).
83. Puzzarini, C., *Physical Chemistry Chemical Physics* **6**, 344 (2004).
84. Nguyen, M. T. and Ruelle, P., *Journal of the Chemical Society, Faraday Transactions 2: Molecular and Chemical Physics* **80**, 1225 (1984).
85. Lee, E. P. F., Wang, D.-C., Chau, F.-T., Dyke, J. M., and Song, X., *Journal of Electron Spectroscopy and Related Phenomena* **97**, 49 (1998).
86. Francisco, J. S., *Journal of Chemical Physics* **124**, (2006).
87. Adler, T. B., Knizia, G. and Werner, H.-J., *The Journal of Chemical Physics* **127**, 221106 (2007).
88. Knizia, G., Adler, T. B. and Werner, H.-J., *The Journal of Chemical Physics* **130**, 054104 (2009).
89. Li, G., Hargreaves, R. J., Wang, J. G., and Bernath, P. F., *Journal of Molecular Spectroscopy* **263**, 123 (2010).
90. Maki, A. G. and Wells, J. S., *Wavenumber Calibration Tables from Heterodyne Frequency Measurements - NIST Standard Reference Database 118*, 1998, National institute of standards and technology: US.
91. Bernath, P. F., Shayesteh, A., Tereszchuk, K., and Colin, R., *Science* **297**, 1323 (2002).
92. Shayesteh, A. and Bernath, P. F., *Journal of Chemical Physics* **124**, (2006).
93. Bizzocchi, L. and Esposti, C. D., *Journal of Chemical Physics* **115**, 7041 (2001).
94. Amat, G. and Nielsen, H. H., *Journal of Molecular Spectroscopy* **2**, 163 (1958).
95. Amat, G. and Nielsen, H. H., *Journal of Molecular Spectroscopy* **2**, 152 (1958).
96. Maki, A. G. and Lide, D. R., *Journal of Chemical Physics* **47**, 3206 (1967).

97. Coxon, J. A. and Hajigeorgiou, P. G., *J. Mol. Spectrosc.* **203**, 49 (2000).
98. Pine, A. S., Fried, A. and Elkins, J. W., *J. Mol. Spectrosc.* **109**, 30 (1985).
99. Buldakov, M. A. and Cherepanov, V. N., *Journal of Physics B Atomic Molecular Physics* **37**, 3973 (2004).
100. Harrison, J. F., *J. Chem. Phys.* **128**, 4320 (2008).
101. Wang, H.-Y., Zhang, W.-A., Yuan, S.-F., Hua, W.-H., and Jiang, Z.-F., *Qiangjiguang Yu Lizishu (High Power Laser and Particle Beams)* **18**, 309 (2006).
102. Herman, R. and Wallis, R. F., *Journal of Chemical Physics* **23**, (1955).
103. De Rosa, M., Nardini, C., Piccolo, C., Corsi, C., and D'amato, F., *Appl. Phys. B: Lasers Opt.* **72**, 245 (2001).
104. Ortwein, P., Woiwode, W., Wagner, S., Gisi, M., and Ebert, V., *Appl. Phys. B: Lasers Opt.* **100**, 341 (2010).
105. Tipping, R. H. and Herman, R. M., *J. Mol. Spectrosc.* **36**, 404 (1970).
106. Zughul, M. B., *Dirasat* **XII**, 51 (1985).
107. Kiriyaama, F., *Electric dipole moment functions of the hydrogen chloride ( $^1\text{H}^{35}\text{Cl}$ ) and the carbon monoxide ( $^{12}\text{C}^{16}\text{O}$ ) molecules using an anharmonic potential*, 1999, University of North Dakota. p. 48.
108. Gelfand, J., Zughul, M., Rabitz, H., and Han, C. J., *Journal of Quantitative Spectroscopy and Radiative Transfer* **26**, 303 (1981).
109. Ogilvie, J. F. and Tipping, R. H., *Journal of Quantitative Spectroscopy and Radiative Transfer* **33**, 145 (1985).
110. Parekunnel, T., Hirao, T., Le Roy, R. J., and Bernath, P. F., *Journal of Molecular Spectroscopy* **195**, 185 (1999).
111. Stanton, A. C. and Silver, J. A., *Appl. Opt.* **27**, 5009 (1988).
112. Benedict, W. S., Herman, R., Moore, G. E., and Silverman, S., *Journal of Chemical Physics* **26**, 1671 (1957).
113. Belbruno, J. J., Zughul, M. B., Gelfand, J., and Rabitz, H., *Journal of Molecular Spectroscopy* **87**, 560 (1981).
114. Reddy, K. V., *Journal of Molecular Spectroscopy* **82**, 127 (1980).

115. Guelachvili, G., Niay, P. and Bernage, P., *J. Mol. Spectrosc.* **85**, 271 (1981).
116. Bouanich, J. P., *Journal of Quantitative Spectroscopy and Radiative Transfer* **37**, 17 (1987).
117. Bouanich, J. P., *Journal of Quantitative Spectroscopy and Radiative Transfer* **38**, 89 (1987).
118. Burrows, A., Ram, R. S., Bernath, P., Sharp, C. M., and Milsom, J. A., *Astrophysical Journal* **577**, 986 (2002).
119. Dulick, M., Bauschlicher, C. W., Burrows, A., Sharp, C. M., Ram, R. S., and Bernath, P., *Astrophysical Journal* **594**, 651 (2003).
120. Burrows, A., Dulick, M., Bauschlicher, C. W., Bernath, P. F., Ram, R. S., Sharp, C. M., and Milsom, J. A., *Astrophysical Journal* **624**, 988 (2005).
121. Weck, P. F., Schweitzer, A., Stancil, P. C., Hauschildt, P. H., and Kirby, K., *Astrophysical Journal* **584**, 459 (2003).
122. Le Roy, R. J., *LEVEL 8.0*, 2007. p. University of Waterloo Chemical Physics Research Report CP.
123. Li, G., Gordon, I. E., Bernath, P. F., and Rothman, L. S., *Journal of Quantitative Spectroscopy and Radiative Transfer* **112**, 1543 (2011).
124. Brown, J. M. and Carrington, A., eds. *Rotational Spectroscopy of Diatomic Molecules*. 2003, Cambridge University Press: Cambridge, United Kingdom.
125. Honl, H. and London, F., *Zeitschrift Fur Physik* **33**, 803 (1925).
126. Hill, E. and Van Vleck, J. H., *Physical Review* **32**, 250 (1928).
127. Mulliken, R. S., *Reviews of Modern Physics* **3**, 0089 (1931).
128. Earls, L. T., *Physical Review* **48**, 423 (1935).
129. Herzberg, G., ed. *Molecular Spectra and Molecular Structure*. Second Edition ed. 1950, Krieger Publishing Company: Malabar, Florida.
130. Tatum, J. B., *Astrophysical Journal* **S 14**, 21 (1967).
131. Bennett, R. J. M., *Monthly Notices of the Royal Astronomical Society* **147**, 35 (1970).

132. Whiting, E. E. and Nicholls, R. W., *Astrophysical Journal Supplement Series* **27**, 1 (1974).
133. Schadee, A., *Journal of Quantitative Spectroscopy & Radiative Transfer* **19**, 451 (1978).
134. Whiting, E. E., Schadee, A., Tatum, J. B., Hougen, J. T., and Nicholls, R. W., *Journal of Molecular Spectroscopy* **80**, 249 (1980).
135. Hansson, A. and Watson, J. K. G., *Journal of Molecular Spectroscopy* **233**, 169 (2005).
136. Kaiser, E. W., *The Journal of Chemical Physics* **53**, 1686 (1970).
137. Shayesteh, A., Walker, K. A., Gordon, I., Appadoo, D. R. T., and Bernath, P. F., *Journal of Molecular Structure* **695**, 23 (2004).
138. Herman, R., Rothery, R. W. and Rubin, R. J., *Journal of Molecular Spectroscopy* **2**, 369 (1958).
139. Liu, M., Pauchard, T., Sjödin, M., Launila, O., Van Der Meulen, P., and Berg, L. E., *Journal of Molecular Spectroscopy* **257**, 105 (2009).
140. Licetus, F., *'Litheosphorus Sive De Lapide Bononiensi Utini: ex typographia Nicolai Schiratti Bologna'*. Vol. The original volume can be found in the Historical Section of the University Library of Bologna, Italy. 1640, University Library of Bologna, Italy.
141. Marggraf, V. a. S., *'Chymische Schriften', Band 21767*, Berlin.
142. Holleman, A. F. W., E., *Inorganic Chemistry*. Inorganic Chemistry 2001, San Diego: Academic Press.
143. Kalpana, G., Palanivel, B. and Rajagopalan, M., *Physical Review B* **50**, 12318 (1994).
144. Zollweg, R. J., *Physical Review* **111**, 113 (1958).
145. Vij, D. R. and Singh, N., *Conference on the Physics and Technology of Semiconductor Devices and Integrated Circuits* **1523**, 608 (1992).
146. Sauval, A. J. and Tatum, J. B., *Astrophysical Journal Supplement Series* **56**, 193 (1984).
147. Barrow, R. F., Burton, W. G. and Jones, P. A., *Transactions of the Faraday Society* **67**, 902 (1971).
148. Cummins, P. G., Field, R. W. and Renhorn, I., *Journal of Molecular Spectroscopy* **90**, 327 (1981).

149. Helms, D. A., Winnewisser, M. and Winnewisser, G., *The Journal of Physical Chemistry* **84**, 1758 (1980).
150. Janczyk, A. and Ziurys, L. M., *Journal of Molecular Spectroscopy* **236**, 11 (2006).
151. Melendres, C. A., Hebert, A. J. and Street, K., *Radio Frequency Stark Spectra and Dipole Moment of BaS*. Vol. 51. 1969: AIP. 855.
152. Morbi, Z. and Bernath, P. F., *Journal of Molecular Spectroscopy* **171**, 210 (1995).
153. Tiemann, E., Ryzlewicz, C. and Tarring, T., *Zeitschrift Fur Naturforschung Section a-a Journal of Physical Sciences* **31**, 128 (1976).
154. Mathur, L. S., *Proceedings of the Royal Society of London. Series A, Mathematical and Physical Sciences* **162**, 83 (1937).
155. S.Gerstenkorn, J.Verges and J.Chevillard, *Atlas du Spectre d'Absorption de la Molecule d'Iode, Laboratoire Aime Cotton CNRS II 91405 Orsay, France* 1982.
156. Nevin, T. E., *Proceedings of the Physical Society* **43**, 554 (1931).
157. Kawashima, Y., Endo, Y., Kawaguchi, K., and Hirota, E., *Chemical Physics Letters* **135**, 441 (1987).
158. Kawashima, Y., Endo, Y. and Hirota, E., *Journal of Molecular Spectroscopy* **133**, 116 (1989).
159. M.John, Y., *Journal of Quantitative Spectroscopy and Radiative Transfer* **14**, 1317 (1974).
160. Donald W, B., *Journal of Quantitative Spectroscopy and Radiative Transfer* **24**, 269 (1980).
161. Kawashima, Y., Kawaguchi, K., Endo, Y., and Hirota, E., *Journal of Chemical Physics* **87**, 2006 (1987).
162. Gatehouse, B., Müller, H. S. P. and Gerry, M. C. L., *Journal of Molecular Spectroscopy* **190**, 157 (1998).
163. Alexandrova, A. N., Boldyrev, A. I., Zhai, H.-J., and Wang, L.-S., *Coordination Chemistry Reviews* **250**, 2811 (2006).
164. Sergeeva, A. P., Zubarev, D. Y., Zhai, H.-J., Boldyrev, A. I., and Wang, L.-S., *Journal of the American Chemical Society* **130**, 7244 (2008).

165. Cao, L. M., et al., *Advanced Materials* **13**, 1701 (2001).
166. Zhai, H. J., Wang, L. S., Alexandrova, A. N., and Boldyrev, A. I., *Journal of Chemical Physics* **117**, 7917 (2002).
167. Alexandrova, A. N., Boldyrev, A. I., Zhai, H. J., Wang, L. S., Steiner, E., and Fowler, P. W., *Journal of Physical Chemistry A* **107**, 1359 (2003).
168. Zhai, H. J., Alexandrova, A. N., Birch, K. A., Boldyrev, A. I., and Wang, L. S., *Angewandte Chemie-International Edition* **42**, 6004 (2003).
169. Zhai, H. J., Kiran, B., Li, J., and Wang, L. S., *Nature Materials* **2**, 827 (2003).
170. Zhai, H. J., Wang, L. S., Alexandrova, A. N., and Boldyrev, A. I., *Journal of Physical Chemistry A* **107**, 9319 (2003).
171. Kiran, B., Bulusu, S., Zhai, H. J., Yoo, S., Zeng, X. C., and Wang, L. S., *Proceedings of the National Academy of Sciences of the United States of America* **102**, 961 (2005).
172. Tanabashi, A., Hirao, T., Amano, T., and Bernath, P. F., *Astrophysical Journal* **624**, 1116 (2005).